NTNU – Trondheim
Norwegian University of
Science and Technology

Effect of Firing Temperature on the Kinetics of Oxygen Reduction in $La_{0.6}Sr_{0.4}Co_{0.2}Fe_{0.8}O_{3-\delta}$ (LSCF) Cathodes for Solid Oxide Fuel Cells

Brage Braathen Kjeldby

Chemical Engineering and Biotechnology
Submission date: June 2015
Supervisor: Tor Grande, IMTE
Co-supervisor: Carlos Bernuy-López, IMTE

Norwegian University of Science and Technology
Department of Materials Science and Engineering

Preface

The work presented in this master's thesis was conducted in the Inorganic Materials and Ceramics Research Group at the Department of Materials Science and Engineering, Norwegian University of Science and Technology, the spring 2015. My main supervisor was Professor Tor Grande and my co-supervisor was Dr. Carlos Bernuy-López.

The work presented was performed by the author, with the exception of the dilatometry characterization done by PhD candidate Katherine Inzani.

Furthermore, this work is a continuation of the project work titled *Optimization of the microstructure of* $La_{0.6}Sr_{0.4}Co_{0.2}Fe_{0.8}O_{3-\delta}$ *(LSCF) for solid oxide fuel cell cathodes,* carried out the fall 2014.

Brage Kjeldby
Trondheim, June 8, 2015

Acknowledgment

First and foremost, I want to thank my supervisor Tor Grande for giving me the opportunity to work on this exciting project. His advice and guidance throughout this last semester have been invaluable and of great importance to the quality of the work done. I have learned a lot about oxide ceramics, as well as how to write a scientific report.

I would also like to thank my co-supervisor Carlos Bernuy-López. He has shown unmatched willingness to assist, and it has been a privilege to work closely with him the last year. Through countless discussions and work sessions, he has helped me gain insight into the very exciting field of solid oxide fuel cells.

Furthermore, all the members of the Inorganic Materials and Ceramic Research Group should be thanked for contributing to an excellent working environment. As a master student, it has been very rewarding to get to participate in the weekly project meetings and various social events of the research group. Didrik Småbråten should be given special recognition for taking time to help me create beautiful plots, and Katherine Inzani deserves to be mentioned for doing dilatometry characterization of my materials.

Last but certainly not least, I must express my heartfelt gratitude to all the wonderful people at Chemical Engineering and Biotechnology. These past five years have been truly incredible. We have shared so many experiences and grown learning from each other. I will always

treasure the close friendships we have developed, and wish all of you the best of luck in your future endeavors.

Abstract

Solid oxide fuel cells (SOFCs) have attracted much attention as a means to reduce greenhouse gas emissions. However, the operating temperature must be reduced for the technology to become economically competitive. The main challenge associated with this is to obtain favorable kinetics for the oxygen reduction reaction at these temperatures. In the present work, symmetric cells consisting of $La_{0.6}Sr_{0.4}Co_{0.2}Fe_{0.8}O_{3-\delta}$ (LSCF) cathodes and a $Ce_{0.9}Gd_{0.1}O_{2-\delta}$ (CGO) electrolyte were fabricated and characterized. Both materials were spray-pyrolyzed by CerPoTech AS (Trondheim, Norway), and were received without any further post-treatments. A procedure for obtaining CGO pellets with relative densities in excess of 94% was developed, and airbrushing was used to deposit LSCF cathodes on the electrolyte pellets. The effect of firing temperature on the kinetics of the oxygen reduction was then evaluated by electrochemical impedance spectroscopy (EIS) of symmetric cells fired for 2 hours at 950 °C, 1000 °C, 1050 °C and 1100 °C. Measurements were recorded at three different temperatures in pure oxygen atmosphere. The area specific resistance (ASR) was observed to increase continuously with increasing firing temperature, which was explained by the simultaneous reduction in specific surface area of the LSCF cathodes. Moreover, the obtained data were correlated with the microstructure of the cathodes as documented by SEM. The deposited cathodes were observed to be uneven and inhomogeneous, which was believed to be a result of the deposition method used. Furthermore, this also explained that the obtained ASRs and calculated activation energies were higher than those reported in literature. Considering that minimal effort has been made to optimize the fabrication procedure thus far, the results documented here are nevertheless promising for the use of spray-pyrolyzed LSCF as cathode material in intermediate temperature SOFCs (IT-SOFCs).

Sammendrag

Fastoksid brenselceller kan bidra til å redusere utslipp av drivhusgasser, og har defor fått stor oppmerksomhet i nyere tid. For at teknologien skal bli økonomisk konkurransedyktig, må imidlertid driftstemperaturen senkes. Dette er utfordrende siden oksygenreduksjonen er termisk aktivert, noe som medfører at kinetikken blir tregere ettersom temperaturen reduseres. I dette arbeidet ble symmetriske celler bestående av $La_{0.6}Sr_{0.4}Co_{0.2}Fe_{0.8}O_{3-\delta}$ (LSCF) katoder og en $Ce_{0.9}Gd_{0.1}O_{2-\delta}$ (CGO) elektrolytt produsert og karakterisert. Begge råmaterialene ble spraypyrolysert av CerPoTech AS (Trondheim, Norge), og ble mottatt uten videre etterbehandlinger. En metode for fremstilling av CGO pellets med relativ tetthet større enn 94% ble utviklet, og luftkosting ble deretter brukt til deponering av katodene på elektrolytten. Effekten av brenntemperaturen på kinetikken til oksygenreduksjonen ble undersøkt med elektrokjemisk impedansspektroskopi av celler brent i 2 timer ved 950 °C, 1000 °C, 1050 °C og 1100 °C. Målinger ble gjort ved tre ulike temperaturer i ren oksygenatmosfære. Det ble observert at den arealspesifikke motstanden økte kontinuerlig med økende brenntemperatur, noe som ble forklart med den samtidige reduksjonen i spesifikt overflateareal. Videre ble disse målingene sett i sammenheng med mikrostrukturen til katoden. SEM-karakterisering viste tydelig at de deponerte katodene var ujevne og inhomogene, noe som mest sannsynlig skyldtes valget av deponeringsmetode. Dette var en viktig observasjon og forklarte hvorfor de målte arealspesifikke motstandene og beregnede aktiveringsenergiene var høyere enn verdier rapportert i litteraturen. Siden liten innsats har blitt gjort for å optimalisere produksjonsmetoden inntil videre, er resultatene likevel lovende for bruk av spraypyrolysert LSCF som katodemateriale i fastoksid brenselceller ved reduserte driftstemperaturer.

Contents

Preface i

Acknowledgment iii

Abstract v

Sammendrag vii

List of Figures xiii

1 Introduction 1

- 1.1 Background 1
- 1.2 Objective 6

2 Literature Review 7

- 2.1 Cathode design 7
- 2.2 Crystal structure of LSCF 9
  - 2.2.1 Unit cell 9
  - 2.2.2 Effect of composition 11
- 2.3 Electrical transport properties of LSCF 13
- 2.4 Oxygen reduction reaction 19
- 2.5 Electrochemical impedance spectroscopy 21
- 2.6 Ceramic processing 24
  - 2.6.1 Spray-pyrolysis 24
  - 2.6.2 Airbrushing 26

3 Experimental **29**
3.1 Materials 29
3.1.1 LSCF 29
3.1.2 CGO 30
3.2 Symmetric cells 31
3.3 Characterization 32
3.3.1 XRD 32
3.3.2 SEM 34
3.3.3 Electrochemical impedance spectroscopy 36
3.3.4 BET 37
3.3.5 Dilatometry 38

4 Results **39**
4.1 LSCF 39
4.1.1 Phase purity 39
4.1.2 Ball milling 41
4.1.3 Sintering kinetics 42
4.1.4 Specific surface area 43
4.2 CGO 43
4.2.1 Phase purity 43
4.2.2 Ball milling 44
4.2.3 Sintering kinetics 44
4.3 Symmetric cells 46
4.3.1 Chemical compatibility 46
4.3.2 Oxygen reduction kinetics 47
4.3.3 Cross section and cathode surface 51

5 Discussion **55**
5.1 Oxygen reduction kinetics 55
5.1.1 ASR and activation energy 55
5.1.2 Equivalent circuit 61

5.2 Ceramic processing 64
5.2.1 Cathode deposition 64
5.2.2 Phase purity of LSCF 66
5.2.3 CGO electrolyte pellets 67
5.3 Further work 68

6 Conclusion 71

References 73

Appendix A BET surface area plots 81

Appendix B Calculation of LSCF particle sizes 85

Appendix C Non-normalized Nyquist plots 87

List of Figures

1.1 Concentrations of greenhouse gases in the atmosphere 1

1.2 Schematic single SOFC unit 3

1.3 Cross section of an anode-supported SOFC 4

2.1 Concept of the TPB 7

2.2 Three different types of cathode design 8

2.3 Cubic unit cell of an ideal perovskite 10

2.4 Rhombohedral unit cell of $La_{0.6}Sr_{0.4}Co_{0.2}Fe_{0.8}O_{3-\delta}$ 11

2.5 Effect of Sr-content on the pseudocubic unit cell volume and Goldschmidt tolerance factor of $La_{1-x}Sr_xCo_{0.2}Fe_{0.8}O_3$ 12

2.6 Rhombohedral to orthorombic transition temperature in $La_{1-x}Sr_xCo_{0.2}Fe_{0.8}O_{3-\delta}$ and $La_{0.8}Sr_{0.2}Co_{1-y}Fe_yO_{3-\delta}$ 12

2.7 Concentration of charge carriers in $La_{0.6}Sr_{0.4}Co_{0.8}Fe_{0.2}O_{3-\delta}$ 14

2.8 Electrical conductivity of $La_{1-x}Sr_xCo_{0.2}Fe_{0.8}O_{3-\delta}$ 15

2.9 Site occupancy of $La_{1-x}Sr_xCo_{0.2}Fe_{0.8}O_{3-\delta}$ 16

2.10 Oxygen content of $La_{1-x}Sr_xCo_{0.2}Fe_{0.8}O_{3-\delta}$ 18

2.11 Oxygen deficiency, electrical conductivity and Seebeck coefficient of LSCF as function of temperature 18

2.12 Thermodynamic driving force for the oxygen reduction reaction 19

2.13 Mechanism of the oxygen reduction reaction 20

2.14 Nyquist plot and the ASR 22

2.15 Theoretical impedance response of a symmetric cell with MIEC cathodes . . . 23

2.16 Equivalent circuit for LSCF microelectrodes on YTZ electrolyte 23

2.17 Spray-pyrolysis method and apparatus 25

2.18 Spherical morphology of spray-pyrolyzed powder 26

2.19 Airbrushing apparatus 27

3.1 Calcination procedure for as-synthesized LSCF 30

3.2 Sintering procedure for CGO pellets 31

3.3 Firing procedure for the symmetric cells 32

3.4 Calcination procedure for BET measurements 38

4.1 Phase purity of as-calcined LSCF 40

4.2 Secondary phases in ball milled LSCF 40

4.3 The effect of ball milling on the particle size of LSCF 41

4.4 Volume change and sintering rate of LSCF as functions of temperature 42

4.5 Phase purity of ball milled CGO. 44

4.6 The effect of ball milling on the particle size of CGO 45

4.7 Volume change and sintering rate of CGO as functions of temperature 45

4.8 Investigation of the chemical compatibility of LSCF and CGO 46

4.9 Effect of firing time on the ASR 47

4.10 Effect of firing temperature on the ASR at 600 °C 48

4.11 Effect of firing temperature on the ASR at 700 °C 48

4.12 Effect of firing temperature on the ASR at 800 °C 49

4.13 Equivalent circuit 49

4.14 Activation energies for the oxygen reduction 50

4.15 Low magnification SEM images of symmetric cell cross sections 51

4.16 Higher magnification SEM images of symmetric cell cross sections 52

4.17 Low magnification SEM images of symmetric cell cathode surfaces 53

4.18 Higher magnification SEM images of symmetric cell cathode surfaces 54

5.1 Correspondence of the model with impedance data recorded at 600 °C. 63

5.2 Correspondence of the model with impedance data recorded at 700 °C. 63

5.3 Correspondence of the model with impedance data recorded at 800 °C. 64

A.1 BET surface area plot for sample 1 calcined at 725 °C 81
A.2 BET surface area plot for sample 2 calcined at 725 °C 82
A.3 BET surface area plot for sample 1 calcined at 900 °C 82
A.4 BET surface area plot for sample 2 calcined at 900 °C 83

C.1 Electrochemical impedance data recorded at 700 °C for two different firing times at 1100 °C. 87
C.2 Electrochemical impedance data recorded at 600 °C 88
C.3 Electrochemical impedance data recorded at 700 °C 88
C.4 Electrochemical impedance data recorded at 800 °C 89

Chapter 1

Introduction

1.1 Background

Extensive use of fossil fuels for energy generation has increased the concentrations of greenhouse gases in the atmosphere dramatically since the mid 1800s, as shown by Figure 1.1. In fact, the current concentrations of CO_2, CH_4 and N_2O are unprecedented in at least the last 800000 years [1].

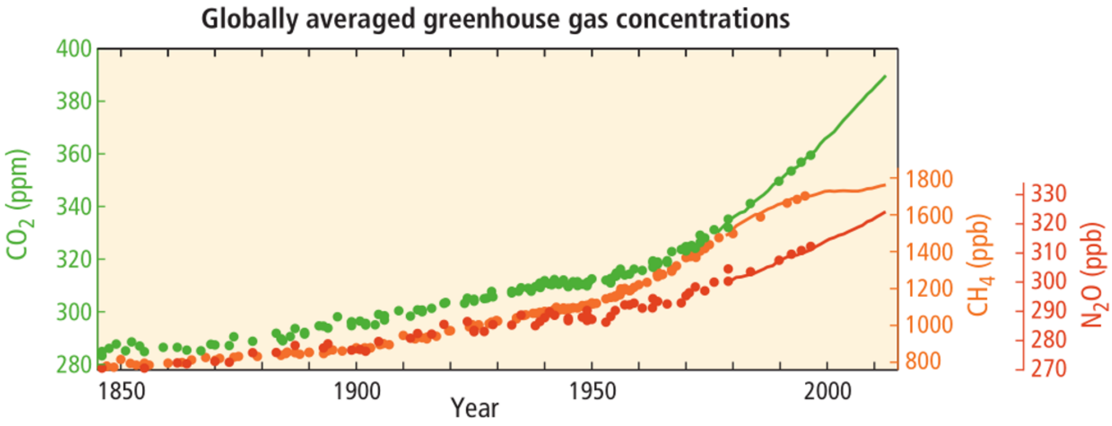

Figure 1.1: Development of greenhouse gas concentrations in the atmosphere from around 1850 until today. Adapted and reprinted from [1].

Whereas the effects of emissions of greenhouse gases were not known in earlier times, they are well-documented today. There is broad consensus in scientific communities worldwide that global warming is a direct consequence. According to The Intergovernmental Panel on Climate Change (IPCC), consequences include melting of ice sheets in Greenland and Antarctica, acidification of sea water and raised sea levels to name a few [1]. In this context, the urgency for reducing emissions and halting global warming is obvious.

The only permanent solution to this problem is to remove the need for fossil fuels as the main energy source. Numerous technologies based entirely on renewable resources are currently being investigated for this very purpose. Some of the most promising are solar, wind and geothermal energy. It is extremely important to continue the development of these technologies to make them competitive. However, fossil fuels will still play an important role in the global energy economy for many years to come. Another approach to reduce greenhouse gas emissions is thus to develop technologies that improve the conversion efficiency of fossil fuels to electricity. It is primarily in this aspect fuel cells have attracted a lot of interest in recent years. At the risk of oversimplification, a fuel cell is a device that directly converts chemical energy into easily applicable electric energy [2]. This is the fundamental concept shared by all fuel cells, even though there exist many different types. The main advantage with direct conversion is that the limitation of the Carnot cycle, inherent to for example conventional combustion engines, is avoided [3]. Solid oxide fuel cells (SOFCs) are particularly interesting in this aspect since they have the highest conversion efficiencies of all fuel cells [4]. In fact, they can reach as high as 50-60% [4] [5], and even in excess of 80% if the waste heat is recycled [3] [6].

Whereas a lot of other fuel cells rely on an aqueous electrolyte, SOFCs consist of two solid electrodes separated by a solid ionic conductor electrolyte [7]. A single SOFC unit is shown schematically in Figure 1.2. Reactants are fed continuously to the two electrodes where half-cell reactions occur, i.e. reduction at the cathode and oxidation at the anode [2]. For almost all practical applications, several SOFC units are connected in series to increase the delivered voltage [3] [8]. This is achieved by a component called the interconnect, which connects the anode of one unit to the cathode of another.

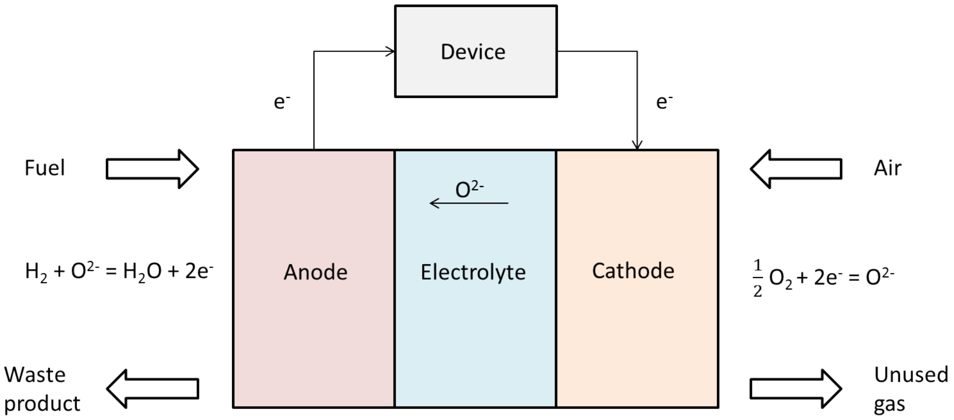
Device
e-
e-
Fuel
Air
O2-
H2 + O2- = H2O + 2e-
Anode
Electrolyte
Cathode
½ O2 + 2e- = O2-
Waste product
Unused gas

Figure 1.2: Schematic illustration of a single SOFC unit with hydrogen used as fuel.

Oxygen gas, normally fed as air, is reduced to oxide ions at the cathode according to the following reaction [9] [10]:

$$\frac{1}{2}O_2(g) + 2e^- = O^{2-} \tag{1.1}$$

The oxide ions are then transported through the dense ceramic electrolyte to the anode. At the anode, they react with the fuel to produce the waste product. This can be water and/or carbon dioxide depending on the fuel. Usually, the fuel is $H_2(g)$, $CO(g)$ or $CH_4(g)$ either separately or in combination, e.g. syngas [4] [11]. The reaction below shows the oxidation of hydrogen fuel [9] [10]:

$$H_2(g) = 2H^+ + 2e^- \tag{1.2}$$

The electrons liberated in the oxidation are directed to an external circuit, where the generated electricity can be taken advantage of. Furthermore, the overall cell reaction becomes:

$$\frac{1}{2}O_2(g) + H_2(g) = H_2O(g) \tag{1.3}$$

Designing a well-functioning SOFC system is by no means trivial. Since the list of required properties for each component is quite extensive, identifying candidate materials can be a challenge in itself. In addition, the components and their properties must also be compatible with each other. As detailed below, there are a lot of considerations to take into account. Figure 1.3 shows the cross section of a SOFC and illustrates the differences in microstructure of the various components.

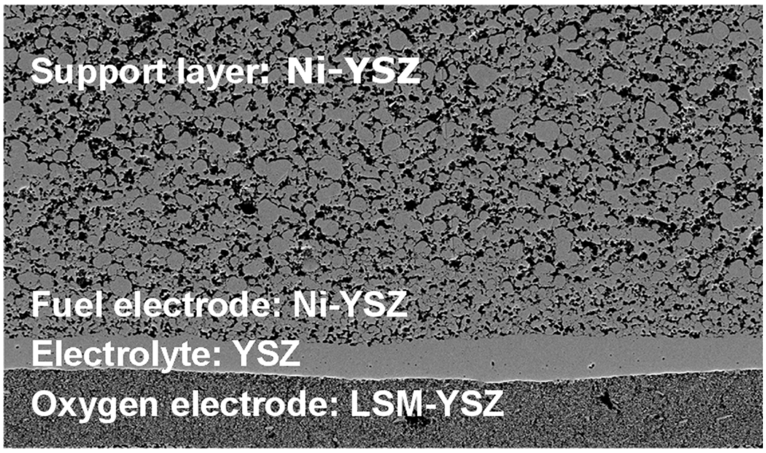

Figure 1.3: Cross section of an anode-supported SOFC. A ceramic-metal composite (cermet) of yttria-stabilized zirconia (YSZ) and nickel is used as anode, YSZ is used as electrolyte and a two-phase composite of lanthanum strontium manganese oxide (LSM) and YSZ is used as cathode. The anode layer is thick in order to provide mechanical support. Reprinted from [7].

It is crucial that the electrolyte exhibits high ionic conductivity and is as thin as possible in order to avoid excessive ohmic resistance [10]. At the same time, the electrolyte must be electronically insulating to avoid short-circuiting, and be completely dense to prevent mixing of the reactants [10]. On the other hand, one of the most important properties of the anode is to provide the mechanical stability of the cell. In addition, the anode must be stable in the reducing environment, have high electronic conductivity and have matching thermal expansion coefficient (TEC) to those of the electrolyte and interconnect [10]. Finally, high specific surface area is required to ensure sufficient transport of reactant to and waste product away from the reaction sites, respectively [10]. For similar reasons, high specific surface area is also a requirement for the cathode [6]. Furthermore, good catalytic properties for oxygen reduction is necessary. Whereas cathode materials must always be electronically conductive [10], ionic conductivity is also required for certain designs. Since the cathode is in contact with the electrolyte and interconnect, it must be chemically stable with both to avoid formation of secondary phases that can inhibit oxide ion and/or electron transport [10]. Finally, the TEC must match those of the electrolyte and interconnect. Of all the components, the requirements for the interconnect are possibly the most demanding. Since it is exposed to both reducing and oxidizing environments, it must be stable in both [10]. Moreover, the permeabilities for both oxygen gas and fuel should be low to avoid mixing of the reactants. Very high electronic conductivity and matching TEC to those of both electrodes and electrolyte is also required [10].

Despite the substantial amount of research on SOFCs in recent decades, there remain some unsolved challenges. Currently, conventional SOFCs operate at 800-1000 °C. This exceedingly high operating temperature limits the potential candidate materials drastically. The materials used are therefore rather expensive, which prevents SOFCs from becoming economically competitive [12]. Furthermore, the lifespan of a typical SOFC must be prolonged as it is currently less than satisfactory. By lowering the operating temperature, both challenges would be diminished [9] [13]. A lot of effort has therefore been invested in the development of intermediate temperature SOFCs (IT-SOFCs), with operating temperatures below 700 °C [5] [6]. This would allow for the use of metallic interconnects, which are significantly cheaper [9] [14] [15] than the commonly used ceramic alkaline-earth doped $LaCrO_3$ [10] [16]. Furthermore, problems related to interdiffusion, formation of secondary phases and thermal cycling will diminish if the temperature is lowered [5] [9]. Thus, the lifespan is expected to increase.

Unfortunately, new challenges are introduced simultaneously. The development of improved fabrication methods has enabled production of thinner and less resistive electrolytes [17]. In addition, novel electrolyte materials that perform well at lower temperatures, such as $Ce_{0.9}Gd_{0.1}O_{2-\delta}$ (CGO), have been discovered [4] [6]. Thus, the main limiting factor is no longer associated with the ohmic resistance of the electrolyte, and the focus has shifted towards the electrodes and the electrochemical processes occurring there [17]. The electrode reactions are thermally activated, and their rates can be expressed by Arrhenius type equations. Hence, the activation energy increases and the kinetics become slower as the temperature is lowered [5] [14] [17]. As the oxygen reduction is usually the main limiting factor [12], the majority of recent research has focused on the cathode [17] [18]. However, the complexity of the reaction has made it difficult to gain insight, and the mechanistic understanding is still less than satisfactory [12].

1.2 Objective

The traditional SOFC cathode, as exemplified by $La_{1-x}Sr_xMnO_{3-\delta}$ (LSM) [16] [17], exhibits high electronic conductivity and negligible ionic conductivity. For this type of cathode, the reduction is believed to be restricted to the triple phase boundaries (TPBs) [5], i.e. the locations where the oxygen gas, the electrode and the electrolyte intersect. Previous research has documented that the overall performance of cells with this type of cathodes scales with the length of the TPB [17]. Much effort has therefore been put into developing mixed ionic-electronic conductor (MIEC) cathodes [5]. It is believed that this will lower the area specific resistance (ASR) and result in improved kinetics at lower temperatures [17].

In this work, symmetric cells with $La_{0.6}Sr_{0.4}Co_{0.2}Fe_{0.8}O_{3-\delta}$ (LSCF) cathodes and $Ce_{0.9}Gd_{0.1}O_{2-\delta}$ (CGO) electrolyte were fabricated and characterized. The LSCF and CGO powders were spray-pyrolyzed by CerPoTech AS (Trondheim, Norway), and were received without further post-treatments. A procedure for fabrication of CGO pellets with relative densities in excess of 94% was developed. Afterwards, LSCF cathodes were deposited on the electrolyte pellets by airbrushing. Numerous sets of symmetric cells were fabricated, and each set was subjected to an unique firing temperature. The effect of this temperature on the kinetics of the oxygen reduction was then evaluated by electrochemical impedance spectroscopy (EIS) in pure oxygen at three different measurement temperatures. Moreover, these results were related to the microstructure of the cathodes as determined by SEM.

Chapter 2

Literature Review

2.1 Cathode design

The purpose of any SOFC cathode is to reduce molecular oxygen to oxide ions according to Equation 1.1. This requires that electrons are supplied to the reaction sites and that the generated oxide ions are transported away. Electronic and ionic conductivity are thus features that invariably must be taken into account for any cathode design. As such, the TPB is an important concept. The TPB is, as briefly described in Chapter 1, the locations where the electrode, electrolyte and oxygen gas intersect. Figure 2.1 illustrates this concept in a simplified manner.

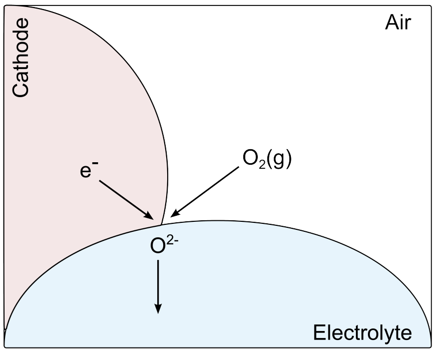

Figure 2.1: The concept of the triple phase boundary (TPB). Reduction of the oxygen gas occurs in the locations where the cathode, electrolyte and air intersect.

Several different cathode designs have been investigated and documented in the SOFC literature, and they can be divided into three fundamentally different types [4] [17]: (i) porous single-phase electronic conductor, e.g. LSM, (ii) porous two-phase composite of electronically and ionically conducting materials, e.g. LSM and YSZ and (iii) porous single-phase MIEC, e.g. LSCF. Figure 2.2 illustrates these different approaches schematically.

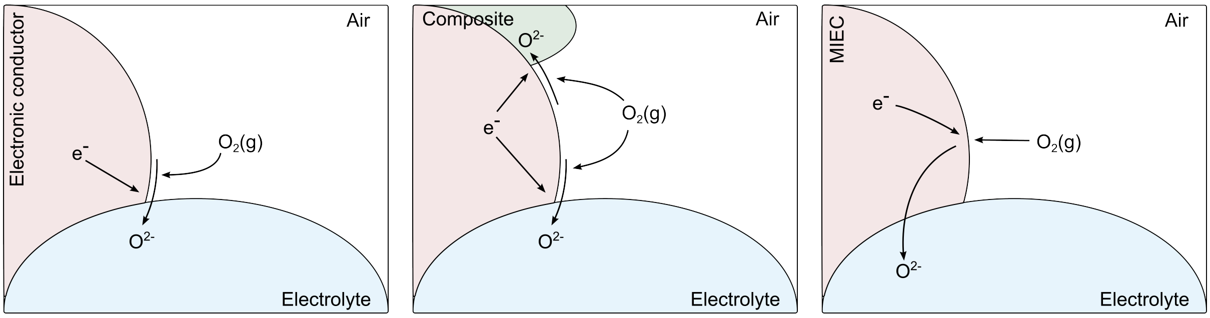

(a) Type (i) **(b)** Type (ii) **(c)** Type (iii)

Figure 2.2: The three different types of cathode design: (i) single-phase electronic conductor, (ii) two-phase composite of an electronic and ionic conductor and (iii) single-phase MIEC.

Type (i) represents the traditional SOFC cathode. This is reflected in the fact that LSM has been one of the most studied cathode materials since the early 1970s [7] [16] [17]. For this kind of cathode, the reduction of oxygen is confined to the TPBs. Since the cathode has negligible ionic conductivity, the reduction reaction must occur in close proximity to the TPBs to allow for transport of oxide ions away from the reaction site through the electrolyte to the anode where they oxidize the fuel and make the waste product. Simultaneously, the electronic conductivity of the cathode ensures that the electrons travelling through the external circuit are directed to the reaction sites where oxygen is reduced. However, this design is not ideal as previous research documents that the overall cathode performance is proportional to the one dimensional length of the TPB [17] [19]. The implication of this is that the performance can be improved by increasing the contact area between the electronically and ionically conducting materials. One possible improvement is therefore to fabricate a composite as detailed by type (ii). Another solution is as described by type (iii) to use a single-phase MIEC. This approach has several advantages. The TPB area becomes equivalent to the entire gas-exposed surface area, since the oxygen reduction in theory can occur over the entire surface [7]. Another advantage as compared to the two-phase composite, is ease of fabrication.

2.2 Crystal structure of LSCF

2.2.1 Unit cell

The cathodes used in SOFCs are very commonly perovskite metal oxides with the general chemical formula $ABO_{3-\delta}$ [7], where A and B are cations and O is oxygen anions. An ideal perovskite has a cubic unit cell described by the $Pm\overline{3}m$ space group [20], as illustrated by Figure 2.3. The Goldschmidt tolerance factor, defined in the following equation, is used to assess whether the perovskite is ideal or not [20]:

$$\tau = \frac{r_{\mathrm{A}} + r_{\mathrm{O}}}{\sqrt{2}(r_{\mathrm{B}} + r_{\mathrm{O}})} \tag{2.1}$$

where r_{A}, r_{B} and r_{O} are the ionic radii of the A-, B- and O-ions, respectively [6]. Although an ideal perovskite corresponds to $\tau = 1$, deviation from this is very common. The ability to accommodate various different cations, in addition to both cation and anion vacancies, is known to provide perovskites with numerous interesting functional properties. Among these are electronic and ionic conductivity, which make them well-suited for SOFC cathode purposes.

When the perovskite is not ideal, the A-O bonds experience tension and the B-O bonds experience compression, or vice versa depending on whether $\tau < 1$ or $\tau > 1$. This entails increased energy as compared to the ideal case, and several mechanisms for minimization of this are known [6]. The most common one is tilting of the corner-shared BO_6 octahe-

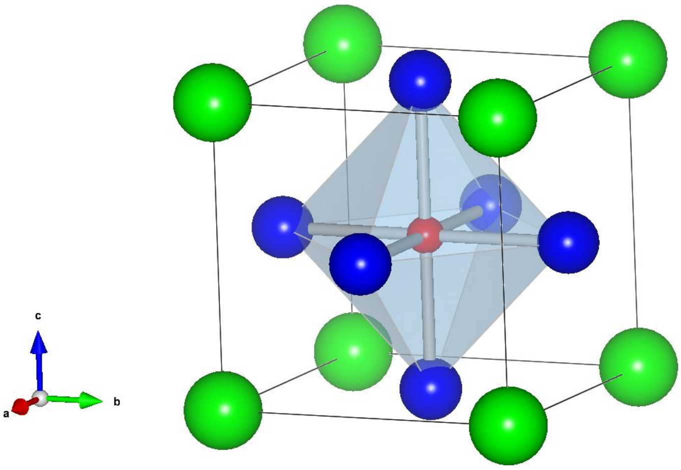

Figure 2.3: The cubic unit cell, space group $Pm\overline{3}m$, of an ideal perovskite. A-site cations are located in the corners, B-site cations in the unit cell center and O-anions at the unit cell faces. The figure was generated by the VESTA software [21].

dra relative to one another [6]. Such tilting decreases the number of symmetry elements of the perovskite, meaning that the unit cell has to be contracted to correctly account for the symmetry elements of the lattice [6]. An important consequence of this is that new crystal planes will be able to give constructive interference, which gives rise to reflections in the diffractogram known as superreflections [6]. Such reflections can be seen in diffractograms of LSCF, as it is not an ideal perovskite. The unit cell is shown in Figure 2.4, with the corresponding atom positions taken from PDF 04-017-2448 given in Table 2.1. As can be seen, the unit cell is rhombohedral and can be described by the $R\overline{3}c$ space group [22] [23].

Table 2.1: Atom positions in the rhombohedral unit cell of LSCF, space group $R\overline{3}c$, given in Cartesian coordinates. The values are taken from PDF 04-017-2448.

Atom	x	y	z
La	0	0	0.25
Sr	0	0	0.25
Fe	0	0	0
Co	0	0	0
O	0.458	0	0.25

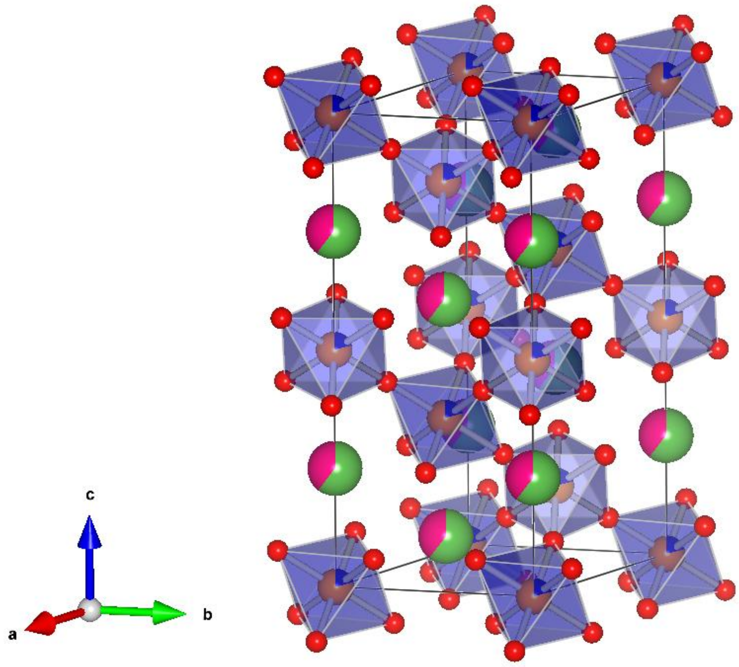

Figure 2.4: The rhombohedral unit cell, space group $R\bar{3}c$, of $La_{0.6}Sr_{0.4}Co_{0.2}Fe_{0.8}O_{3-\delta}$ (LSCF). The green, pink, orange, blue and red atoms represent La, Sr, Fe, Co and O, respectively. The figure was generated by the VESTA software [21].

2.2.2 Effect of composition

Furthermore, the unit cell is observed to change if the composition is varied. Aliovalent substitution of La^{3+} with Sr^{2+} leads to an increase in the average radius of the A-cations [23]. Furthermore, some of the Co^{3+} and/or Fe^{3+} cations will be oxidized to the tetravalent state to compensate for the charge imbalance [23], explained in detail in Chapter 2.3. Consequently, the average radius of the B-cations decrease. Due to the higher charge, the B-O bonds in the BO_6 octahedra will then become stronger. The result of these effects combined is that the unit cell size decreases as the Sr-content increases [22] [23], which can be seen from Figure 2.5. From the indicated change in space group, it is also obvious that structural transitions are occurring. Indeed, it has previously been reported that $La_{1-x}Sr_xCo_{0.2}Fe_{0.8}O_{3-\delta}$ has a rhombohedral unit cell at room temperature for $x \geq 0.3$ and an orthorhombic unit cell for $x \leq 0.2$. Similarly, $La_{0.8}Sr_{0.2}Co_{1-y}Fe_yO_{3-\delta}$ has been reported to be rhombohedral for $y \leq 0.7$ and orthorombic for $y \geq 0.8$ [24]. This is shown in Figure 2.6a and 2.6b, respectively.

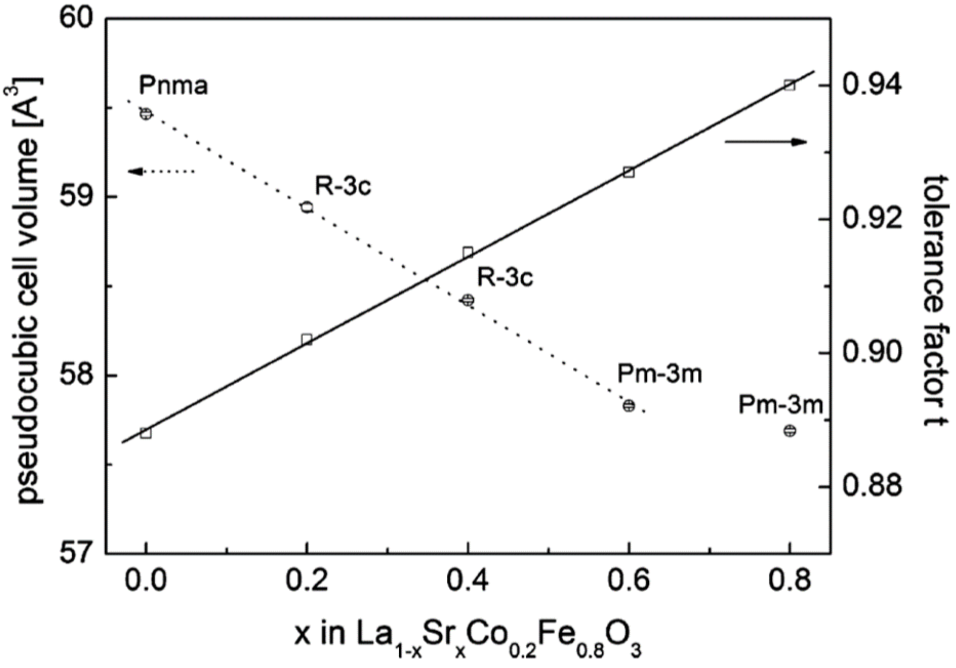

Figure 2.5: The pseudocubic unit cell volume and Goldschmidt tolerance factor plotted as functions of the Sr-content in $La_{1-x}Sr_xCo_{0.2}Fe_{0.8}O_3$. Reprinted from [22].

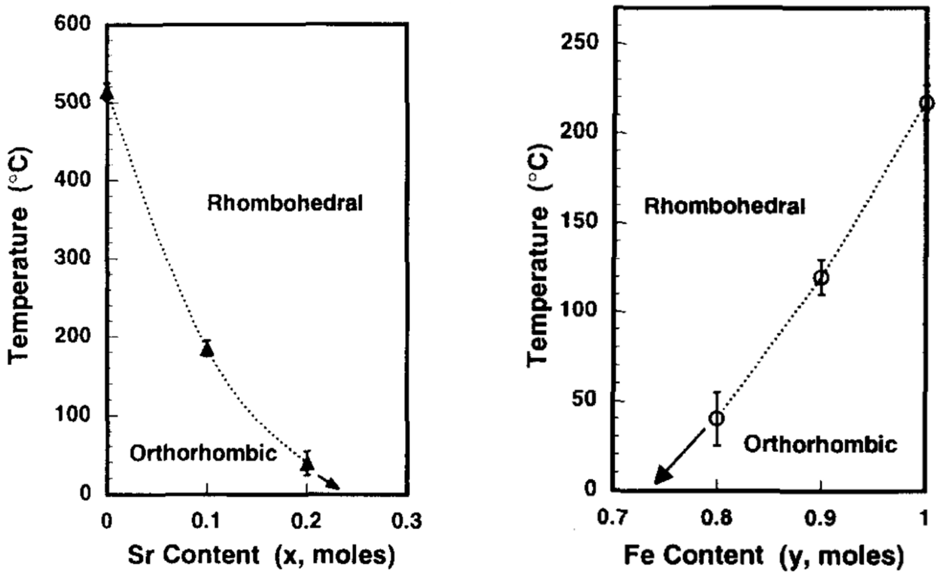

(a) $La_{1-x}Sr_xCo_{0.2}Fe_{0.8}O_{3-\delta}$ **(b)** $La_{0.8}Sr_{0.2}Co_{1-y}Fe_yO_{3-\delta}$

Figure 2.6: The rhombohedral to orthorombic transition temperature in $La_{1-x}Sr_xCo_{0.2}Fe_{0.8}O_{3-\delta}$ and $La_{0.8}Sr_{0.2}Co_{1-y}Fe_yO_{3-\delta}$ shown as a function of Sr- and Fe-content, respectively. Reprinted from [23] and [24], respectively.

2.3 Electrical transport properties of LSCF

The kinetics of the oxygen reduction, and thereby the efficiency of the SOFC, are improved by high electrical conductivity [6]. Thus, the two most important properties of a MIEC cathode is the electronic and ionic conductivity. By ensuring high electronic conductivity, the polarization resistance associated with charge transfer processes can be minimized [6]. A value of 100 S/cm is normally taken as the lower limit for a material to be suitable [6] [25]. Similarly, good ionic conductivity reduces the polarization resistance by allowing the oxygen reduction to take place over a larger portion of the electrode surface [6]. The electronic and ionic conductivity of LSCF at 900 °C have been reported as 230 S/cm and 0.2 S/cm, respectively [26]. It is worth noting that this ionic conductivity is many orders of magnitude larger than the value of 10^{-7} S/cm reported for LSM at 900 °C [26].

Charge compensation due to aliovalent substitution of La^{3+} by Sr^{2+} is very important for the conductivity behavior of LSCF. Two mechanisms of charge compensation are shown by Kröger-Vink notation in the following reactions [6]:

$$\mathrm{SrMO_3} \xrightarrow{\mathrm{LaMO_3}} \mathrm{Sr_{La}}' + \mathrm{M_M}^{\bullet} + 3\,\mathrm{O_O}^{x} \tag{2.2}$$

$$2\,\mathrm{M_M}^{\bullet} + \mathrm{O_O}^{x} \longrightarrow 2\,\mathrm{M_M}^{x} + \mathrm{V_O}^{\bullet\bullet} + \frac{1}{2}\mathrm{O_2(g)} \tag{2.3}$$

Thus, the prevailing electroneutrality condition becomes:

$$[\mathrm{Sr_{La}}'] = [\mathrm{M_M}^{\bullet}] + 2\,[\mathrm{V_O}^{\bullet\bullet}] \tag{2.4}$$

The mechanism shown in Equation 2.2 relies on the oxidation of one B-site cation to a higher valency, e.g. oxidation of Fe^{3+} to Fe^{4+}. Conversely, the mechanism shown in Equation 2.3

relies on the introduction of oxygen vacancies. As illustrated by these equations, there are three possible charge carriers in LSCF: (i) electrons, (ii) holes and (iii) oxygen vacancies. Factors such as the temperature, partial pressure of oxygen and the given B-site transition metal cations will influence to what extent Equation 2.2 and 2.3 happen relative to each other [6] [7]. Wang et al. investigated the concentration of the various charge carriers in $La_{0.6}Sr_{0.4}Co_{0.8}Fe_{0.2}O_{3-\delta}$ as a function of oxygen partial pressure, as shown in Figure 2.7 [27]. Holes are expected to be the main charge carrier as the concentration, denoted by p, is much larger than the concentration of electrons, denoted by n, over the entire oxygen partial pressure range investigated. At low oxygen partial pressures, however, oxygen vacancies will be important.

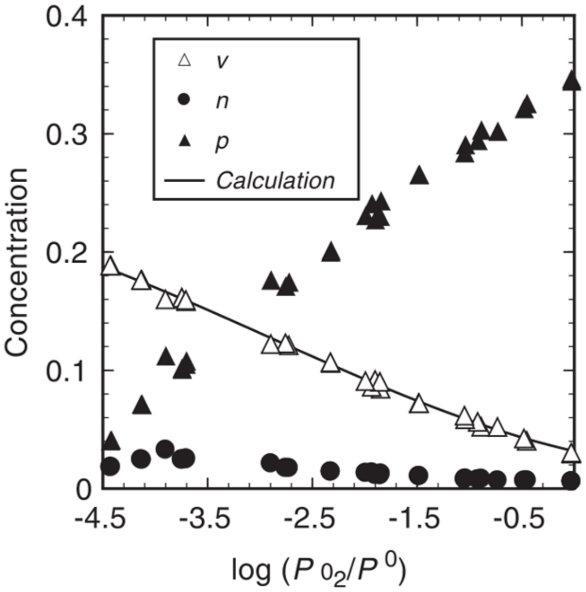

Figure 2.7: Concentration of the various charge carriers in $La_{0.6}Sr_{0.4}Co_{0.8}Fe_{0.2}O_{3-\delta}$ plotted as a function of oxygen partial pressure, P_{O_2}, at 1073 K. The concentrations of holes, electrons and oxygen vacancies are denoted by p, n and v, respectively. P^0 = 101325 Pa. Reprinted from [27].

The electrical conductivity of $La_{1-x}Sr_xCo_{0.2}Fe_{0.8}O_{3-\delta}$ has been investigated thouroughly by Tai et al. [23]. They found that the conductivity depends both on the temperature and Sr-content, as evidenced by Figure 2.8. Each composition with $x \geq 0.1$ displays an increase in conductivity until a certain characteristic temperature is reached. The conductivity behavior below this temperature was attributed to the adiabatic small polaron hopping mechanism:

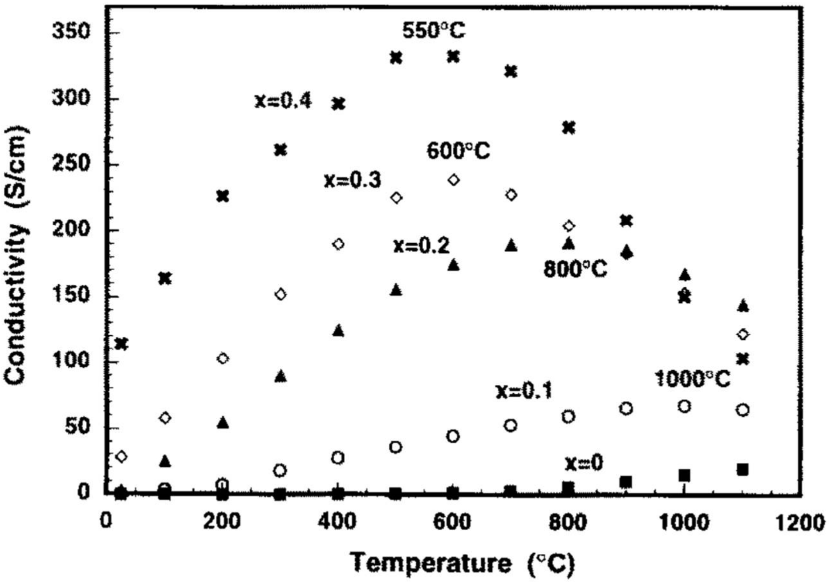

Figure 2.8: Electrical conductivity in air of $La_{1-x}Sr_xCo_{0.2}Fe_{0.8}O_{3-\delta}$ plotted as a function of temperature and Sr-content. Reprinted from [23].

$$\sigma = \frac{A}{k_b T}\exp\left(\frac{-E_a}{k_b T}\right) \tag{2.5}$$

where A is a material constant including the concentration of charge carriers, E_a is the activation energy for polaron hopping, k_b is Boltzmann's constant and T is the absolute temperature. Available sites for polaron hopping are created when charge compensation occurs by mixed valence state of the B-site cations [6], described by Equation 2.2. Thus, the associated activation energy is lowered and the electrical conductivity increased due to enhanced mobility of the charge carriers. From this consideration alone, it is expected that the electrical conductivity will be maximized for a doping level of Sr^{2+} equal to 0.5 [6]. Furthermore, since the pre-exponential term decreases with temperature and the exponential term increases, a maximum conductivity for a certain temperature is expected based on the polaron mechanism. However, this maximum would correspond to $T = E_a/k_b$ [23]. Since these temperatures are significantly higher than those observed, it is reasonable to assume that other mechanisms start to dominate the conductivity behavior as the temperature increases. Valuable information about these can be extracted from evaluation of the charge carrier concentration for polaron hopping. This can be expressed in terms of the site occupancy, i.e. the fraction of available hopping sites occupied by charge carriers, by the following equation [23]:

$$C = \left(1 + \exp\left(\frac{Qe}{k_{\mathrm{b}}}\right)\right)^{-1} \tag{2.6}$$

where C is the site occupancy, Q is the Seebeck coefficient and e is the elementary charge. The site occupancy was documented to be dependent both on temperature and Sr-content, as shown in Figure 2.9 [23].

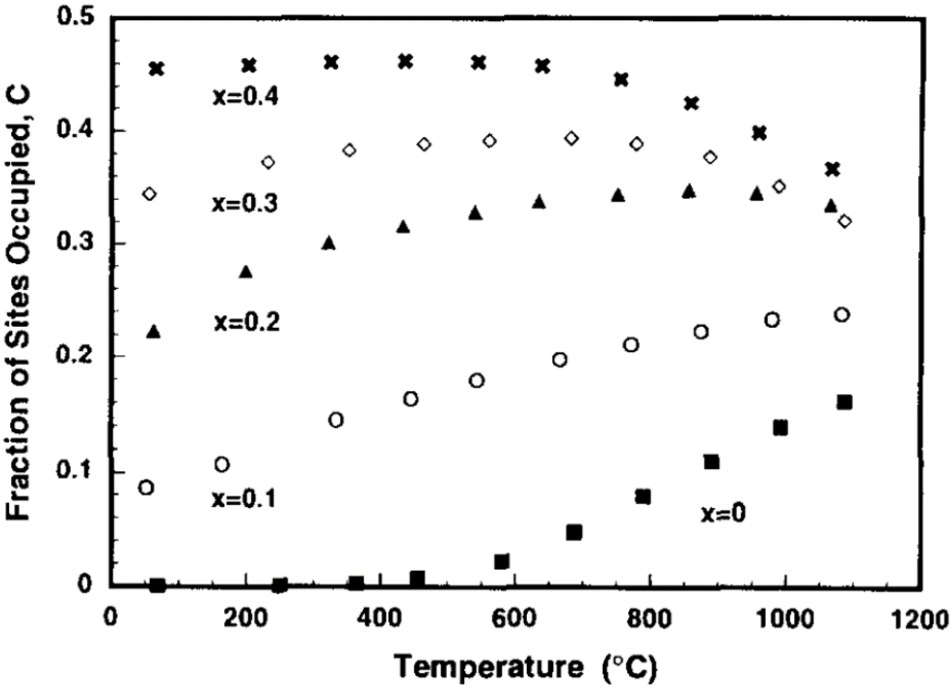

Figure 2.9: Site occupancy calculated from Seebeck data of $La_{1-x}Sr_xCo_{0.2}Fe_{0.8}O_{3-\delta}$ plotted as a function of temperature and Sr-content. Reprinted from [23].

Two opposing effects can be used to account for the observed behavior. Firstly, the increase in site occupancy with increasing temperature can be explained by the charge disproportionation of two Co^{3+}, or equivalently Fe^{3+}, according to the following reaction [23]:

$$2\text{Co}^{3+} = \text{Co}^{2+} + \text{Co}^{4+} \tag{2.7}$$

The reaction is thermally-activated, which is in accordance with the fact that the charge carrier concentration is observed to increase with increasing temperatures.

Conversely, the decrease in site occupancy in the high temperature region for compositions with $x \geq 0.1$, can be explained by introduction of oxygen vacancies. Figure 2.10 shows that the oxygen deficiency for For $La_{1-x}Sr_xCo_{0.2}Fe_{0.8}O_{3-\delta}$ was observed to increase with temperature. It is also noteworthy that compositions with $x \geq 0.3$ were oxygen deficient even at low temperatures. Oxygen vacancies are very important for the ionic conductivity, since oxide ions usually are much larger than interstitial positions in the perovskite structures [6]. The ionic conductivity is thus enhanced up to a certain vacancy concentration. However, continued formation of vacancies after this can give defect association and/or structural deformations [6]. Moreover, the introduction of oxygen vacancies in the high temperature region can explain the observed decline in electrical conductivity seen in Figure 2.8. Figure 2.11 clearly shows that a substantial decrease in the electrical conductivity is observed simultaneously with introduction of oxygen vacancies. This can be justified by evaluating the electroneutrality condition given in Equation 2.4. For each oxygen vacancy formed, two $\text{M}_\text{M}^\bullet$ must be eliminated. Consequently, the available sites for polaron hopping are reduced and the electrical conductivity is decreased. This might seem counterintuitive, as one might expect that the increased ionic conductivity would help maintain an overall large electrical conductivity. However, it is the electronic contribution that governs this [22], which can be explained by the much larger mobility of the electronic charge carriers [28]. The introduction of oxygen vacancies is also believed to reduce the mobility of the electronic charge carriers by serving as scattering centers [23], since the electrical conductivity was observed to decrease much more rapidly than the carrier concentration at high temperatures [23]. This implied that the reduced number of charge carriers could not account for the observed conductivity behavior alone.

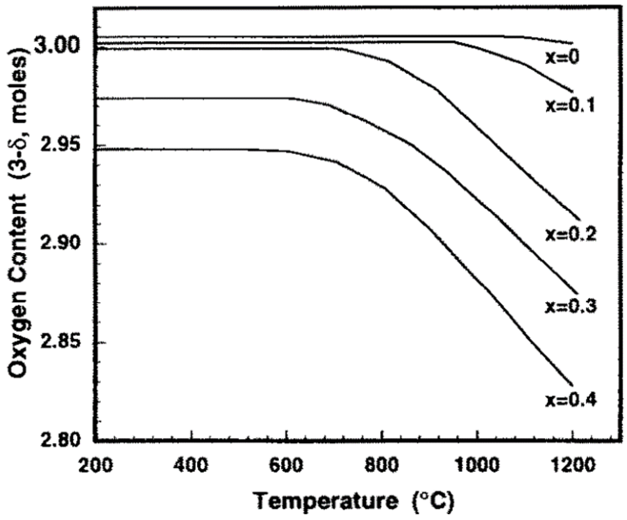

Figure 2.10: Oxygen content of $La_{1-x}Sr_xCo_{0.2}Fe_{0.8}O_{3-\delta}$ in air plotted as a function of temperature and Sr-content. Reprinted from [23].

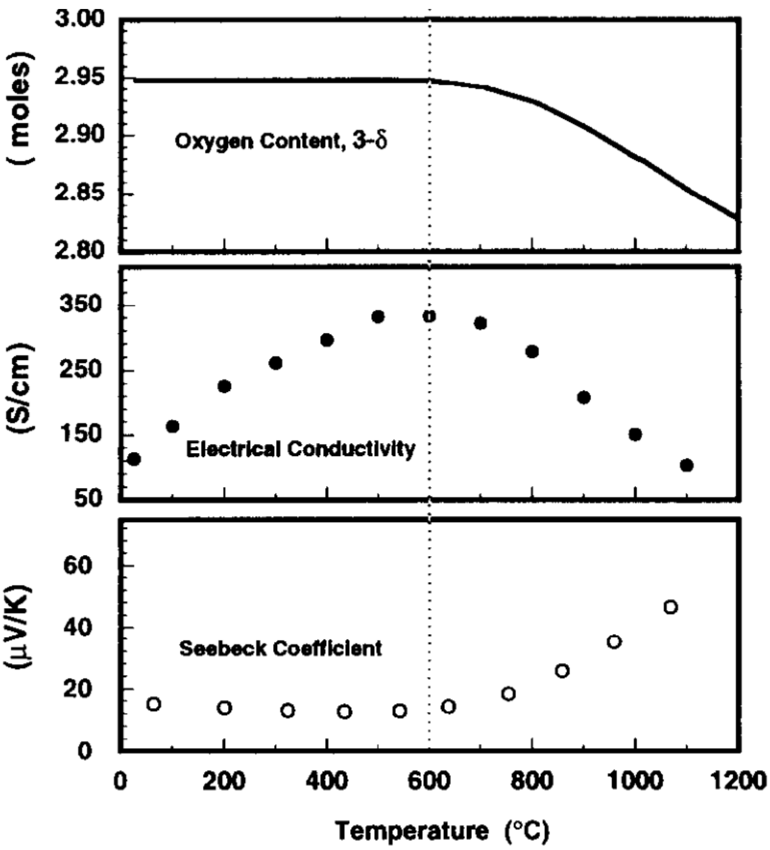

Figure 2.11: Oxygen deficiency, electrical conductivity and Seebeck coefficient of $La_{0.6}Sr_{0.4}Co_{0.2}Fe_{0.8}O_{3-\delta}$ in air plotted as a function of temperature. Adapted and reprinted from [23].

2.4 Oxygen reduction reaction

The thermodynamic driving force for the oxygen reduction reaction in an actual fuel cell arises from the difference in oxygen partial pressure on the cathode and anode side of the electrolyte [6]. Since air is being fed to the cathode, the oxygen partial pressure will be highest on this side of the electrolyte. Consequently, the chemical potential of oxygen will also be higher on the cathode side. Oxygen reduction and transport through the electrolyte will thus result in reduced oxygen chemical potential, which implies a negative change in Gibbs energy. Figure 2.12 shows this conceptually.

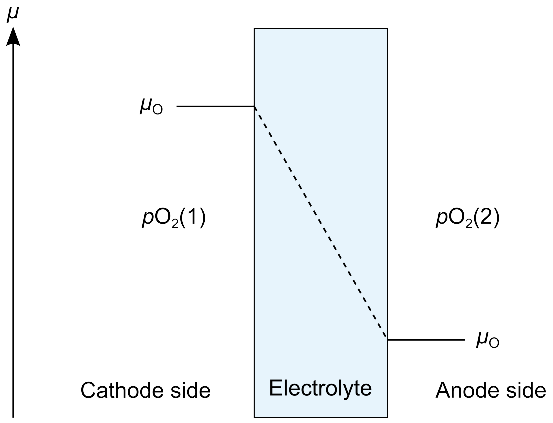

Figure 2.12: The thermodynamic driving force for the oxygen reduction reaction arises from the difference in oxygen partial pressure, pO_2. Since $pO_2(1) \gg pO_2(2)$, the chemical potential of oxygen, μ_O, will be larger on the cathode side of the electrolyte. The chemical potential gradient is not necessarily linear as depicted here. Adapted from [6].

Although the oxygen reduction reaction has been studied extensively, the mechanism and kinetics are still not entirely understood. The oxygen reduction happens in multiple steps that depend on the type of cathode used [14] [17]. Firstly, molecules of oxygen gas have to adsorb on one or more of the solid surfaces present, i.e. the cathode and electrolyte, to become partly reduced ionic/atomic species. Before, during or after partial reduction, the oxygen species must be transported to the electrolyte either along an interface, across a surface or through the bulk of the cathode material [6] [17]. At this point, the partially reduced species must have become fully reduced in order to be transported through the electrolyte as oxide ions. Some of the various possible reaction steps are shown conceptually in Figure

2.13. However, there is still ongoing debate regarding the mechanism of the reduction and which step(s) that is rate-determining [6].

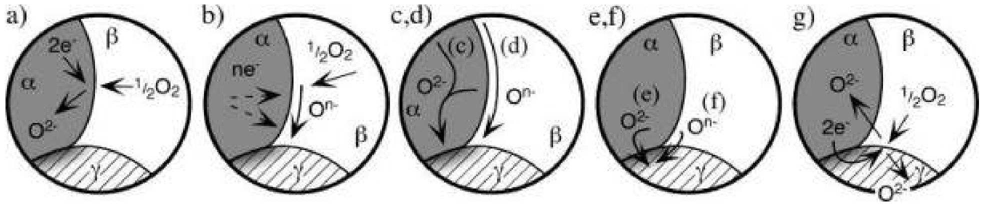

Figure 2.13: Some of the possible reaction steps for the oxygen reduction reaction. The α, β and γ phases represent the cathode, oxygen gas and electrolyte, respectively. Reprinted from [17].

To better understand the kinetics of the oxygen reduction, it is worthwhile to refer to the somewhat simpler system of a Pt-cathode on a YSZ-electrode. This is one of the most extensively studied electrode-electrolyte systems to date, and much of the knowledge gained from this can be applied to the more complex perovskite cathodes found in SOFCs. For a long time there were two opposing mindsets on how to evaluate the kinetics of the reduction reaction on the Pt-cathode. Some believed that the system could be described in terms of traditional electrochemical kinetics, i.e. Tafel kinetics. Conversely, others relied on electrochemical impedance spectroscopy (EIS). The main discrepancy between the two was that the reduction should be rate-limited by charge transfer processes on the electrode surface according to Tafel kinetics, whereas EIS showed that the reduction was rate-limited by diffusion of gas species and resulting concentration gradients [6]. Several works have documented by use of EIS that viewing the system exclusively as charge transfer limited is not justified [29] [30] [31]. However, it was later shown that the kinetics could be governed both by charge transfer and diffusion, as adsorption of oxygen gas and diffusion of oxygen to the TPBs in some instances could be interconnected [32]. When expanding the discussion to include the state-of-the-art MIEC perovskite cathodes, the picture becomes even more complicated. Owing to their ionic conductivity, the MIECs will allow for transport of oxygen through the bulk as well [33].

2.5 Electrochemical impedance spectroscopy

Electrochemical impedance spectroscopy is as mentioned above a method used to evaluate the kinetics of reactions occurring in gas diffusion electrodes, and it was first reported by Bauerle [34]. An important feature of the technique is that it relies on AC currents. The most common way of doing impedance measurements is to apply a periodic voltage with constant amplitude over a predefined frequency interval to the system being investigated [6] [35]. The phase shift and amplitude of the resulting current response are then measured as functions of frequency [35]. If the various electrode processes occur at different frequencies, it will be possible to determine the individual reaction steps constituting the overall electrode reaction.

The impedance function is complex and frequency-dependent [35], and can be written as [12]:

$$Z(\omega) = Z_{\text{real}}(\omega) + i Z_{\text{imag}}(\omega) \tag{2.8}$$

where i is the imaginary unit and ω is the angular frequency. Real, ohmic resistances are represented by $Z_{\text{real}}(\omega)$, whereas $Z_{\text{imag}}(\omega)$ represents reactances [6]. The latter provides information about the polarization resistances of the processes constituting the electrode reaction [6]. Furthermore, impedance data are commonly represented in Nyquist plots [36], in which the imaginary part of the impedance function is plotted as a function of the real part [6]. Such plots consist of semi-circles or arcs that represent rate-limiting electrode processes [6]. Importantly, Nyquist plots allow for visual assessment of the ASR, which is a very important parameter for evaluation of the kinetics of the electrode reaction. The ASR can be viewed as the total polarization resistance, meaning that low ASR entails fast kinetics. Figure 2.14 shows a Nyquist plot in which the raw data with unit Ω has been multiplied with the geometrical cathode area to give data with unit Ωcm^2. The ASR for the electrode process corresponding to the observed semi-circle can be found as the distance between the high-

and low-frequency intercept of the semi-circle with the x-axis. If the impedance response consists of several semi-circles, the overall ASR will equal the sum of these. When working with symmetric cells, i.e. there are two similar electrodes, the ASR for one electrode is found by dividing the graphically obtained value by two [5] [25].

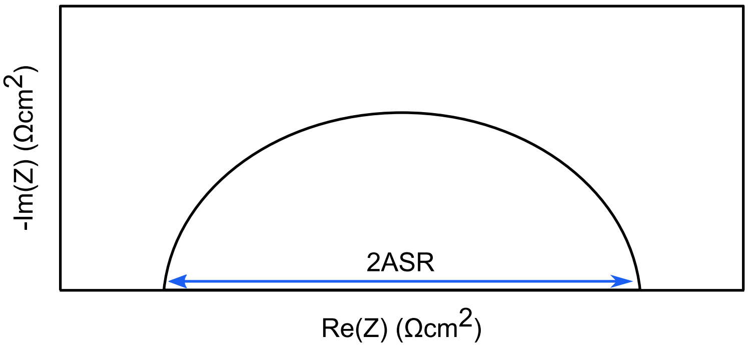

Figure 2.14: Schematic illustration of the relation between the semi-circles in the Nyquist plot and the ASR for the electrode reaction. In a symmetric cell, this value must be divided by two to give the ASR for one cathode only.

After impedance measurements have been completed, it is common practice to model the experimental data with an equivalent electrical circuit consisting of standard elements such as resistors and capacitors [12]. However, great care should be exercised while doing this. It is important to verify that the circuit not only fits the data reasonably well, but that the various circuit elements can be attributed to actual physical processes taking place during the reaction. Furthermore, the common practice of proposing these circuits based on the experimental data can be problematic, as good fits are normally taken to be sufficient evidence for the correctness of the model [12]. However, this can lead to misinterpretation of the system as several different circuits can yield the same frequency dependence of the impedance function, even though the value of each individual circuit element will vary. Thus, the physical interpretation of the system will depend upon which circuit is chosen. To avoid this problem, one could instead derive the circuit from fundamental concepts beforehand [12].

It has previously been observed that the impedance response of symmetric cells with MIEC cathodes can consist of three distinct features: (i) ohmic resistance of the electrolyte, (ii) charge transfer resistances at interfaces, including electronic transfer at the interconnect/-electrode interface and ionic transfer at the electrode/electrolyte interface and (iii) chemical impedance of non-charge-transfer process, including oxygen surface exchange, solid-state and gas-phase diffusion [37] [38]. Figure 2.15 illustrates this in a schematic Nyquist plot. Baumann et al. were able to identify the electrode processes corresponding to the three individual semi-circles by investigating dense thin film LSCF microelectrodes with well-defined geometry on YTZ electrolyte substrates [12]. Furthermore, they used the circuit given in Figure 2.16 to model the experimental data. They found that the high frequency (HF), medium frequency (MF) and low-frequency (LF) semi-circles corresponded to electron transfer, ionic transfer and chemical diffusion resistance, respectively [12].

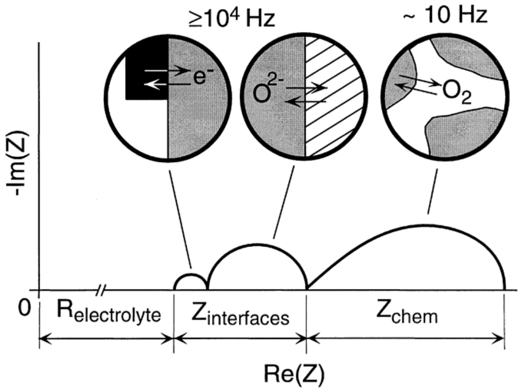

Figure 2.15: Theoretical impedance response of a symmetric cell with MIEC cathodes. $R_{\text{electrolyte}}$ is the electrolyte resistance, $Z_{\text{interfaces}}$ is the impedance related to interfacial charge-transfer processes and Z_{chem} is the impedance related to non-charge-transfer processes. Adapted and reprinted from [39].

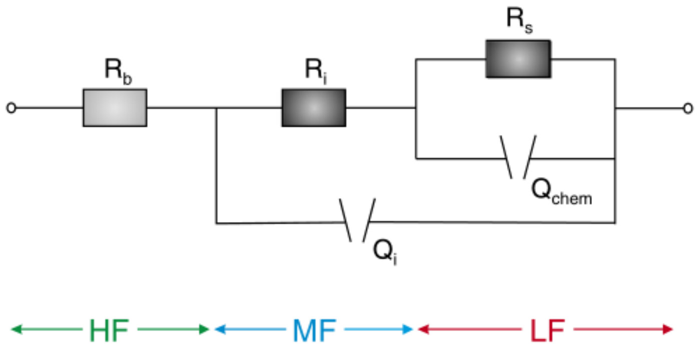

Figure 2.16: Equivalent circuit used to model experimental impedance data of dense thin film LSCF microelectrodes on a YTZ electrolyte. R denotes resistors and Q denotes constant phase elements. Adapted and reprinted from [12].

2.6 Ceramic processing

The microstructure of the final cathode is essential for the performance [6] [17]. In this context, it is important to take into account that the effect of early processing will be inherited throughout the entire fabrication of the SOFC. Careful thought must therefore be given to each step from the initial powder synthesis to the final firing of the finished SOFC. One of the main considerations is to preserve the high specific surface area of the as-synthesized cathode material. By virtue of increasing the number of reaction sites for oxygen reduction, this can help maintain the output voltage high by reducing the cathodic polarization. The overall output voltage of the SOFC strongly depends on the cathodic polarization [18] [40], and can be written as follows [41]:

$$E_{\mathrm{cell}} = E^{\mathrm{rev}} - \eta_{\mathrm{a,a}} - |\eta_{\mathrm{a,c}}| - \eta_{\mathrm{r}} - \eta_{\mathrm{m,a}} - |\eta_{\mathrm{m,c}}| - \eta_{\mathrm{x}} \tag{2.9}$$

where E^{rev} is the reversible potential calculated at a given pressure and temperature by the Nernst equation, $\eta_{\mathrm{a,a}}$ and $\eta_{\mathrm{a,c}}$ are the activation overpotentials at the anode and cathode respectively, η_{r} is the sum of all the ohmic losses, $\eta_{\mathrm{m,a}}$ and $\eta_{\mathrm{m,c}}$ are the concentration overpotentials at the anode and cathode respectively and η_{x} is the deviation from the reversible voltage that occurs due to mixing of the fuel and oxygen or other short-circuits in the cell.

2.6.1 Spray-pyrolysis

Spray-pyrolysis is a fast and inexpensive method for production of various materials in powder form [42] [43]. Metals, metal oxides and non-oxide ceramics can all be produced by this method [42] [43]. This is illustrated by the numerous different compositions synthesized by spray-pyrolysis reported in the literature, including $LaNbO_4$-based powders, $LaMnO_3$- and $LaCoO_3$-powders [44] and $LaFeO_3$-powders [45]. Moreover, the technique can be used to deposit coatings [46]. Spray-pyrolysis offers several advantages compared to other methods for ceramic powder production. The most important ones are high purity, uniform size distribution and small variation in composition [43].

For production of metal oxides, the first step is typically to make an aqueous solution containing the cations of interest [47] [48]. The solution is then atomized and sprayed into a heated rotating reactor [43] [48]. The high temperature results in evaporation of the solvent and decomposition of metal salts into metal oxide powders [48]. Moreover, the residence time in the reactor is very low, on the order of a few seconds [42]. The powder is collected in a cyclone after exiting the reactor. Figure 2.17 shows the process and required apparatus schematically.

The morphology of the resulting particles is characteristic of the method. Very rapid surface precipitation and melt formation result in hollow and spherical, often deformed, particles [42]. This morphology is sometimes referred to as eggshell-like [47], and is shown in Figure 2.18 for a $La_{0.98}Sr_{0.02}NbO_4$ powder.

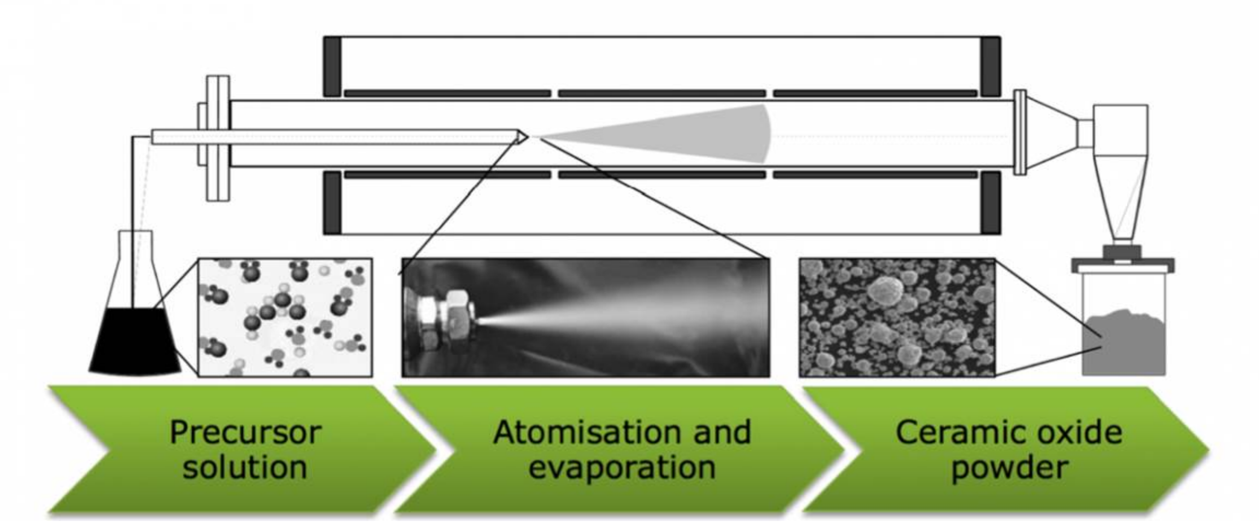

Figure 2.17: Illustration of the spray-pyrolysis method and apparatus. Reprinted from [48].

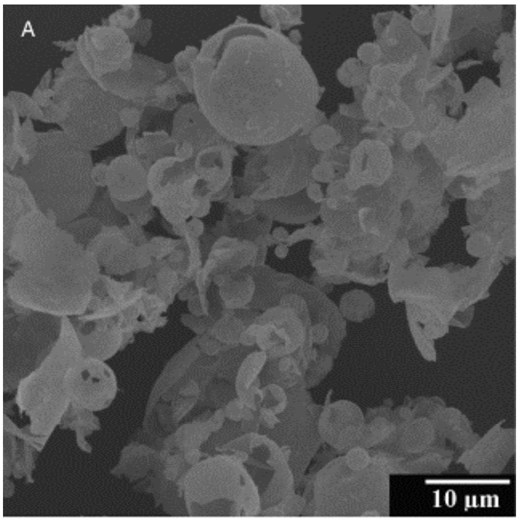

Figure 2.18: Spherical and hollow particles of $La_{0.98}Sr_{0.02}NbO_4$ synthesized by spray-pyrolysis. Reprinted from [47].

2.6.2 Airbrushing

Airbrushing is a technique that can be used for deposition of porous coatings on a substrate. A prime example is porous cathodes on a dense electrolyte. The technique is straightforward and requires only a minimum of equipment, of which a schematic illustration is given in Figure 2.19.

The procedure starts with the preparation of a stable dispersion of the cathode material in a suitable solvent. This step is critical for achieving homogeneous cathodes, and can prove to be challenging. It is important to avoid the presence of agglomerates, as these will sediment fast due to gravitational forces. Ball milling or a similar method is therefore required beforehand. Furthermore, it might be necessary to use a dispersing agent. Once a stable dispersion has been obtained, deposition of the cathode material can begin. The airbrush must be connected to a gas outlet, and argon is a good choice if an inert atmosphere is desired. Finally, a small portion of the dispersion is transferred to the airbrush and sprayed onto the electrolyte pellet. The process can be repeated until the desired thickness has been reached.

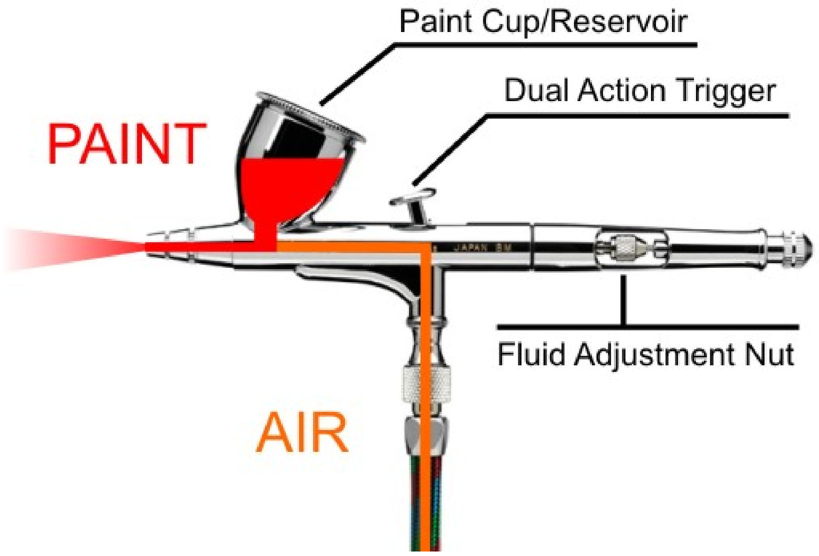
Paint Cup/Reservoir
Dual Action Trigger
PAINT
Fluid Adjustment Nut
AIR

Figure 2.19: Schematic illustration of the cross section of a standard airbrush. Reprinted and adapted from [49].

Chapter 3

Experimental

3.1 Materials

3.1.1 LSCF

Spray-pyrolyzed $La_{0.6}Sr_{0.4}Co_{0.2}Fe_{0.8}O_{3-\delta}$ powder (500 g) was supplied by CerPoTech AS (Trondheim, Norway) without further post-treatments. An aqueous nitrate precursor solution and organic additives were used [47] [48]. Approximately 50 g of the as-synthesized powder was calcined at 725 °C in a Lenton UAF 15/10 furnace. The hold time was 6 hours, and the heating and cooling rate were 3.33 °C/min. Figure 3.1 illustrates this calcination procedure.

Subsequently, the as-calcined powder was ball milled. Two 500 mL bottles and yttria-stabilized zirconia (YTZ) grinding media were used. The grinding media was cleaned by milling for one hour in water and subsequently overnight in ethanol. Furthermore, a diluted solution of nitric acid was used to etch off remaining contaminations before the balls were rinsed by ethanol in an ultrasonic bath and left to dry in a heating cabinet overnight. The as-calcined powder was distributed evenly between the two bottles, and then equal amounts

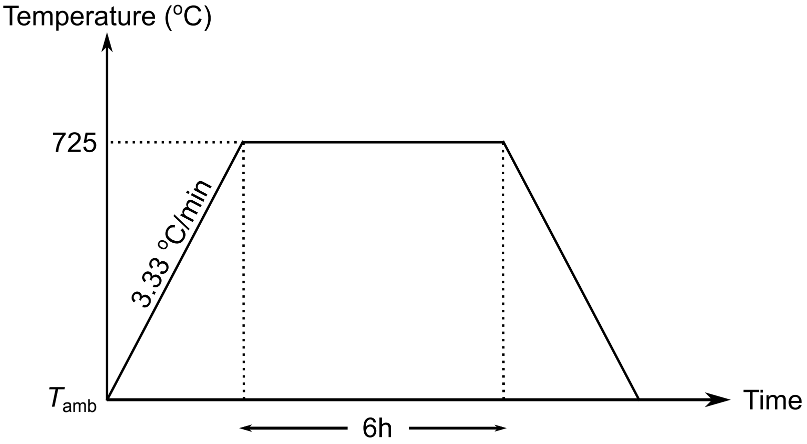

Figure 3.1: Illustration of the calcination procedure for as-synthesized LSCF. The temperature was raised at a rate of 3.33 °C/min from ambient temperature, T_{amb}, to 725 °C. This temperature was maintained for 6 hours, before the temperature was brought back down to T_{amb} at the same rate.

of YTZ was added to both. Approximately 1/2 of each bottle was then occupied. Afterwards, the bottles were shaken vigorously by hand before just enough ethanol to cover the powder and grinding media was added. The bottles were finally placed on a U.S. Stoneware mill and the rpm was set to 120. Milling was conducted for 48 hours. Approximately 5 g of the ball milled powder was subsequently calcined once more at 725 °C for 6 hours according to the procedure in Figure 3.1.

3.1.2 CGO

Spray-pyrolyzed $Ce_{0.9}Gd_{0.1}O_{2-\delta}$ powder (100 g) was supplied by CerPoTech AS (Trondheim, Norway) without further post-treatments. An aqueous nitrate precursor solution was used. One 250 mL bottle and yttria-stabilized zirconia (YTZ) grinding media were used for ball milling of the as-synthesized powder. Cleaning of the grinding media was done according to the same procedure as detailed above for LSCF. The calcined powder and grinding media was transferred to the bottle, between 1/2 and 2/3 of the volume was occupied. Afterwards, the bottle was shaken vigorously by hand before just enough ethanol to cover the powder and grinding media was added. The bottle was finally placed on a U.S. Stoneware mill and the rpm was set to 130. Milling was conducted for 48 hours.

Dense CGO electrolyte pellets were then fabricated by uniaxial pressing with an applied pressure of 70 MPa. Each pellet consisted of approximately 1.1 g and had a diameter of 15 mm. Furthermore, the pellets were sintered at 1300 °C in the Lenton furnace. The hold time was 2 hours, and the heating and cooling rate were 10 °C/min. A schematic illustration of the sintering procedure is given in Figure 3.2. Finally, the geometrical density of each pellet was calculated based on the dimensions measured with a digital caliper. This value was then compared to the theoretical value of 7.26 g/cm^3 stated in PDF 04-002-6160, and the relative densities were found to be consistently higher than 94%. Subsequently, the pellets were grinded by SiC paper on a Struers LaboPol-21. Grinding was done in two steps, starting with grit size FEPA P500 and ending with FEPA P800. Both sides of each pellet were grinded until a reflective surface could be observed by eye.

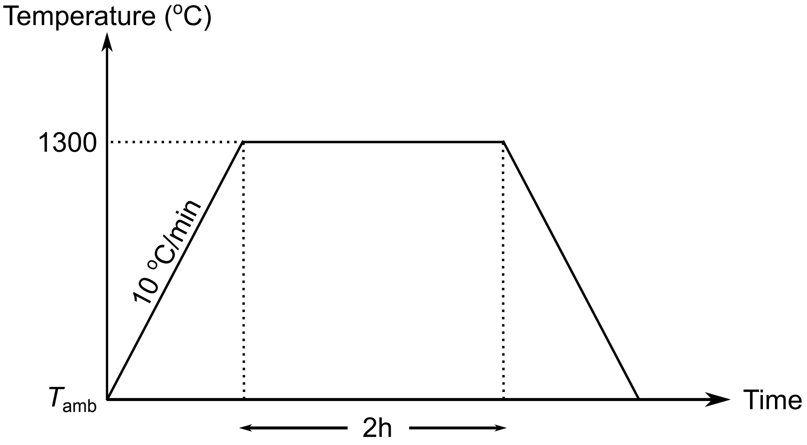

Figure 3.2: Illustration of the sintering procedure for uniaxially pressed CGO pellets. The temperature was raised at a rate of 10 °C/min from ambient temperature, T_{amb}, to 1300 °C. This temperature was maintained for 2 hours, before the temperature was brought back down to T_{amb} at the same rate.

3.2 Symmetric cells

Symmetric cells were then fabricated by depositing LSCF cathodes on a CGO electrolyte by airbrushing. A dispersion of 2 wt% LSCF in ethanol was made and placed in an ultrasonic bath for 30 minutes. Three sintered and grinded CGO pellets were weighed and put on a piece of paper on a hot plate set to 90 °C. The airbrush was connected to an argon gas outlet, and the pressure was adjusted to approximately 0.5 bar. Subsequently, a small amount of the LSCF dispersion was transferred to the airbrush and sprayed onto the pellets. The ethanol was allowed to evaporate from the pellet surfaces before a new layer was applied. Furthermore, the dispersion was shaken vigorously in order to limit sedimentation before applying a new layer. Both sides of the pellets were sprayed, and each pellet was weighed again after the cathode deposition was completed. Finally, the symmetric cells were fired in the Lenton furnace. Initially, two sets of symmetric cells were fired at 1100 °C for 2 hours and 6 hours, respectively. Subsequently, four new sets of symmetric cells were fired at one distinct temperature each. The applied temperatures were 950 °C, 1000 °C, 1050 °C and 1100 °C. Figure 3.3 illustrates the firing procedure for a firing time of 2 hours.

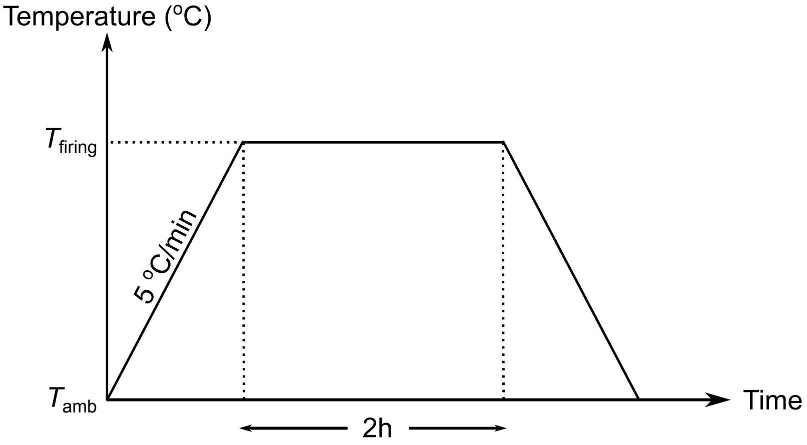

Figure 3.3: Illustration of the firing procedure for the symmetric cells. The heating rate was 5 °C/min from ambient temperature, T_{amb}, to the firing temperature, T_{firing}, which was either 950 °C, 1000 °C, 1050 °C or 1100 °C. T_{firing} was maintained for 2 hours, before the temperature was brought back down to T_{amb} at the same rate.

3.3 Characterization

3.3.1 XRD

Characterization by XRD was done with a Bruker D8 ADVANCE DAVINCI diffractometer with CuK($\alpha_1 + \alpha_2$) radiation of wavelength 1.54 Å.

3.3.1.1 LSCF

In order to verify that the powder had become phase pure after calcination, a diffractogram was recorded of the as-calcined powder. Furthermore, diffractograms were recorded of the ball milled powder and of the powder calcined once more after ball milling. In all cases, the powder was lightly grinded by hand in an agate mortar beforehand. The parameters for the diffractograms are given in Table 3.1, and phase purity was assessed by comparison with PDF 04-017-2448.

Table 3.1: Parameter values for the diffractograms of LSCF recorded by the Bruker D8 ADVANCE DAVINCI diffractometer.

Parameter	Value
Scan time	120 min
Start angle	20.00°
Stop angle	80.00°
Step size	0.013°
Time per step	1.520 s

3.3.1.2 CGO

In order to verify that no secondary phase had been introduced during ball milling, a diffractogram was recorded afterwards. The powder was lightly grinded by hand in an agate mortar beforehand. Furthermore, the parameters for the diffractograms are given in Table 3.2, and phase purity was assessed by comparison with PDF 04-002-6160.

Table 3.2: Parameter values for the diffractogram of CGO recorded by the Bruker D8 ADVANCE DAVINCI diffractometer.

Parameter	Value
Scan time	120 min
Start angle	5.00°
Stop angle	75.00°
Step size	0.013°
Time per step	1.300 s

3.3.1.3 Chemical compatibility

The chemical compatibility of LSCF and CGO was investigated by mixing 0.401 g calcined and ball milled LSCF with 0.400 g ball milled CGO. A single pellet was made by uniaxial pressing with an applied pressure of 60 MPa. The pellet had a diameter of 10 mm, and was sintered at 1300 °C for 2 hours in the Lenton furnace with a heating and cooling rate of 10 °C/min. The procedure is shown in Figure 3.2. Subsequently, it was crushed and grinded by hand in an agate mortar, and a diffractogram was recorded of the resulting powder. The parameters were identical as for the diffractograms recorded of LSCF, which are listed in Table 3.1.

3.3.2 SEM

Characterization by SEM was done with a Hitachi S-3400N. Sputtering with gold was done by an Edwards Sputter Coater S150B.

3.3.2.1 LSCF

After ball milling for 48 hours, a small amount of the slurry was transferred to a glass container and diluted heavily with ethanol. The glass container was then put in an ultrasonic bath to ensure good mixing. Afterwards, a droplet of the slurry was put directly onto a sample holder. The ethanol was allowed to evaporate before the sample was subjected to gold sputtering for 15 seconds. Finally, SEM images were recorded. The accelerating voltage was 5 kV, secondary electrons were used and the working distance was 4.2 mm.

3.3.2.2 CGO

After ball milling for 48 hours, a small amount of the slurry was transferred to a glass container and diluted heavily with ethanol. The glass container was then put in an ultrasonic bath to ensure good mixing. Afterwards, a droplet of the slurry was put directly onto a sample holder. The ethanol was allowed to evaporate before the sample was subjected to gold sputtering for 15 seconds. Finally, SEM images were recorded. The accelerating voltage was in the 3.5-4 kV range, secondary electrons were used and the working distance was in the 4.1-4.4 mm range.

3.3.2.3 Symmetric cells

SEM images of the symmetric cells fired at 950 °C, 1000 °C, 1050 °C and 1100 °C were recorded. Both the cathode surfaces and the cross sections were investigated.

For investigation of the cathode surface, the symmetric cell was attached to a sample holder by carbon tape and sputter coated with gold for approximately 30 seconds. SEM images were then recorded. The accelerating voltage was in the 5-10 kV range and secondary electrons were used. Afterwards, the same cell was cut in half by a Struers Minitom. One of the pieces was cast in epoxy and left to harden for 12 hours. Subsequently, the surface of the epoxy unit was grinded and polished on a Struers Tegramin-20 until the cross section of the symmetric cell was exposed. Grinding with Struers SiC papers of three different grit sizes was done in the following sequence: FEPA P500, FEPA P800 and FEPA P1200. Polishing by DiaPro diamond suspensions on increasingly fine Struers polishing plates then followed. The order of the plates used was: Largo (9 μm), Dur (3μm) and Mol (1μm). Furthermore, the entire epoxy unit was cleaned in water in an ultrasonic bath before each new grinding or polishing step. Subsequently, the epoxy unit was sputter coated with gold for approximately 45 seconds. A narrow slit was cut in a piece of aluminium foil, which was then aligned with the exposed cross section of the symmetric cell. The aluminium foil was wrapped tightly around the rest of the epoxy, after which conductive carbon cement was applied to ensure contact between the two. Furthermore, a piece of carbon tape was extended from the perimeter of the slit down to the sample holder. Finally, SEM images were recorded. The accelerating voltage was 10 kV and secondary electrons were used.

3.3.3 Electrochemical impedance spectroscopy

Electrochemical impedance spectroscopy was carried out on the symmetric cells using a tubular furnace equipped with the ProboStat™ sample holder setup for circular samples from NorECs. An Alpha-A High Performance Frequency Analyser from Novocontrol was used to analyze the impedance. All measurements were done in pure oxygen at open-circuit voltage. The applied AC signal had an amplitude of 1 volt, and the frequency range investigated was 3 MHz to 0.01 Hz.

Before starting measurements, platinum paste had to be applied to the cathode surfaces in order to ensure sufficient electrical contact with the platinum leads of the apparatus. One of the cathodes was covered and allowed to dry in a heating cabinet set to 90-120 °C for approximately 10 minutes. Subsequently, the cell was flipped over and the process was repeated for the second cathode. Furthermore, the fabrication process had left deposited cathode around the circumference of the electrolyte pellet, which had to be removed in order to avoid short-circuiting. This was done by manual grinding on a SiC FEPA P1200 paper. Finally, the symmetric cell was placed in the ProboStat™, where it was clamped between two sheets of platinum foil. A mechanical spring system was used to ensure that the cell was kept tightly in place.

The effect of firing time was investigated briefly initially. This was done by measuring the impedance response at 700 °C for the symmetric cells fired at 1100 °C for 2 hours and 6 hours, respectively. The heating rate was 5 °C/min, and the temperature was allowed to stabilize for one hour before the measurement started.

Then, the effect of the firing temperature was evaluated by measuring the impedance response of one symmetric cell fired at 950 °C, 1000 °C, 1050 °C and 1100 °C, respectively. The impedance was now measured at 600 °C, 700 °C and 800 °C. As before, the heating rate was

5 °C/min, and for each temperature change the temperature was allowed to stabilize for one hour before the measurement started. The dimensions of the symmetric cell were afterwards determined by a digital caliper. Finally, the ZSimpWin 3.21 software was used to fit the experimentally obtained data with an equivalent electrical circuit. Before fitting, the inductance was manually removed from the data sets. In order to determine the ASR for a single cathode, the ASR given by the software was divided by two and multiplied with the geometrical cathode area as measured by the digital caliper.

3.3.4 BET

The specific surface area of LSCF after two different calcination procedures were determined by a Micromeritics TriStar 3000 and the BET method [50]. $N_2(g)$ was used as the adsorptive, and the isotherms were recorded at 77 K.

Initially, the powder that had been calcined at 725 °C and ball milled for 48 hours was investigated. Two samples were prepared by transferring 0.2073 g to one sample tube and 1.4065 g to another. Both samples were then degassed overnight at 250 °C. Finally, the sample tubes were loaded in the instrument and the specific surface areas were measured.

Subsequently, a pellet of the same powder was fabricated by uniaxial pressing with an applied pressure of 60 MPa. The pellet had a diameter of 15 mm, and was calcined in the Lenton furnace at 900 °C for 6 hours with a heating and cooling rate of 3.33 °C/min. The calcination procedure is shown in Figure 3.4. It was afterwards crushed and grinded by hand in a mortar, and the resulting powder was distributed relatively evenly between two separate sample tubes. One sample tube contained 0.4629 g, whereas the other contained 0.7184 g. Both samples were degassed overnight at 250 °C. Finally, the sample tubes were loaded in the instrument and the specific surface areas were measured.

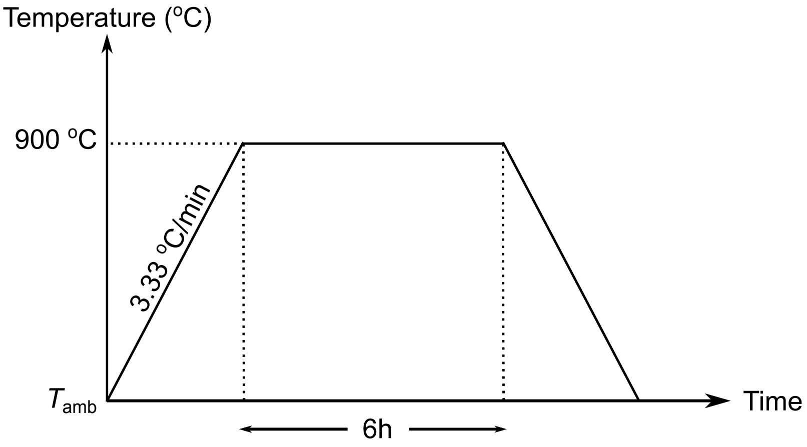

Figure 3.4: Illustration of the calcination procedure for the LSCF pellet investigated by BET. The temperature was raised at a rate of 3.33 °C/min from ambient temperature, T_{amb}, to 900 °C. This temperature was maintained for 6 hours, before the temperature was brought back down to T_{amb} at the same rate.

3.3.5 Dilatometry

The volume change of LSCF and CGO as a function of temperature was determined by a Netzsch 402C dilatometer. One pellet of each composition was made by uniaxial pressing with an applied pressure of 60 MPa. Both pellets had a diameter of 5 mm, and the length was 4.14 mm and 4.26 mm for the LSCF and CGO pellet, respectively. The measurements were done in the 25-1300 °C temperature range with a heating rate of 10 °C/min, and were carried out in air.

Chapter 4

Results

4.1 LSCF

4.1.1 Phase purity

The phase purity of the as-calcined powder was assessed by XRD. Figure 4.1 shows the recorded diffractogram in addition to the previously recorded pattern for $La_{0.6}Sr_{0.4}Co_{0.2}Fe_{0.8}O_3$ given in PDF 04-017-2448. The correspondence was observed to be excellent, and it was concluded that the powder was phase pure. However, two additional reflections at $2\theta \approx 25°$ and $2\theta \approx 36°$ were seen after ball milling. These are marked by asterisks in Figure 4.2. The same result was observed once more by repeating the calcination and ball milling for another batch, which indicated that one or more secondary phases had been introduced during milling. However, these reflections were observed to disappear when the ball milled powder was calcined once more afterwards. This is also shown in Figure 4.2. Furthermore, the small reflections at $2\theta \approx 29°$ and $2\theta \approx 31°$ observed in all three diffractograms were caused by the apparatus.

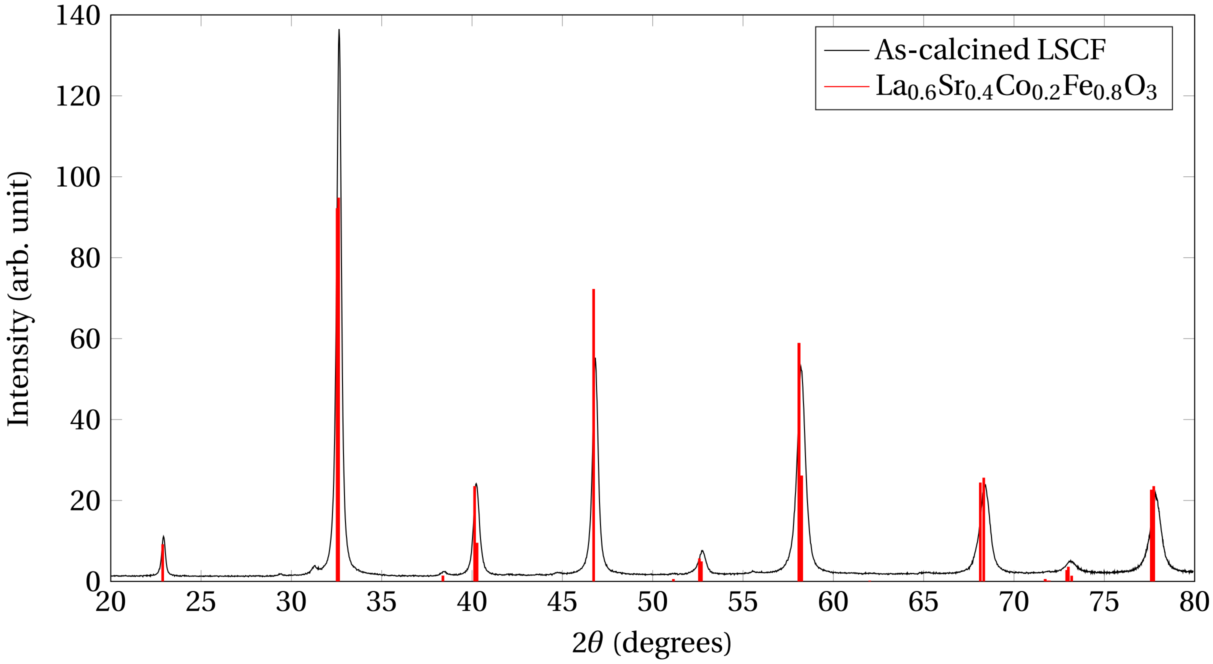

Figure 4.1: Diffractogram of the as-calcined LSCF powder and the previously identified pattern for $La_{0.6}Sr_{0.4}Co_{0.2}Fe_{0.8}O_3$ given in PDF 04-017-2448. The powder appeared to be phase pure.

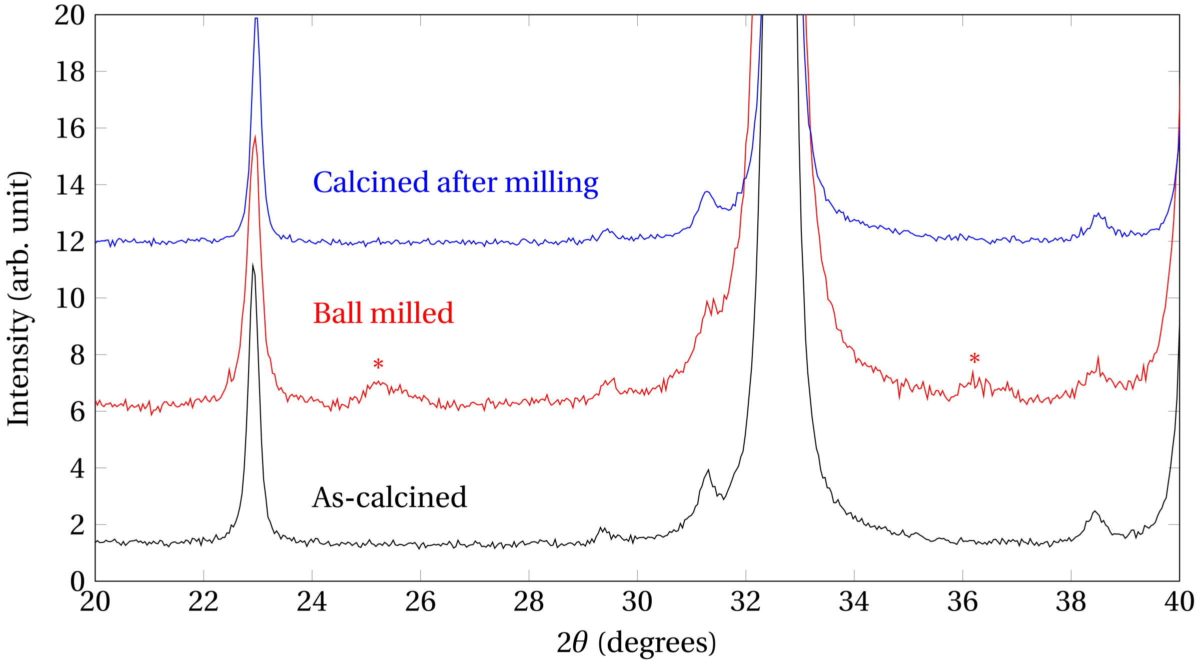

Figure 4.2: Comparison of three diffractograms of LSCF: (i) as-calcined, (ii) ball milled and (iii) calcined once more after ball milling. The two reflections marked by asterisks indicated the presence of one or more secondary phases after milling. However, these were observed to disappear after repeated calcination at the same temperature. The reflections at $2\theta \approx 29°$ and $2\theta \approx 31°$ observed in all three diffractograms were caused by the apparatus.

4.1.2 Ball milling

Figure 4.3 shows the effect of the applied ball milling procedure on the LSCF particle size. An image of the as-synthesized powder is included in Figure 4.3a for reference purposes, whereas Figure 4.3b-4.3d shows images at various magnifications after ball milling. The spherical, eggshell-like agglomerates typical of spray pyrolysis were clearly evident in the as-synthesized powder. However, these agglomerates seemed to have been broken down after ball milling. Furthermore, the primary particle size appeared to be less than 100 nm.

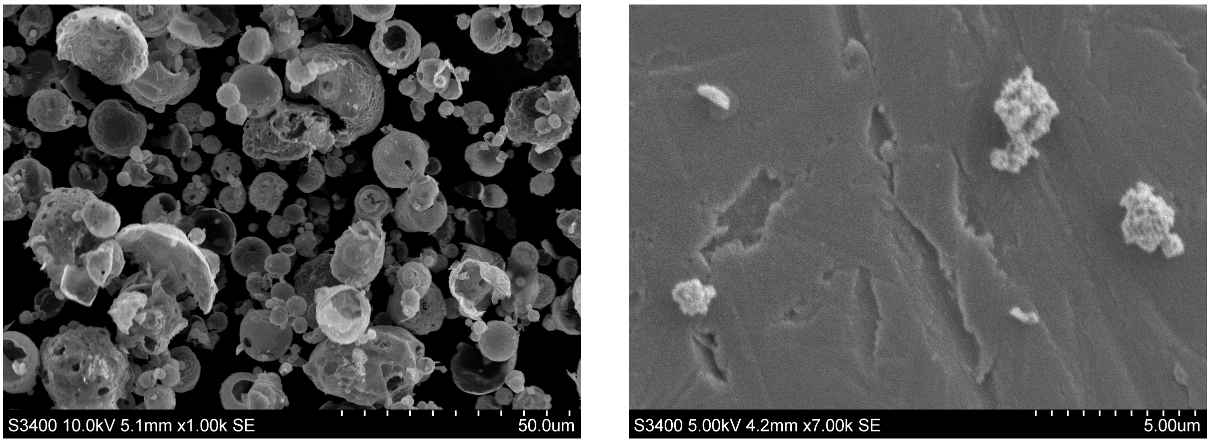
S3400 10.0kV 5.1mm x1.00k SE
50.0um
S3400 5.00kV 4.2mm x7.00k SE
5.00um

(a) As-synthesized, 1000×

(b) Ball milled, 7000×

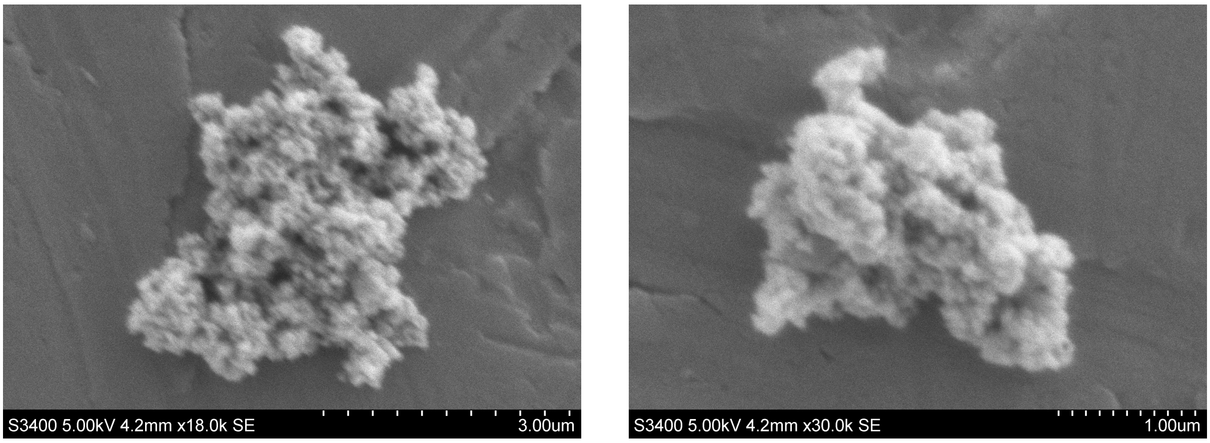
S3400 5.00kV 4.2mm x18.0k SE
3.00um
S3400 5.00kV 4.2mm x30.0k SE
1.00um

(c) Ball milled, 18000×

(d) Ball milled, 30000×

Figure 4.3: The effect of ball milling for 48 hours at 120 rpm on the particle size of LSCF.

4.1.3 Sintering kinetics

The sintering kinetics of calcined and ball milled LSCF were assessed by dilatometry. Figure 4.4 shows the recorded volume change of LSCF as a function of temperature. Furthermore, the sintering rate curve was obtained by numerical differentiation of the dilatometry data. Densification was observed to initiate at around 850 °C and continued to approximately 1100 °C. The maximum sintering rate occurred at approximately 1000 °C.

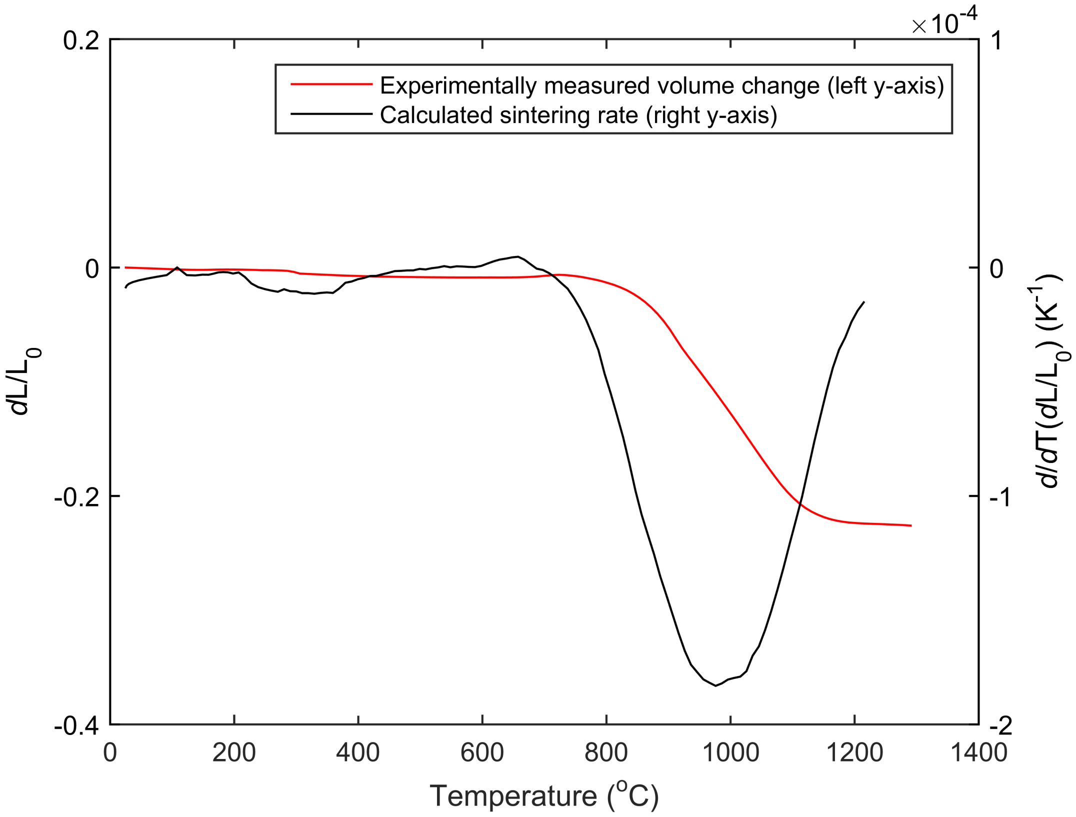

Figure 4.4: The volume change of LSCF measured by dilatometry plotted as a function of temperature. Also shown is the sintering rate curve obtained by numerical differentiation of the dilatometry data. Densification began at temperatures around 850 °C and continued to approximately 1100 °C. Furthermore, the sintering rate was at its maximum at approximately 1000 °C. Note that the scale of the right y-axis is multiplied with 10^{-4}.

4.1.4 Specific surface area

The specific surface areas of LSCF measured by the BET method are listed in Table 4.1, and the recorded surface area plots can be found in Appendix A. The values after calcination at 725 °C were quite high, and a strong temperature dependence was documented. Furthermore, the corresponding calculated particle radii are also listed in Table 4.1. These were determined by assuming spherical particles, and the complete derivation is detailed in Appendix B. The calculated values of approximately 20 nm after calcination at 725 °C and subsequent ball milling were consistent with the primary particle sizes seen from SEM images in Figure 4.3.

Table 4.1: Measured specific surface areas and calculated particle sizes of LSCF after two different calcination procedures.

	Sample 1	Sample 2
Calcined 725 °C		
Specific surface area [m^2/g]	26.86 ± 0.15	25.11 ± 0.29
Calculated radius [nm]	17.7	18.9
Calcined 900 °C		
Specific surface area [m^2/g]	1.68 ± 0.01	1.70 ± 0.01
Calculated radius [nm]	282.9	279.5

4.2 CGO

4.2.1 Phase purity

The phase purity of ball milled CGO was assessed by XRD. Figure 4.5 shows the recorded diffractogram in addition to the previously recorded pattern for $Ce_{0.9}Gd_{0.1}O_2$ given in PDF 04-002-6160. The correspondence was observed to be excellent, and it was concluded that the powder was phase pure.

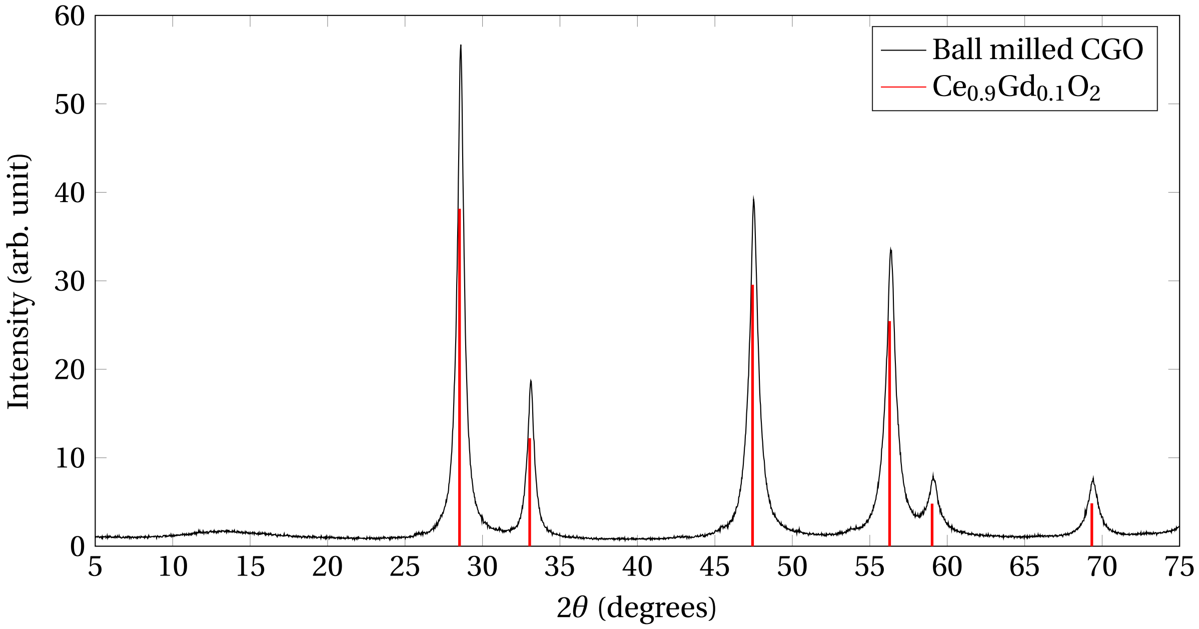

Figure 4.5: Diffractogram of the ball milled CGO and the previously identified pattern for $Ce_{0.9}Gd_{0.1}O_2$ given in PDF 04-002-6160. The powder appeared to be phase pure.

4.2.2 Ball milling

Figure 4.6 shows the effect of the applied ball milling procedure on the CGO particle size. An image of the as-synthesized powder is included in Figure 4.6a for reference purposes, whereas Figure 4.6b was recorded after ball milling. As for LSCF, the spherical, eggshell-like agglomerates were obvious in the as-synthesized powder. These appeared to have been broken down after ball milling, and the primary particle size was around 100 nm.

4.2.3 Sintering kinetics

The sintering kinetics of ball milled CGO were assessed by dilatometry. Figure 4.7 shows the recorded volume change of CGO as a function of temperature. Furthermore, the sintering rate curve was obtained by numerical differentiation of the dilatometry data. Densification was observed to initiate at around 600 °C and seemed to continue to temperatures above 1300 °C. The maximum sintering rate occurred at approximately 900 °C.

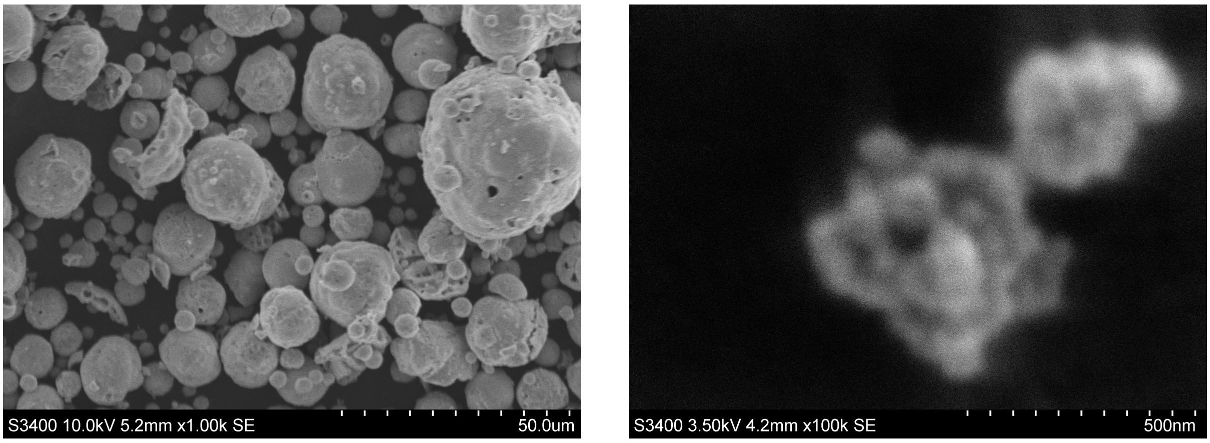
S3400 10.0kV 5.2mm x1.00k SE
50.0um
S3400 3.50kV 4.2mm x100k SE
500nm

(**a**) As-synthesized, 1000×

(**b**) Ball milled, 100000×

Figure 4.6: The effect of ball milling for 48 hours at 130 rpm on the particle size of CGO.

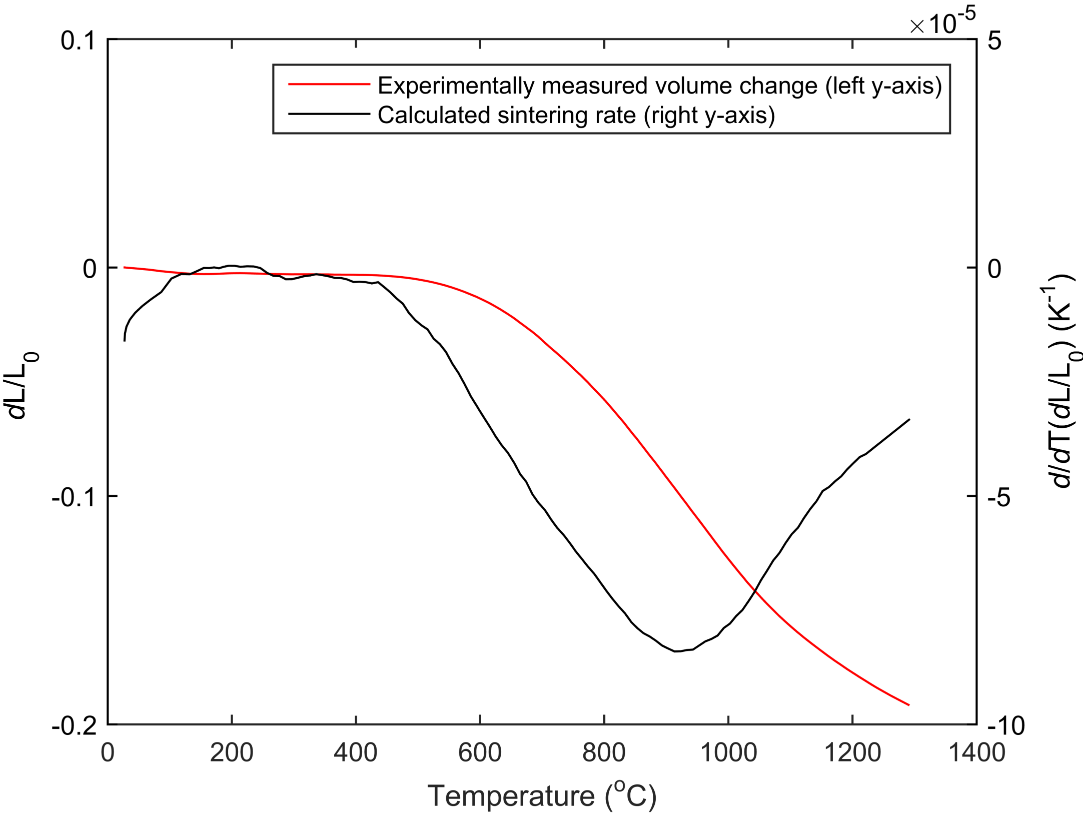

Figure 4.7: The volume change of CGO measured by dilatometry plotted as a function of temperature. Also shown is the sintering rate curve obtained by numerical differentiation of the dilatometry data. Densification began at temperatures around 600 °C and seemed to continue to temperatures above 1300 °C. Furthermore, the sintering rate was at its maximum around 900 °C. Note that the scale of the right y-axis is multiplied with 10^{-5}.

4.3 Symmetric cells

4.3.1 Chemical compatibility

The chemical compatibility of LSCF and CGO was assessed by XRD. Figure 4.8 shows the recorded diffractogram of powder from the sintered pellet consisting of equal weight fractions of LSCF and CGO. As can be seen, every reflection can be accounted for by the combined diffractograms of as-calcined LSCF and ball milled CGO, which are also shown in Figure 4.8. As-calcined LSCF was chosen as reference here since the secondary phase(s) introduced during ball milling disappeared when the pellet was sintered. Based on the obtained diffractogram, no chemical reaction appeared to have occurred between LSCF and CGO.

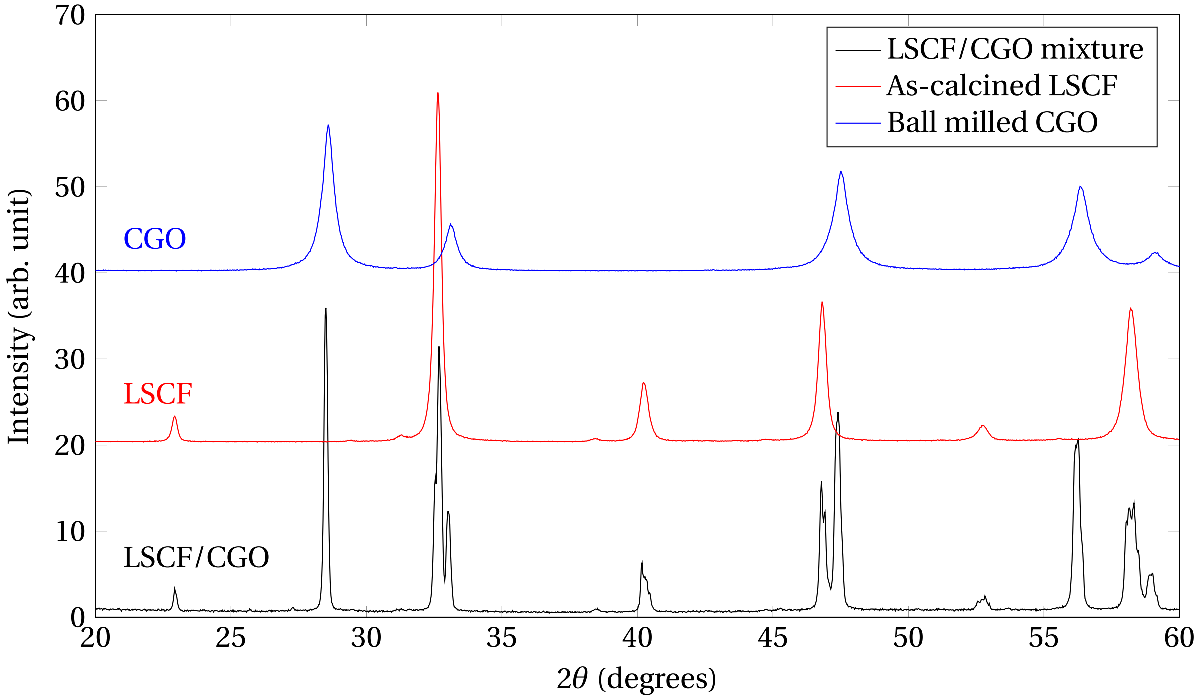

Figure 4.8: Investigation of the chemical compatibility of LSCF and CGO. A diffractogram of the powder from the LSCF/CGO pellet sintered at 1300 °C for 2 hours is shown at the bottom. The reflections can be accounted for by the combined diffractograms of as-calcined LSCF and ball milled CGO.

4.3.2 Oxygen reduction kinetics

The kinetics of the oxygen reduction reaction were assessed by EIS in pure oxygen atmosphere. Initially, the effect of the firing time was investigated. Figure 4.9 shows the data recorded at 700 °C for symmetric cells fired at 1100 °C for 2 hours and 6 hours, respectively. Note that the data has been normalized to Re(Z)=0 to better visualize the effect on the ASR. However, the original data can be found in a non-normalized Nyquist plot in Appendix C. It is evident that the ASR was much larger for the longer firing time. Consequently, all cells fabricated subsequently were fired for 2 hours.

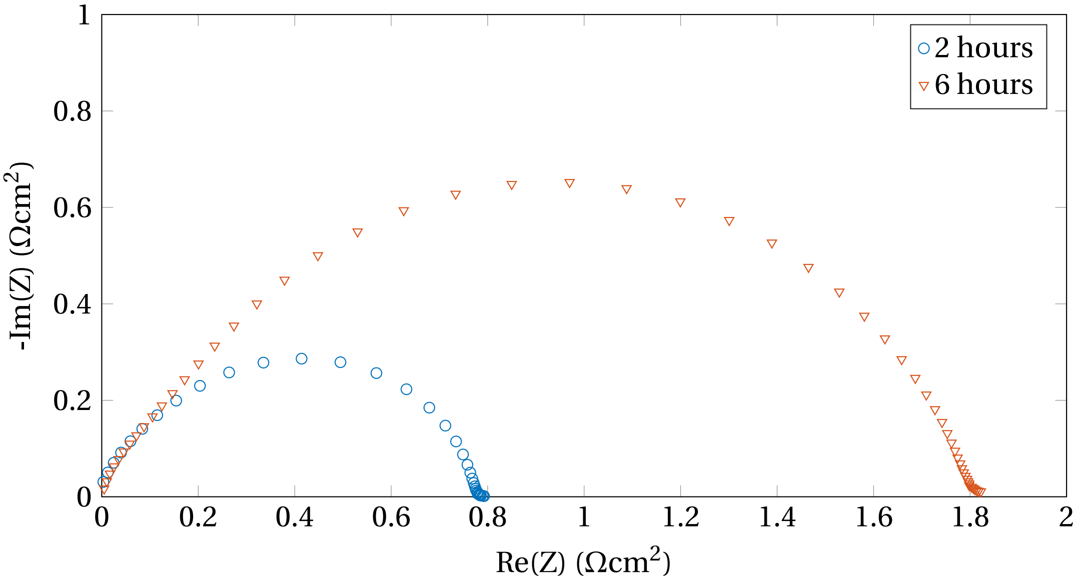

Figure 4.9: Electrochemical impedance data recorded at 700 °C in pure oxygen for symmetric cells fired at 1100 °C for 2 hours and 6 hours, respectively. The data have been normalized to Re(Z)=0.

The effect of the firing temperature was investigated next. Figure 4.10 shows the impedance data recorded at 600 °C for symmetric cells fired at 950 °C, 1000 °C, 1050 °C and 1100 °C. Figure 4.11 and 4.12 show the same for the impedance data recorded at 700 °C and 800 °C, respectively. Note that all data have been normalized to Re(Z)=0 to better visualize the effect on the ASR. However, the original data can be found in non-normalized Nyquist plots in Appendix C. The ASR was observed to increase continuously with increasing firing temperature for all three measurement temperatures. Furthermore, the ASR for all the symmetric cells was observed to decrease with increasing measurement temperature.

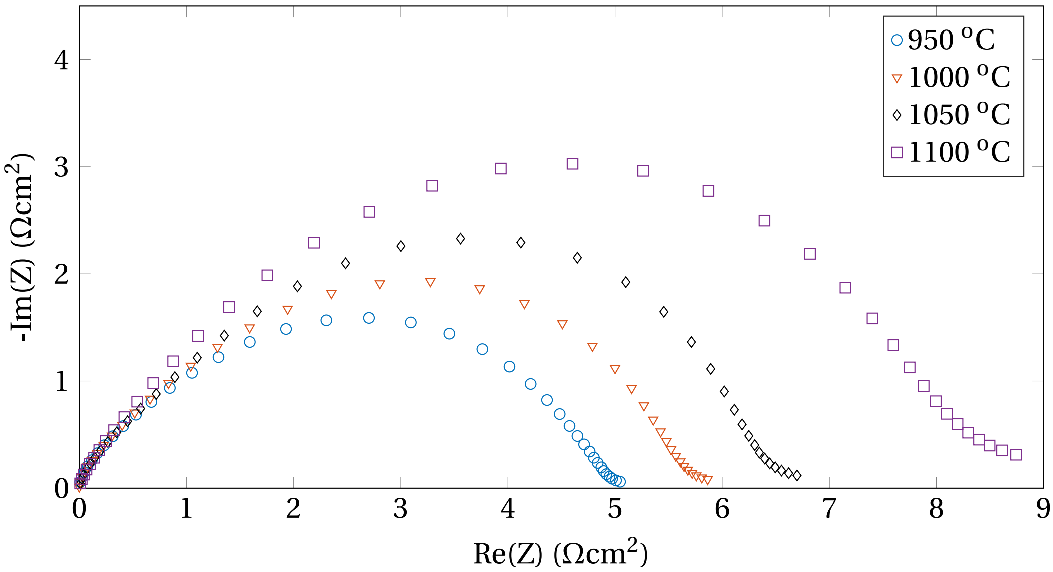

Figure 4.10: Electrochemical impedance data recorded at 600 °C in pure oxygen for symmetric cells fired at 950 °C, 1000 °C, 1050 °C and 1100 °C. All data has been normalized to Re(Z)=0.

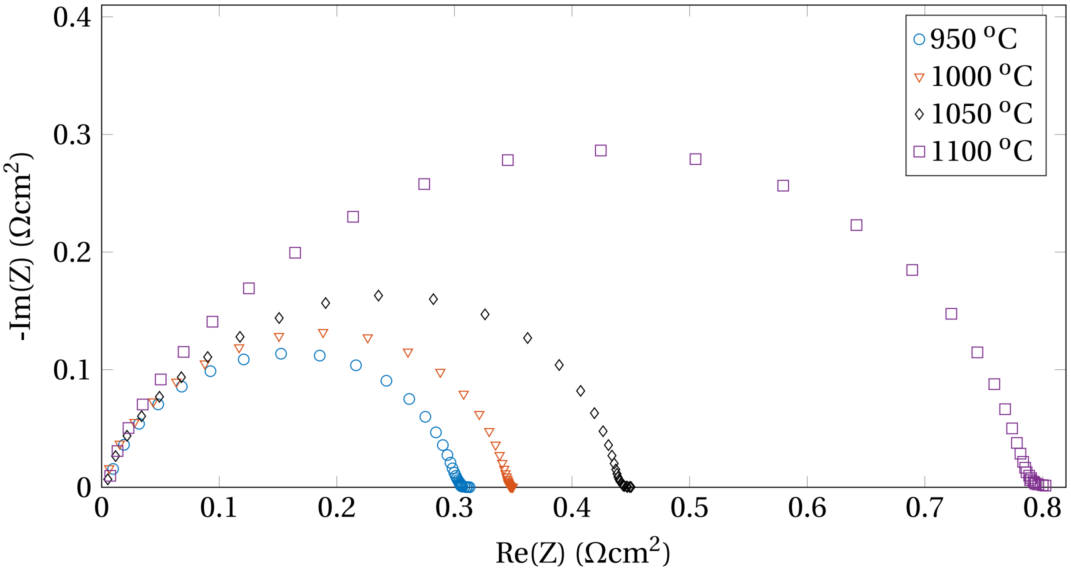

Figure 4.11: Electrochemical impedance data recorded at 700 °C in pure oxygen for symmetric cells fired at 950 °C, 1000 °C, 1050 °C and 1100 °C. All data has been normalized to Re(Z)=0.

The experimental data was modeled by the equivalent electrical circuit shown schematically in Figure 4.13, where R denotes a resistor and Q denotes a constant phase element. Table 4.2 contains the calculated ASR values based on the equivalent circuit. These were used to create the Arrhenius plot shown in Figure 4.14. Furthermore, the activation energies for the oxygen reduction were calculated from the slopes of the least-square fitted data sets shown

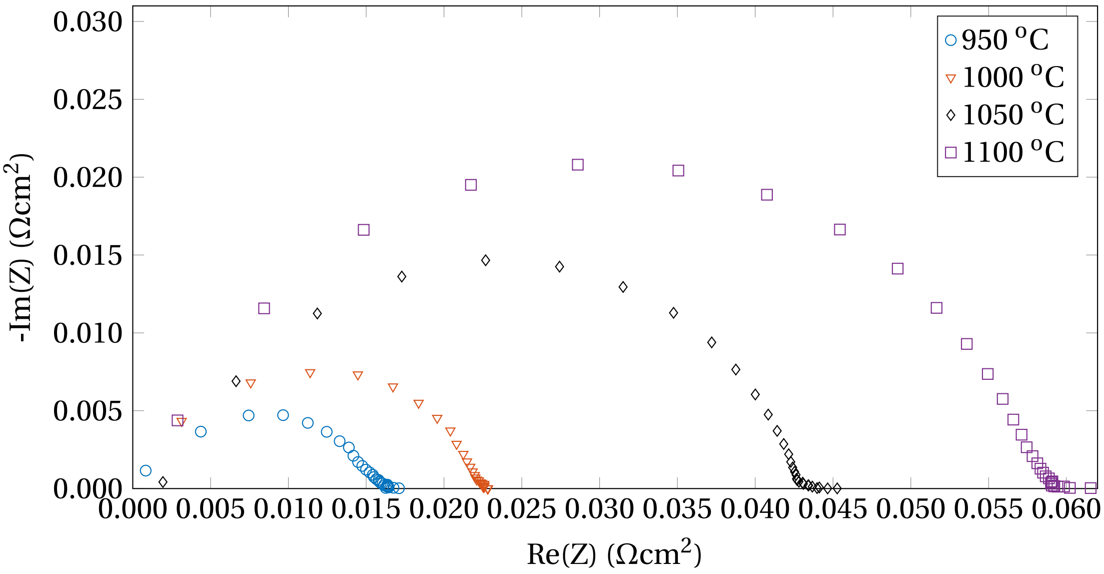

Figure 4.12: Electrochemical impedance data recorded at 800 °C in pure oxygen for symmetric cells fired at 950 °C, 1000 °C, 1050 °C and 1100 °C. All data has been normalized to Re(Z)=0.

in Figure 4.14. The calculated values for cathodes fired at each of the four temperatures are listed in Table 4.3.

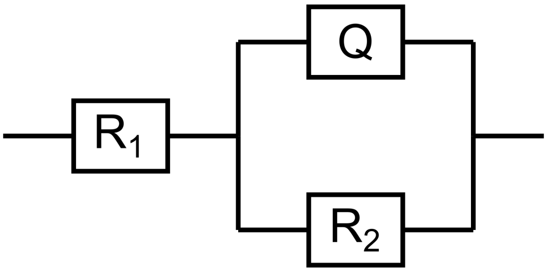

Figure 4.13: Equivalent electrical circuit used to model the experimental impedance data. R denotes a resistor and Q denotes a constant phase element.

Table 4.2: ASR values obtained from the equivalent circuit. The value at each of the three measurement temperatures, i.e. 600 °C, 700 °C and 800 °C, is shown as a function of the firing temperature, i.e. 950 °C, 1000 °C, 1050 °C and 1100 °C.

ASR [Ωcm^2]	950 °C	1000 °C	1050 °C	1100 °C
600 °C	2.52	2.91	3.30	4.35
700 °C	0.15	0.17	0.22	0.39
800 °C	0.01	0.01	0.02	0.03

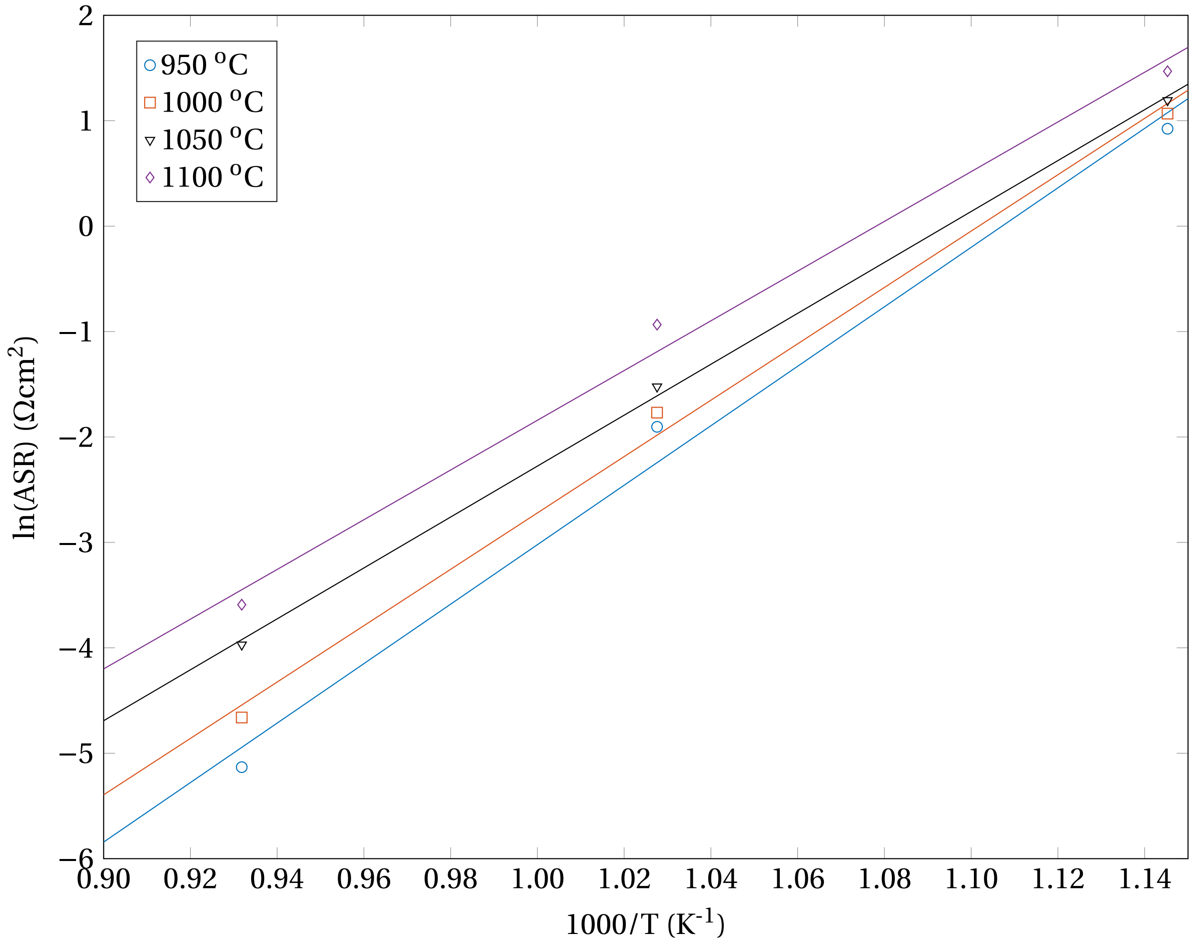

Figure 4.14: The natural logarithm of the ASR values plotted as a function of the reciprocal measurement temperature for each of the four firing temperatures, i.e. 950 °C, 1000 °C, 1050 °C and 1100 °C. Values of the ASR were obtained from the equivalent circuit modeling, and the trend lines were obtained by least-square fitting.

Table 4.3: Activation energy, E_a, for the oxygen reduction reaction listed as a function of firing temperature, T_firing. The values were calculated from the slopes of the least-square fitted lines in Figure 4.14, and are given by two different units.

T_firing (°C)	E_a (kJ/mol)	E_a (eV)
950	234.5	2.43
1000	222.3	2.30
1050	200.8	2.08
1100	196.1	2.03

4.3.3 Cross section and cathode surface

Figure 4.15 shows SEM images of the cross sections of the symmetric cells fired at 950 °C, 1000 °C, 1050 °C and 1100 °C. It is evident that the deposited cathode layers were uneven. The maximum width of the layers appeared to be approximately 10 μm, whereas they were no more than a couple of microns wide in other areas. The same cross sections are shown at higher magnifications in Figure 4.16. These images further confirmed that the width of the deposited cathode layer varied along the length of the cross section.

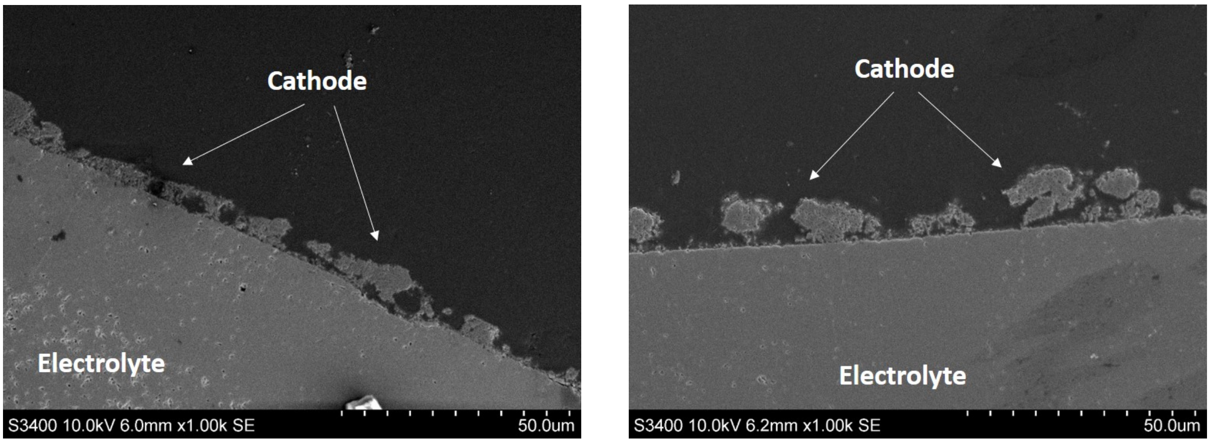
Cathode
Electrolyte
S3400 10.0kV 6.0mm x1.00k SE
50.0um
Cathode
Electrolyte
S3400 10.0kV 6.2mm x1.00k SE
50.0um

(a) Firing temperature 950 °C, 1000×

(b) Firing temperature 1000 °C, 1000×

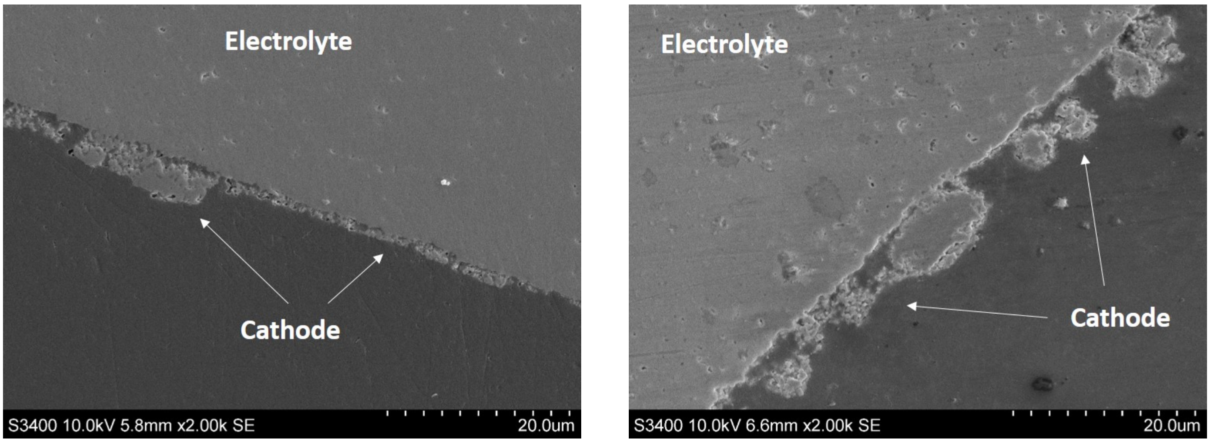
Electrolyte
Cathode
S3400 10.0kV 5.8mm x2.00k SE
20.0um
Electrolyte
Cathode
S3400 10.0kV 6.6mm x2.00k SE
20.0um

(c) Firing temperature 1050 °C, 2000×

(d) Firing temperature 1100 °C, 2000×

Figure 4.15: Low magnification SEM images of the cross sections of symmetric cells fired at 950 °C, 1000 °C, 1050 °C and 1100 °C, respectively.

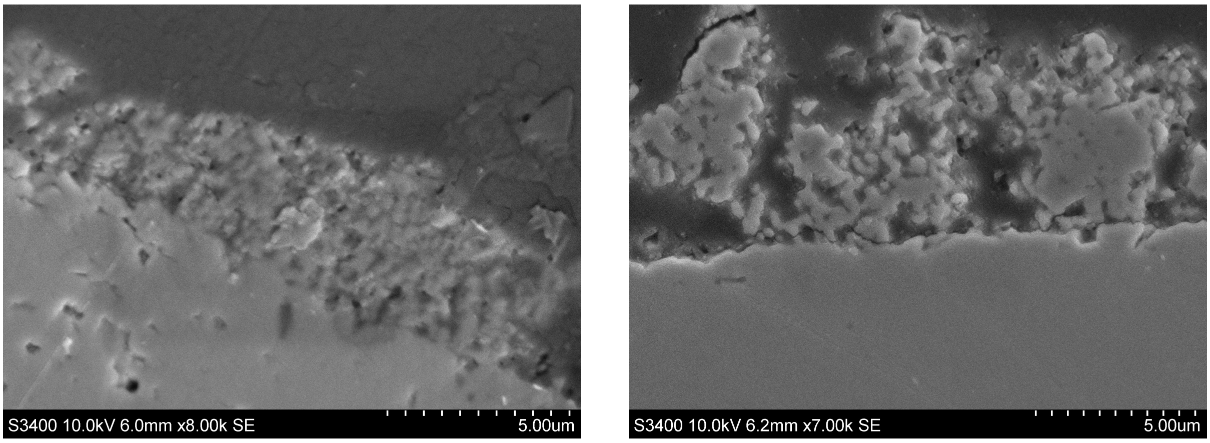
S3400 10.0kV 6.0mm x8.00k SE
5.00um
S3400 10.0kV 6.2mm x7.00k SE
5.00um

(a) Firing temperature 950 °C, 8000×

(b) Firing temperature 1000 °C, 7000×

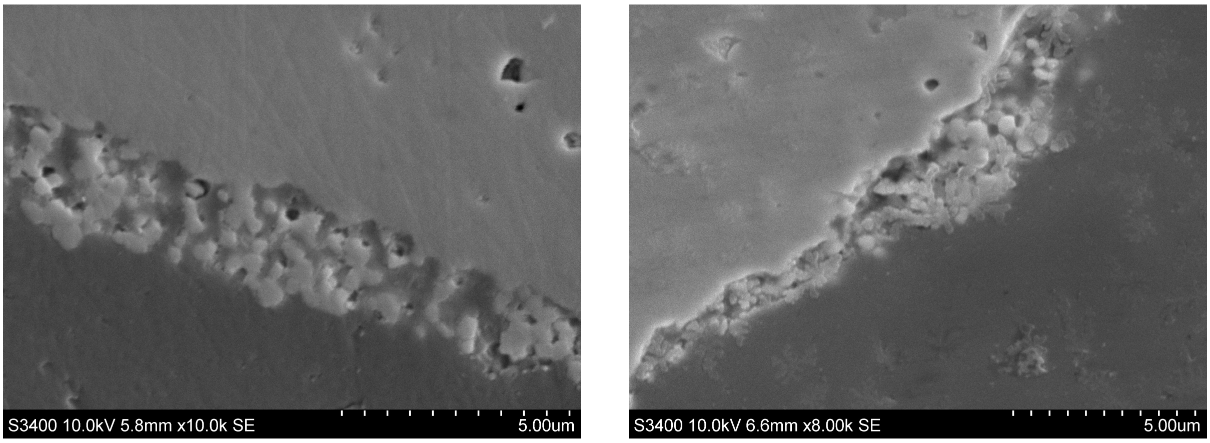
S3400 10.0kV 5.8mm x10.0k SE
5.00um
S3400 10.0kV 6.6mm x8.00k SE
5.00um

(c) Firing temperature 1050 °C, 10000×

(d) Firing temperature 1100 °C, 8000×

Figure 4.16: Higher magnification SEM images of the cross sections of symmetric cells fired at 950 °C, 1000 °C, 1050 °C and 1100 °C, respectively.

Figure 4.17 shows the cathode surfaces of symmetric cells fired at 950 °C, 1000 °C, 1050 °C and 1100 °C. It is evident that all cathodes contained large agglomerates. The same cathode surfaces are shown at higher magnifications in Figure 4.18. From these images it is clear that the cathodes were porous. Furthermore, it appeared that the cathodes became gradually denser as the firing temperature was increased.

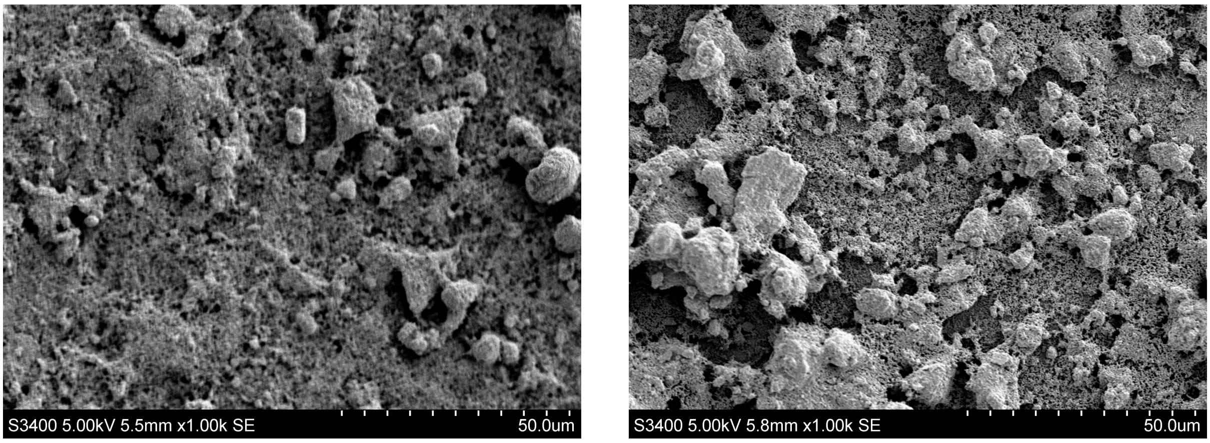
S3400 5.00kV 5.5mm x1.00k SE
50.0um
S3400 5.00kV 5.8mm x1.00k SE
50.0um

(a) Firing temperature 950 °C, 1000×

(b) Firing temperature 1000 °C, 1000×

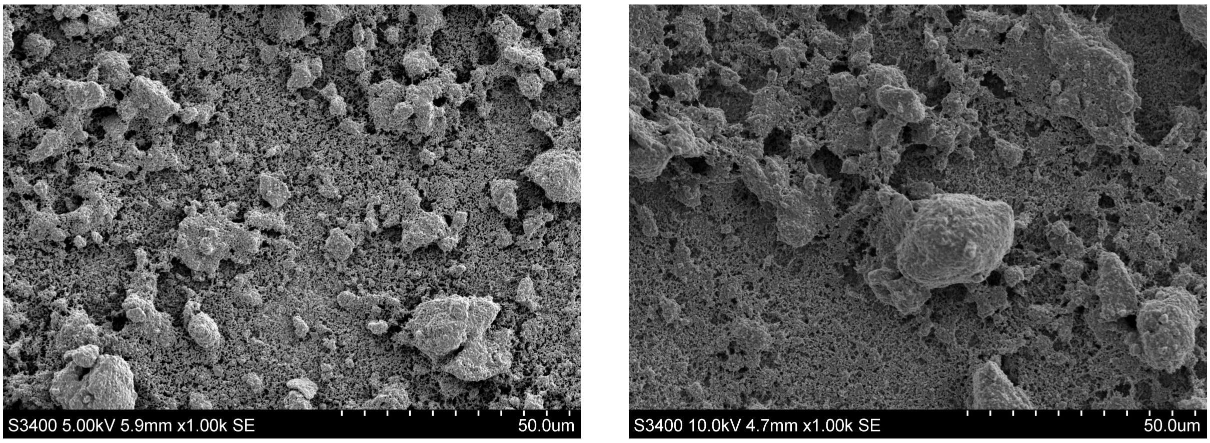
S3400 5.00kV 5.9mm x1.00k SE
50.0um
S3400 10.0kV 4.7mm x1.00k SE
50.0um

(c) Firing temperature 1050 °C, 1000×

(d) Firing temperature 1100 °C, 1000×

Figure 4.17: Low magnification SEM images of the cathode surfaces of symmetric cells fired at 950 °C, 1000 °C, 1050 °C and 1100 °C, respectively.

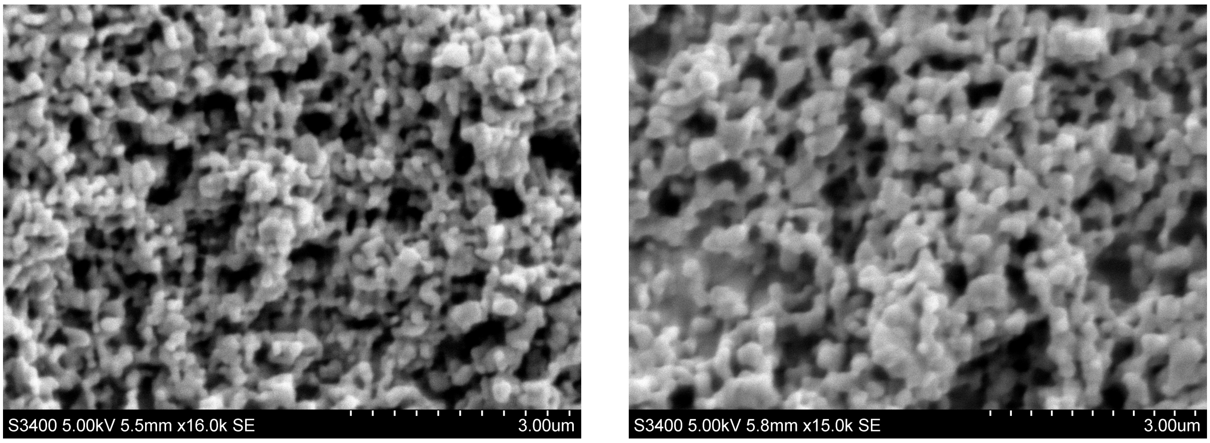
S3400 5.00kV 5.5mm x16.0k SE
3.00um
S3400 5.00kV 5.8mm x15.0k SE
3.00um

(a) Firing temperature 950 °C, 16000×

(b) Firing temperature 1000 °C, 15000×

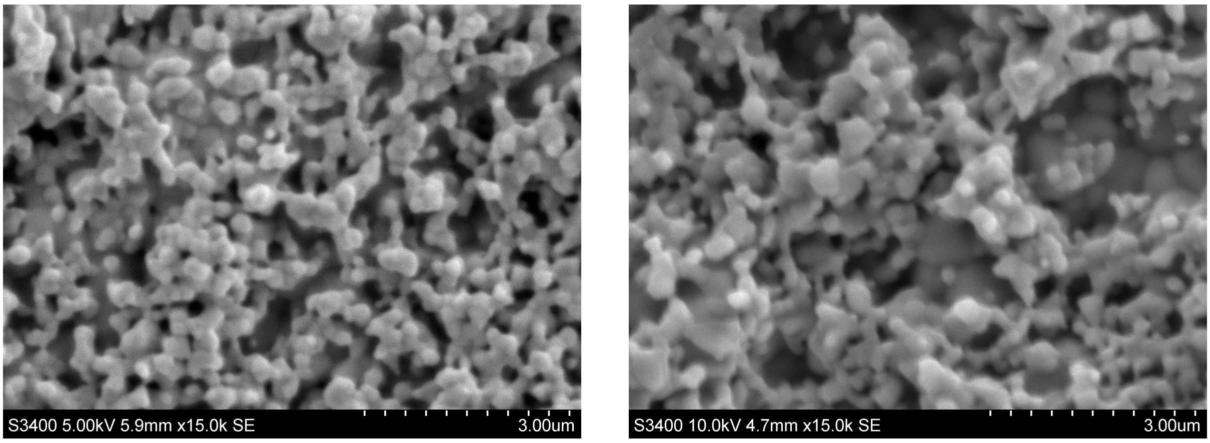
S3400 5.00kV 5.9mm x15.0k SE
3.00um
S3400 10.0kV 4.7mm x15.0k SE
3.00um

(c) Firing temperature 1050 °C, 15000×

(d) Firing temperature 1100 °C, 15000×

Figure 4.18: Higher magnification SEM images of the cathode surfaces of symmetric cells fired at 950 °C, 1000 °C, 1050 °C and 1100 °C, respectively.

Chapter 5

Discussion

5.1 Oxygen reduction kinetics

5.1.1 ASR and activation energy

Initial studies of the effect of firing time on the kinetics of oxygen reduction were carried out. A good compromise between ensuring sufficient adhesion of the cathode to the electrolyte and maintaining the specific surface area high was searched for. Naturally, the former improved with longer firing time, whereas the latter declined. Figure 4.9 clearly documents that the ASR after firing for 6 hours was more than twice as large as that after firing for 2 hours, meaning that 2 hours was used for all subsequent samples. This was also in accordance with the works of other researchers [25] [51]. However, it is very likely that this parameter can be optimized further by investigating even shorter firing times.

Once the firing time had been established, the effect of firing temperature was thoroughly investigated. The impedance response of symmetric cells fired at 950 °C, 1000 °C, 1050 °C and 1100 °C was measured at three different temperatures. By examination of the calculated ASRs for the various symmetric cells listed in Table 4.2, it is obvious that the ASR increased with increasing firing temperature. This was also in accordance with results reported elsewhere [51] [52]. Furthermore, the ASR was shown to decrease as the measurement temperature increased. Considering the thermally-activated nature of the oxygen reduction, this was as expected. This also serves to illustrate the challenge in obtaining IT-SOFCs. Lowering the measurement temperature from 800 °C to 600 °C increases the ASR by several orders of magnitude.

The observed effect of firing temperature is reasonable considering the temperature dependence of the specific surface area of LSCF. As documented by Table 4.1, the specific surface area was approximately 26 m^2/g after calcination at 725 °C, with a corresponding particle size below 20 nm. In contrast, the specific surface area of the powder from the pellet calcined at 900 °C was only about 1.7 m^2/g, with a corresponding particle size approaching 300 nm. It should be noted here that the reason for calcining the powder in the form of a pellet was to closer mimic the characteristics of the deposited cathode. Importantly, the specific surface area was observed to decline dramatically as the temperature was increased. Furthermore, the dilatometry data and sintering rate curve in Figure 4.4 shows that this effect is expected to become more prominent as the temperature is increased further from 950 °C through 1100 °C. As can be seen, shrinkage continues until temperatures around 1100 °C are reached, and the sintering rate reaches its maximum at approximately 1000 °C. Lastly, direct visual evidence for reduction in specific surface area can be seen from the SEM images in Figure 4.18. The cathode became denser as the temperature was increased, which entailed a reduction in the number of potential reaction sites for oxygen reduction. Consequently, the ASR increased. Chanquía et al. documented similar results by measuring the impedance of cathodes with different average crystallite sizes [5]. The ASRs were observed to be lowest for the smallest average crystallite size, which was explained by increased cathode surface area and shorter oxygen ion surface and/or bulk diffusion paths [5].

Based on the discussion above, it is obviously important to fire the cells at low temperatures. Not only will this improve the oxygen reduction kinetics, but the fabrication costs will also be minimized. This is important to take into account for large scale, commercial production. Even lower firing temperatures should therefore be investigated, and other researchers have documented that 850 °C is feasible [25] [51]. Furthermore, Darbandi et al. fired symmetric cells with LSCF cathodes at temperatures as low as 650 °C [53], albeit with a firing time of 10 hours. However, they identified the optimal firing temperature as 750 °C, and explained this by poor connectivity between individual cathode particles if lower temperatures were used. This indicates that the ideal firing temperature is a compromise between ensuring sufficient connectivity and maintaining a high specific surface area.

In order to assess the quality of the cathodes fabricated in the present work, obtained ASR values were compared to those reported by other researchers. Esquirol et al. fired symmetric cells consisting of LSCF cathodes and CGO electrolytes for 2 hours at 850 °C and 1000 °C [51]. Furthermore, the cathodes were comparable to those fabricated here as they were deposited by a spraying technique. By recording impedance data at 700 °C in pure oxygen for the cell fired at 850 °C, they found an ASR of 0.07 Ωcm^2. This is approximately one half of the ASR at 700 °C for the symmetric cell fired at 950 °C in the present work. The most likely reason for this difference is the firing temperature. Furthermore, the cathodes used by Esquirol et al. were homogeneous with thicknesses between 12-18 μm [51]. As evidenced by the SEM images in Figure 4.15, this stood in contrast to the cathodes fabricated here. The ASR is expected to decrease as the cathode becomes thicker, since there will be more reaction sites for oxygen reduction [52]. However, after a certain thickness is reached, this effect will be opposed by the longer diffusion paths to the electrolyte.

Dumaisnil et al. fabricated symmetric cells by screen printing $La_{0.6}Sr_{0.4}Co_{0.8}Fe_{0.2}O_3$ cathodes onto CGO electrolyte pellets [25]. Furthermore, the cells were fired at 850 °C for 2 hours, after which impedance data was recorded in air at different temperatures. The obtained ASRs at 600 °C and 700 °C were 0.38 Ωcm^2 and 0.15 Ωcm^2, respectively. In comparison, the ASR at 600 °C for the symmetric cell fired at 950 °C in the present work was higher by approximately 2 Ωcm^2. This discrepancy can possibly reflect the difference in firing temperatures used. However, the values are not directly comparable as the measurements were carried out in different atmospheres. Pure oxygen was used in the present work, whereas air was used by Dumaisnil et al. [25]. Other researchers have observed the appearance of an additional low-frequency arc above 700 °C for low oxygen partial pressures [51] [52], which could be attributed to gaseous diffusion [17] [51]. Importantly, the ASRs measured at 700 °C and 800 °C in the current work are thus expected to increase if air is used. Considering the relatively high ASRs reported, there seems to be room for improvement of the cathodes.

This is also supported by the observation that the calculated activation energies listed in Table 4.3 are higher than those reported in literature. The lowest activation energy obtained was 196.1 kJ/mol and corresponded to the symmetric cell fired at 1100 °C. Conversely, values in the range 120-150 kJ/mol are reported in the literature by various authors [26] [51] [52] [53]. Some have even documented activation energies as low as 100 kJ/mol [5]. It is likely that the higher values reported here can be ascribed, at least partially, to the poor cathode geometry documented by the SEM images in Figure 4.15 and 4.17. More homogeneous layers would probably give better performance. Surprisingly, it was also observed that the activation energy decreased continuously with increasing firing temperature. Judging by the reduction in specific surface area, an opposite trend was expected. This was shown by Esquirol et al., who documented higher activation energies for cathodes fired at 1000 °C than at 850 °C [51]. However, the pre-exponential factor in the Arrhenius equation must be taken into account. Figure 4.14 shows that the y-axis intercept, corresponding to the natural logarithm of the pre-exponential factor, vary significantly for the different least-square fitted data sets. Naturally, the activation energies calculated from the slopes will be influenced by this.

Valuable information about the oxygen reduction mechanism can be gained from calculated activation energies. Jiang reported an activation energy of 154 kJ/mol for symmetric cells with LSCF cathodes fired at 950 °C for 2 hours [26]. Interestingly, he observed that this value was approximately midway between the previously reported activation energy for oxygen surface exchange, 110 kJ/mol [54], and the oxygen self-diffusion coefficient, 200 kJ/mol [54]. Oxygen surface exchange at MIEC cathodes is a complex process that generally involves diffusion of gaseous oxygen to the gas/electrode interface, adsorption on the surface, dissociation into two oxygen atoms and finally incorporation of these as oxide ions in vacancies in the cathode material [12]. Conversely, the oxygen self-diffusion coefficient describes the bulk diffusion of oxygen in the absence of a chemical potential gradient [55]. The magnitude of the reported activation energy indicated that the oxygen reduction was in fact rate-limited by a combination of these processes, meaning that both surface and bulk properties must be taken into account for fabrication of cathodes [26]. Furthermore, the credibility of these results was improved by the comparable activation energies documented by Esquirol et al., who reported values of 133 kJ/mol and 149 kJ/mol for symmetric cells fired at 850 °C and 1000 °C, respectively [51].

The importance of bulk processes on the kinetics of oxygen reduction was evidenced by Darbandi et al. [53]. They reported an activation energy of 141.7 kJ/mol for pure LSCF cathodes, whereas 109.12 kJ/mol was reported for composite cathodes with 10 wt% CGO [53]. The latter value corresponded excellently to the value reported for oxygen surface exchange, and indicated that the contribution from bulk diffusion had been reduced by the enlarged TPB area and shorter diffusion paths to the electrolyte. Oxygen surface exchange was also found to be the dominating rate-determining electrode process in the work by Baumann et al. [12], who investigated microelectrodes of LSCF by impedance measurements in the same temperature region as used here. Justification for oxygen surface exchange as the rate-limiting process was found by comparing the thicknesses of their electrodes to the characteristic thickness, L_c. This is defined as $L_c = D^*/k^*$, where D^* is the oxygen tracer diffusion coefficient and k^* is the corresponding surface exchange rate constant [56]. Oxygen transport is predicted to be limited by bulk diffusion if the cathode thickness is larger than L_c, whereas surface exchange is expected to be limiting if the cathode thickness is smaller [12]. Furthermore, L_c is known to be on the order of 100 μm for MIECs in the $(La,Sr)(Co,Fe)O_{3-\delta}$ system [56] [57]. Based on this argument, the exceedingly thin cathodes in the present work suggest that surface exchange could be important.

However, the magnitudes of the calculated activation energies contradict this, and suggest that bulk diffusion of oxygen might be the main rate-limiting process. In particular, the values of 196.1 and 200.8 kJ/mol corresponding to firing at 1100 °C and 1050 °C, respectively, matched the reported activation energy of 200 kJ/mol [54] for oxygen self-diffusion nicely. On the other hand, the values obtained at lower temperatures were too high to be explained exclusively by this. This was surprising since the higher surface areas should ensure shorter oxygen diffusion paths, thereby reducing the contribution from bulk diffusion. One possible explanation could be an additional contribution from gaseous diffusion of oxygen in the cathodes with larger specific surface areas and smaller pore sizes.

It is also likely that the oxygen reduction is in fact rate-limited by multiple electrode processes. Evidence for this can be found by careful examination of the shape of the semi-circles in the Nyquist plots. In particular, the impedance response at 600 °C seems to be constituted of more than one semi-circle, implying that there is more than one rate-limiting electrode process. Considering the documented geometry of the cathode layers, this is reasonable. The width of the layers varies significantly, and it is conceivable that different rate-limiting electrode processes will dominate for different regions of the cathode. Bulk processes might control the oxygen reduction in regions with large cathode thickness, whereas surface processes dominate in the regions were the cathode is thin. In addition, contributions from electronic and ionic transfer at the cathode/interconnect and cathode/electrolyte interface, respectively, cannot be excluded. This reasoning should also apply to the measurements at 700 °C and 800 °C, since the cathode geometry is unchanged. However, the semi-circles in the corresponding Nyquist plots appear more regular in shape, and it is difficult based solely on the recorded impedance data to tell if this is indeed the case.

In order to reveal the nature of the electrode processes, the impedance response could be measured as a function of oxygen partial pressure since $\mathrm{ASR} \propto p_{\mathrm{O}_2}^{-n}$ [5] [51]. By plotting the natural logarithm of the ASR as a function of the natural logarithm of the oxygen partial pressure, the value of n can be obtained. Importantly, information about the rate-limiting step(s) can be deduced from this value: (i) $n = 1$ is often associated with steps involving molecular oxygen such as oxygen gas-phase diffusion or non-dissociative adsorption, (ii) $n \approx 0.5$ is attributed to dissociative adsorption or surface diffusion and (iii) $n = 0$ indicates steps such as oxide ion bulk diffusion in the cathode or transfer of oxide ions from cathode to electrolyte [5] [51].

5.1.2 Equivalent circuit

The equivalent circuit used to model the experimental data, shown in Figure 4.13, was based on the previous works by several other researchers [12] [25] [53] [58] [59]. It has been shown that circuits consisting of one resistor in series with resistors and constant phase elements in parallel account satisfactorily for the impedance response of symmetric cells with MIEC cathodes. In general, one RQ element should be added for each electrode process contributing to the observed impedance response. Some authors also include an inductance element at the very beginning of the circuit [53]. However, since the inductances arise from the apparatus itself and do not contribute with any valuable information about the oxygen reduction, it was argued that they could be removed prior to fitting. Consequently, the inductance element was omitted from the equivalent circuit used here.

Resistor R_1 in Figure 4.13 represents the ohmic resistance of the electrolyte and the lead wires [59], which can be seen at high frequencies in the non-normalized Nyquist plots shown in Appendix C. Furthermore, the magnitude in Ωcm^2 equals the distance along the x-axis from the origin to the intercept with the first semi-circle. As is obvious, especially for the data recorded at 700 °C and 800 °C, the magnitude varied significantly for the individual symmetric cells. One possible explanation for this is that the densities of the electrolyte pellets also varied. Another could be differences in the sample preparation and placement in the ProboStat™ for each individual sample. Furthermore, the electrolyte pellets were deliberately made quite thick to ease the manual handling of the cells. This naturally resulted in large ohmic resistances, as the oxide ions had to migrate a long distance. On the other hand, resistor R2 and constant phase element Q in Figure 4.13 represent the rate-limiting electrode process corresponding to the semi-circle observed at lower frequencies. As detailed above, this process(es) has not been unambiguously identified.

It is obviously important that the equivalent circuit correctly accounts for the electrode behavior, since the calculated ASR values in Table 4.2 are influenced by this. Therefore, the fit was qualitatively evaluated by comparing the model and experimental data visually for a representative selection of symmetric cells. Figure 5.1 and 5.2 show the correspondence for experimental data recorded at 600 °C and 700 °C, respectively, for the symmetric cell fired at 1000 °C. Figure 5.3 shows the correspondence for the data recorded at 800 °C for the symmetric cell fired at 1050 °C. The model is most well-suited for measurements at 700 °C. Apart from the highest frequencies, the model matches the experimental data reasonably well over the entire frequency range investigated. Conversely, the correspondence is not equally good for the data recorded at 600 °C. The discrepancy between the model and experimental data further supports the assumption that the oxygen reduction is in fact controlled by more than one electrode process at this temperature. Adding another RQ element to the circuit would probably improve the fit. Furthermore, the experimental data seem to flatten out for the lowest measured frequencies. It would be interesting to repeat the measurements and record data at even lower frequencies to reveal the nature of this. Contribution from diffusion processes are conceivable, and the addition of a Warburg element to the circuit might improve the match. Lastly, the model was observed to fit the data recorded at 800 °C poorly. The correspondence in the high-frequency region was particularly bad. Additionally, the model did not account for the observed flattening out at low frequencies. Nevertheless, it was concluded that the model was good enough to yield reliable ASR values for all measurement temperatures. This was confirmed by comparing the calculated values to those graphically extracted from the Nyquist plots. That being said, it will undoubtedly be beneficial to improve the model in future work, as this can help the interpretation of the physical processes controlling the oxygen reduction. By gaining such knowledge, targeted measures to improve the oxygen reduction kinetics can be implemented.

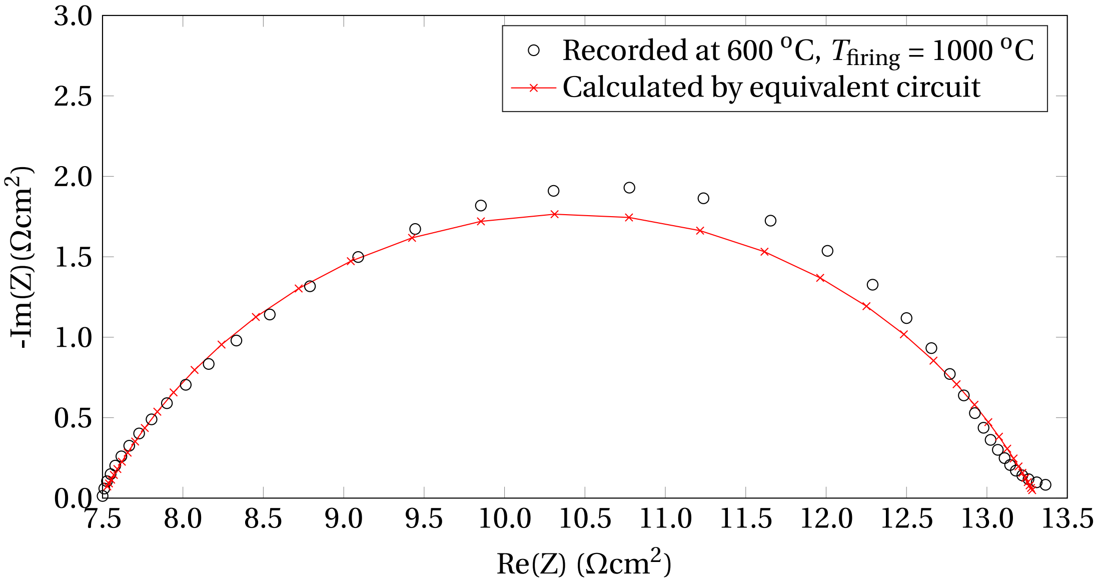

Figure 5.1: Correspondence of the model with impedance data recorded at 600 °C for the symmetric cell fired at 1000 °C.

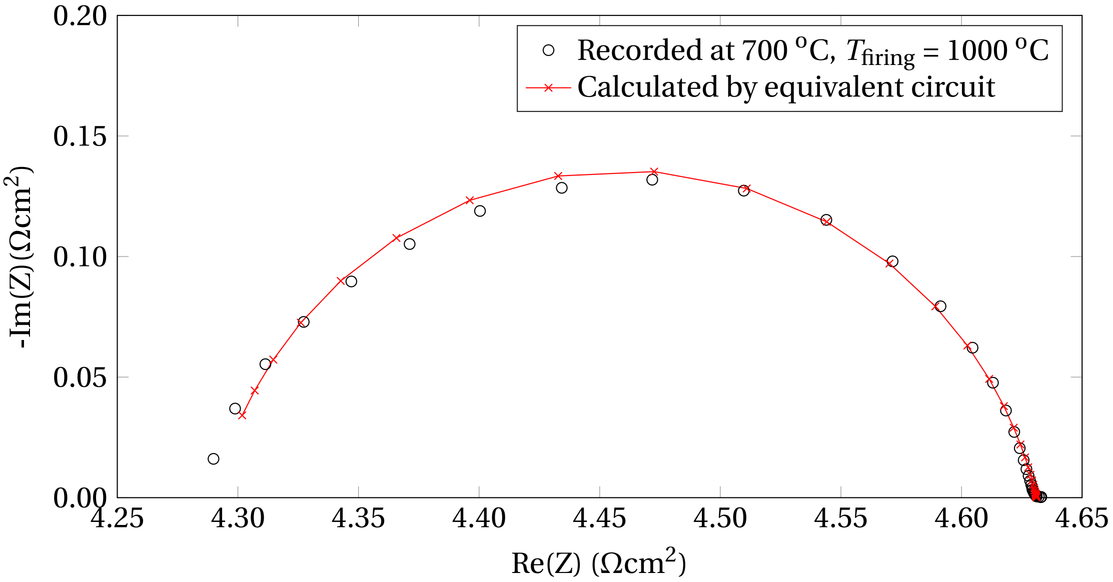

Figure 5.2: Correspondence of the model with impedance data recorded at 700 °C for the symmetric cell fired at 1000 °C.

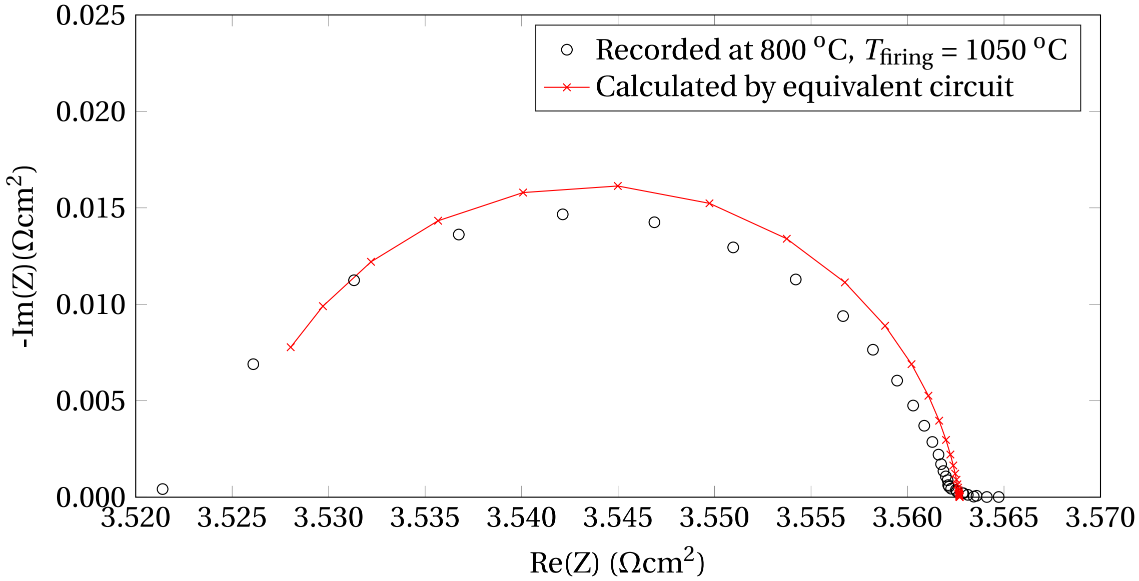

Figure 5.3: Correspondence of the model with impedance data recorded at 800 °C for the symmetric cell fired at 1050 °C.

5.2 Ceramic processing

5.2.1 Cathode deposition

As is evident from the SEM images of the cross sections in Figure 4.15 and the cathode surfaces in Figure 4.17, the deposited cathode layers were very inhomogeneous and agglomerates were present. The layers seemed to be around 10 μm wide at their maximum, whereas the width was only a couple microns in other areas. This poor geometry was undoubtedly a result of the deposition method used. Being non-automated, air brushing introduces numerous parameters that are impossible to control precisely. Hence, it is exceedingly difficult to evaluate the contribution of each one on the characteristics of the final cathode. In future work, effort should be made to improve the reproducibility. Other techniques for cathode deposition could also be considered. There exist many examples in the literature of symmetric cells fabricated by screen printing [25] [60] [61] [62]. Vaßen et al. reported that screen printed cathodes showed superior performance compared to cathodes made by atmospheric plasma spraying [63].

The LSCF dispersion is arguably very important for the quality of the deposited cathodes. A new batch was made for each set of symmetric cells, and complete consistency could therefore not be guaranteed. Furthermore, the dispersions were observed to be highly unstable, which could to a large extent be explained by the very small particle size. Sedimentation due to gravitational forces initiated almost immediately after the dispersions were put down. To limit the effect of this, the dispersion was applied very quickly after being transferred to the airbrush. However, this seems to have been ineffective based on the recorded SEM images. The addition of a suitable dispersing agent could probably help diminish this challenge. The ζ-potential of LSCF has been plotted as a function of pH in the article by Fernández-González et al. [64]. They reported that the isoelectric point for a suspension of LSCF prepared in a 10^{-2} M KCl solution occurred for a pH-value of approximately 6. Furthermore, they reported that stable dispersions could be achieved for pH<3 and pH>7, meaning that both acidic and alkaline dispersing agents could be used. One possible candidate could be polyvinylpirrolidone, as used by Chanquía et al. in the preparation of LSCF inks [5]. However, it is important that the dispersing agent is organic to ensure that it burns off during the subsequent firing of the symmetric cells. Moreover, the required amount of dispersing agent would have to be determined. Small amounts are usually required, and a good starting point could be 1 wt% of the LSCF powder. Another possible way to diminish the challenge of sedimentation is simply to make dispersions with less LSCF content, e.g. 1 wt% as opposed to 2 wt%.

Furthermore, parameters such as the distance between the airbrush and pellets and the angle at which the spray hit the pellets varied since the device is handheld. Mounting the airbrush to a stand to maintain a constant position would partially solve this problem. However, the variation would not be completely removed as the position of the pellets also affects these parameters. Moreover, the duration of each spraying should be kept constant. In the current work, the need for applying the dispersion very quickly made this difficult. Ideally, the process should be standardized with fixed values for the spraying duration and number of layers applied. This would help improve the reproducibility by ensuring that the amount of deposited cathode is relatively constant for each symmetric cell fabricated. The weight of the applied cathode was measured here in an attempt to ensure some consistency, and the values obtained ranged from 0.003 g to 0.004 g. Larger values should be pursued in future work considering that the cathodes fabricated seemed too thin to give optimal performance.

5.2.2 Phase purity of LSCF

In previous work, an ideal calcination temperature for the as-received LSCF powder had been searched for. The secondary phases observed in the powder synthesized by CerPoTech AS (Trondheim, Norway) had to be removed. Simultaneously, it was desired to limit coarsening as much as possible to obtain cathodes with favorable characteristics later. Thus, the lowest calcination temperature to yield a phase pure powder, identified as 725 °C, was viewed as the optimal compromise between these two opposing considerations. This was supported by the high specific surface area of LSCF measured afterwards in the current work. The value of approximately 26 m^2/g was higher than that reported by Chanquía et al. for a comparable calcination procedure [5], whereas Darbandi et al. documented even better results [53]. It might be possible to increase the specific surface area by lowering the calcination temperature further. Currently, temperatures between 700 °C and 725 °C have not been investigated, meaning that a phase pure powder could potentially be obtained in this interval. This might be important as a small reduction in calcination temperature could result in a substantial increase in the specific surface area.

Even though the as-calcined powder was phase pure, one or more secondary phases evidenced by reflections at $2\theta \approx 25°$ and $2\theta \approx 36°$ was observed after ball milling. This was unexpected, and the result had to be verified by repeating the calcination and ball milling for another batch. Once again, the two reflections were clearly visible. Interestingly, one of the secondary phases initially observed in the as-synthesized powder had also been observed at $2\theta \approx 25°$. Furthermore, this had been identified as $SrCO_3$ based on correspondence with the pattern given in PDF 00-005-0418 and the results of other authors [53]. However, it is not obvious that the reflection observed after ball milling can be explained by reintroduction of $SrCO_3$, even though it occurs for the same 2θ. Moreover, it has not been established whether the reflection at $2\theta \approx 36°$ belongs to the same secondary phase or another one. A thorough investigation of the nature and origin of the secondary phase(s) is warranted in future work, as the cathode performance can be affected adversely by the presence of these. In this context, the effect of the milling fluid could be investigated by replacing ethanol with acetone [51] or isopropanol [5]. However, renewed calcination at 725 °C for 6 hours after ball milling was observed to give a phase pure powder once more. The secondary phase(s) were therefore expected to disappear during firing of the symmetric cells, and no further time was spent on this in the present work.

5.2.3 CGO electrolyte pellets

Before satisfactory symmetric cells could be obtained, a procedure for fabrication of dense CGO electrolyte pellets had to be developed. As can be seen from the SEM images in Figure 4.6, spherical agglomerates with eggshell-like morphology were observed in the as-received powder. The presence of such agglomerates were unacceptable as they would make fabrication of dense pellets impossible, meaning that ball milling was necessary to break these down. The applied milling procedure seemed to be effective, as the primary particle size afterwards appeared to be 100 nm or less. Furthermore, suitable parameters for the uniaxial pressing and subsequent sintering had to be determined. The initial parameter values were based on the work previously done by Øygarden [6]. He reported that dense pellets with diameters of 20 mm could be fabricated by uniaxial pressing with an applied pressure of 30 MPa followed by sintering for 2 hours at 1250 °C. However, when this was attempted in the present work, the results were less than satisfactory. The applied pressure was therefore increased to 60 MPa, which yielded pellets with maximum relative densities of 92%. Although better than before, this was still not sufficient. Hence, the pressure was increased further to 80 MPa. The resulting densities were now consistently higher than 93%, with some pellets displaying densities as high as 96-97%. However, the pellets showed signs of pressing defects and several of them cracked during grinding before cathode deposition. Finally, the pressure was reduced to 70 MPa. Densities in the range 94-97% were measured, and the pellets seemed defect free. Furthermore, the pellets were sintered at 1300 °C. Figure 4.7 shows that densification of CGO initiates at around 600 °C. This temperature was surprisingly low considering that undoped ceria has a melting point of 2600 °C [65], implying that CGO has very good sintering properties.

After sintering, the CGO pellets were grinded to ensure good adhesion to the deposited cathode. However, the need for this processing step can be questioned based on the work by other researchers. It was omitted by both by Esquirol et al. and Marrero-López et al. without any observable detrimental effect on the cathode adhesion [51] [52]. This indicates that the the grinding step can be removed altogether. Reduction in the amount of required processing would save both time and money, thus being very important for large scale production.

5.3 Further work

In order to improve the credibility of the documented results, more symmetric cells should be fabricated and characterized. Since the collected data thus far is quite limited, coincidences and erroneous measurements could possibly affect the results significantly. That being said, the documented temperature dependence of the ASR is reasonable, and there is no evidence that indicates this to be incorrect.

In addition to confirming already existing results, the effect of firing temperature should be investigated further. Other researchers have shown that firing temperatures below 950 °C are feasible and improve the oxygen reduction kinetics. Based on the dilatometry data, further reduction of the firing temperature seems to be possible here as well. Moreover, it would also be interesting to document the effect of firing time more thoroughly, since it definitely influences the oxygen reduction kinetics significantly. It should be kept as short as possible to avoid excessive densification of the electrode, and it seems likely that shorter times than 2 hours could still yield sufficient adhesion of the cathode to the electrolyte. Both the effect of reduced firing temperature and reduced firing time could be quantitatively evaluated by accounting more accurately for the temperature dependence of the specific surface area. In the current work, it was established that an increase in temperature resulted in a substantial reduction of the specific surface area. However, the exact nature of this dependence was not revealed.

Furthermore, the effect of atmosphere should be looked into. By measuring the impedance for various oxygen partial pressures, valuable information about the mechanism of oxygen reduction can be deduced. Equally important is the fact that pure oxygen is not realistic with regard to real life applications. It is obviously essential to document the cathode performance under realistic operating conditions. In this context, it should also be mentioned that ASR values for symmetric cells are not necessarily identical to those obtained for actual fuel cells, i.e. when an anode is also included. The reason for this is that there exists a gradient in oxygen chemical potential, as shown in Figure 2.12, and that the current across the cell actually affects the electrode polarizations [5]. Naturally, it will eventually become necessary to test the cathodes in a complete fuel cell setup to assess their actual performance.

Chapter 6

Conclusion

The effect of firing temperature on the kinetics of oxygen reduction in LSCF cathodes was investigated by electrochemical impedance spectroscopy in pure oxygen at three measurement temperatures. As documented by recorded data of symmetric cells fired at 950 °C, 1000 °C, 1050 °C and 1100 °C, the ASR increased continuously with increasing firing temperature. Various characterization methods evidenced that this could be ascribed to the simultaneous reduction in specific surface area. Importantly, it was thus concluded that the firing temperature should be kept low to obtain fast oxygen reduction kinetics. Furthermore, activation energies for all firing temperatures were calculated from Arrhenius plots. Information about the mechanism of oxygen reduction was extracted from these, and it appeared that the oxygen reduction was controlled by multiple electrode processes. Moreover, the ASRs and activation energies obtained in the present work were observed to be higher than values reported in the literature. This was explained by the poor cathode geometry resulting from the deposition method used. Recorded SEM images showed that the deposited cathodes were inhomogeneous and that large agglomerates were present. However, considering that only minimal effort has been made to optimize the fabrication procedure thus far, the results are promising for the use of spray-pyrolyzed LSCF as cathode material for IT-SOFCs.

References

[1] IPCC, 2014: Climate Change 2014: Synthesis Report. Contribution of Working Groups I, II and III to the Fifth Assessment Report of the Intergovernmental Panel on Climate Change [Core Writing Team, R.K. Pachauri and L.A. Meyer (eds.)]. Technical report, IPCC, Geneva, Switzerland, 151 pp.

[2] A.J. Moulson and J.M. Herbert. *Electroceramics.* Wiley, second edition, 2003.

[3] Kevin Huang and Subhash C. Singhal. Cathode-supported tubular solid oxide fuel cell technology: A critical review. *Journal of Power Sources*, 237:84–97, September 2013.

[4] Nagore Ortiz Vitoriano. *Novel* $Ln_{1-x}Ca_xFe_{0.8}Ni_{0.2}O_3$ *(Ln = La, Pr; 0<x<1) phases with perovskite type structure as cathode materials for solid oxide fuel cells.* PhD thesis, University of the Basque Country, 2011.

[5] Corina M. Chanquia, Liliana Mogni, Horacio E. Troiani, and Alberto Caneiro. Highly active $La_{0.4}Sr_{0.6}Co_{0.8}Fe_{0.2}O_{3-\delta}$ nanocatalyst for oxygen reduction in intermediate temperature-solid oxide fuel cells. *Journal of Power Sources*, 270:457–467, December 2014.

[6] Vegar Øygarden. *4d/5d Transition Metals in Perovskite Cathode Materials.* PhD thesis, Norwegian University of Science and Technology, 2013.

[7] Sune Dalgaard Ebbesen, Søren Højgaard Jensen, Anne Hauch, and Mogens Bjerg Mogensen. High Temperature Electrolysis in Alkaline Cells, Solid Proton Conducting Cells, and Solid Oxide Cells. *Chemical Reviews*, 114(21):10697–10734, 2014.

[8] N. Q. Minh. CERAMIC FUEL-CELLS. *Journal of the American Ceramic Society*, 76(3):563–588, 1993.

[9] A. J. Jacobson. Materials for Solid Oxide Fuel Cells. *Chemistry of Materials*, 22(3):660–674, 2010.

[10] S. Singhal. Advances in solid oxide fuel cell technology. *Solid State Ionics*, 135(1-4):305–313, November 2000.

[11] Osamu Yamamoto. Solid oxide fuel cells: fundamental aspects and prospects. *Electrochimica Acta*, 45(15-16):2423–2435, May 2000.

[12] F. Baumann, J. Fleig, H. Habermeier, and J. Maier. Impedance spectroscopic study on well-defined (La,Sr)(Co,Fe)$O_{3-\delta}$ model electrodes. *Solid State Ionics*, 177(11-12):1071–1081, April 2006.

[13] A. Mai, V. Haanappel, S. Uhlenbruck, F. Tietz, and D. Stover. Ferrite-based perovskites as cathode materials for anode-supported solid oxide fuel cells. Part I. Variation of composition. *Solid State Ionics*, 176(15-16):1341–1350, May 2005.

[14] Jürgen Fleig. Solid Oxide Fuel Cell Cathodes: Polarization Mechanisms and Modeling of the Electrochemical Performance. *Annual Review of Materials Research*, 33(1):361–382, August 2003.

[15] Stephen J. Skinner. Recent advances in Perovskite-type materials for solid oxide fuel cell cathodes. *International Journal of Inorganic Materials*, 3(2):113–121, March 2001.

[16] Sossina M. Haile. Fuel cell materials and components. *Acta Materialia*, 51(19):5981–6000, November 2003.

[17] S. B. Adler. Factors governing oxygen reduction in solid oxide fuel cell cathodes. *Chemical Reviews*, 104(10):4791–4843, 2004.

[18] G. Muller, A. Ringuede, and C. Laberty-Robert. Synthesis, characterization and electrical properties of $La_{0.7}Sr_{0.3}Co_{0.2}Fe_{0.8}O_3$/Gd-$CeO_2$ thin films (≤ 500 nm). *Journal of Materials Chemistry A*, 2(18):6448–6455, 2014.

[19] M. J. Verkerk, M. W. J. Hammink, and A. J. Burggraaf. Oxygen Transfer on Substituted ZrO_2, Bi_2O_3 and CeO_2 Electrolytes with Platinum Electrodes. 1. Electrode Resistance by D-C Polarization. *Journal of the Electrochemical Society*, 6691(January):70–78, 1983.

[20] Anthony R. West. *Basic Solid State Chemistry*. Wiley, second edition, 1999.

[21] K. Momma and F. Izumi. Vesta: a three dimensional visualization system for electronic and structural analysis. *Journal of Applied Crystallography*, 41:653–658, 2008.

[22] Konrad Świerczek and Makoto Gozu. Structural and electrical properties of selected $La_{1-x}Sr_xCo_{0.2}Fe_{0.8}O_3$ and $La_{0.6}Sr_{0.4}Co_{0.2}Fe_{0.6}Ni_{0.2}O_3$ perovskite type oxides. *Journal of Power Sources*, 173:695–699, 2007.

[23] L.-W. Tai, M.M. Nasrallah, H. U. Anderson, D. M. Sparlin, and S. R. Sehlin. Structure and electrical properties of $La_{1-x}Sr_xCo_yFe_{1-y}O_3$. Part 2. The system $La_{1-x}Sr_xCo_{0.2}Fe_{0.8}O_3$. *Solid State Ionics*, 76(3-4):273–283, 1995.

[24] L. W. Tai, M. M. Nasrallah, H. U. Anderson, D. M. Sparlin, and S. R. Sehlin. Structure and Electrical-Properties of $La_{1-x}Sr_xCo_{1-y}Fe_yO_3$. Part 1. The System $La_{0.8}Sr_{0.2}Co_{1-y}Fe_yO_3$. *Solid State Ionics*, 76(94):259–271, 1995.

[25] K. Dumaisnil, D. Fasquelle, M. Mascot, A. Rolle, P. Roussel, S. Minaud, B. Duponchel, R. N. Vannier, and J. C. Carru. Synthesis and characterization of $La_{0.6}Sr_{0.4}Co_{0.8}Fe_{0.2}O_3$ films for solid oxide fuel cell cathodes. *Thin Solid Films*, 553:89–92, 2014.

[26] S. P. Jiang. A comparison of O_2 reduction reactions on porous (La,Sr)MnO_3 and (La,Sr)(Co,Fe)O_3 electrodes. *Solid State Ionics*, 146:1–22, 2002.

[27] S. Wang. High temperature properties of $La_{0.6}Sr_{0.4}Co_{0.8}Fe_{0.2}O_{3-\delta}$ phase structure and electrical conductivity. *Solid State Ionics*, 159:71–78, 2003.

[28] J. A. Lane, S. J. Benson, D. Waller, and J. A. Kilner. Oxygen transport in $La_{0.6}Sr_{0.4}Co_{0.2}Fe_{0.8}O_{3-\delta}$. *Solid State Ionics*, 121:201–208, 1999.

[29] M. J. Verkerk and A. J. Burggraaf. Oxygen Transfer on Substituted ZrO_2, Bi_2O_3, and CeO_2 Electrolytes with Platinum Electrodes. 2. A-C Impedance Study. *Journal of the Electrochemical Society*, 354(January):78–84, 1983.

[30] J. Mizusaki, K. Amano, S. Yamauchi, and K. Fueki. Electrode Reaction at Pt, O_2(g)/Stabilized Zirconia Interfaces. Part I: Theoretical Consideration of Reaction Model. *Solid State Ionics*, 22(4):313–322, 1987.

[31] J. Mizusaki, K. Amano, S. Yamauchi, and K. Fueki. Electrode Reaction at Pt, O_2(g)/Stabilized Zirconia Interfaces. Part II: Electrochemical Measurements and Analysis. *Solid State Ionics*, 22(4):323–330, 1987.

[32] N. L. Robertson and J. N. Michaels. Oxygen exchange on platinum electrodes in zirconia cells: location of electrochemical reaction sites. *Journal of the Electrochemical Society*, 137(1), 1990.

[33] O. Yamamoto, Y. Takeda, R. Kanno, and M. Noda. Perovskite-Type Oxides as Oxygen Electrodes for High Temperature Oxide Fuel Cells. *Solid State Ionics*, (February):1–6, 1987.

[34] J.E. Bauerle. Study of Solid Electrolyte Polarization by a Complex Admittance Method. *Journal of Physics and Chemistry of Solids*, 30(12):2657–2670, 1969.

[35] E. Barsoukov and J. R. Macdonald. *Impedance Spectroscopy. Theory, Experiment, and Applications*. Wiley, second edition, 2005.

[36] C. H. Hamann, A. Hamnett, and W. Vielstich. *Electrochemistry*. Wiley-VCH, second edition, 2007.

[37] A. M. Svensson, S. Sunde, and K. Nisancioglu. Mathematical Modeling of Oxygen Exchange and Transport in Air-Perovskite-Yttria-Stabilized Zirconia Interface Regions. *Journal of The Electrochemical Society*, 145(4):1390, 1998.

[38] S. B. Adler, J. A. Lane, and B. C. H. Steele. Electrode Kinetics of Porous Mixed-Conducting Oxygen Electrodes. *Journal of The Electrochemical Society*, 143(11):3554, 1996.

[39] S. B. Adler. Mechanism and kinetics of oxygen reduction on porous $La_{1-x}Sr_xCoO_{3-\delta}$ electrodes. *Solid State Ionics*, 111:125–134, 1998.

[40] J. Fleig and J. Maier. The polarization of mixed conducting SOFC cathodes: Effects of surface reaction coefficient, ionic conductivity and geometry. *Journal of the European Ceramic Society*, 24(6):1343–1347, January 2004.

[41] Matthew M. Mench. *Fuel Cell Engines*. Wiley, 2008.

[42] Miklos Lengyel, Dror Elhassid, Gal Atlas, William T. Moller, and Richard L. Axelbaum. Development of a scalable spray pyrolysis process for the production of non-hollow battery materials. *Journal of Power Sources*, 266:175–178, 2014.

[43] Sanjeev Jain, Daniel J. Skamser, and Toivo T. Kodas. Morphology of Single-Component Particles Produced by Spray Pyrolysis. *Aerosol Science and Technology*, 27(April 2015):575–590, 1997.

[44] Marián Palcut, Ruth Knibbe, Kjell Wiik, and Tor Grande. Cation inter-diffusion between $LaMnO_3$ and $LaCoO_3$ materials. *Solid State Ionics*, 202(1):6–13, November 2011.

[45] Marián Palcut, Jens S Christensen, Kjell Wiik, and Tor Grande. Impurity diffusion of ^{141}Pr in $LaMnO_3$, $LaCoO_3$ and $LaFeO_3$ materials. *Physical chemistry chemical physics : PCCP*, 10(43):6544–52, November 2008.

[46] S.B. Weber, H.L. Lein, T. Grande, and M.-A. Einarsrud. Influence of the precursor solution chemistry on the deposition of thick coatings by spray pyrolysis. *Surface and Coatings Technology*, 221:53–58, April 2013.

[47] T. Mokkelbost, Ø. Andersen, R. A. Strøm, K. Wiik, T. Grande, and M. A. Einarsrud. High-Temperature Proton-Conducting $LaNbO_4$-Based Materials: Powder Synthesis by Spray Pyrolysis. *Journal of the American Ceramic Society*, 90(11):3395–3400, 2007.

[48] CerPoTech. Accessed 13.05.2015. `http://cerpotech.com/spraypyrolysis`.

[49] Ningbo Tagore Machinery Co. Ltd. Accessed 26.05.2015. `http://www.tagoreairbrush.com/news/Gravity-Feed-Airbrush-Diagram-55.html`.

[50] S. Brunauer, P. H. Emmett, and E. Teller. Adsorption of Gases in Multimolecular Layers. *Journal of the American Chemical Society*, 60(2):309–319, 1938.

[51] A. Esquirol, N. P. Brandon, J. A. Kilner, and M. Mogensen. Electrochemical Characterization of $La_{0.6}Sr_{0.4}Co_{0.2}Fe_{0.8}O_3$ Cathodes for Intermediate-Temperature SOFCs. *Journal of The Electrochemical Society*, 151(11):A1847–A1855, 2004.

[52] D. Marrero-López, R. Romero, F. Martín, and J. R. Ramos-Barrado. Effect of the deposition temperature on the electrochemical properties of $La_{0.6}Sr_{0.4}Co_{0.8}Fe_{0.2}O_{3-\delta}$ cathode prepared by conventional spray-pyrolysis. *Journal of Power Sources*, 255:308–317, 2014.

[53] Azad J. Darbandi and Horst Hahn. Nanoparticulate cathode thin films with high electrochemical activity for low temperature SOFC applications. *Solid State Ionics*, 180(26-27):1379–1387, 2009.

[54] B. C. H. Steele and J.-M. Bae. Properties of $La_{0.6}Sr_{0.4}Co_{0.2}Fe_{0.8}O_{3-x}$ (LSCF) double layer cathodes on gadolinium-doped cerium oxide (CGO) electrolytes: II. Role of oxygen exchange and diffusion. *Solid State Ionics*, 106(3-4):255–261, 1998.

[55] Richard J.D. Tilley. *Understanding Solids*. Wiley, 2nd edition, 2013.

[56] B. C. H. Steele. Interfacial reactions associated with ceramic ion transport membranes. *Solid State Ionics*, 75:157–165, 1995.

[57] H. J. M. Bouwmeester, H. Kruidhof, and A. J. Burggraaf. Importance of the surface exchange kinetics as rate limiting step in oxygen permeation through mixed-conducting oxides. *Solid State Ionics*, 72:185–194, 1994.

[58] Jae Dong Kim, Goo Dae Kim, Ji Woong Moon, Yong Il Park, Weon Hae Lee, Koichi Kobayashi, Masayuki Nagai, and Chang Eun Kim. Characterization of LSM-YSZ composite electrode by ac impedance spectroscopy. *Solid State Ionics*, 143(3-4):379–389, 2001.

[59] Xingyan Xu, Zhiyi Jiang, Xing Fan, and Changrong Xia. LSM-SDC electrodes fabricated with an ion-impregnating process for SOFCs with doped ceria electrolytes. *Solid State Ionics*, 177(19-25):2113–2117, 2006.

[60] Laurenia M. P. Garcia, Daniel A. Macedo, Graziele L. Souza, Fabiana V. Motta, Carlos A. Paskocimas, and Rubens M. Nascimento. Citrate-hydrothermal synthesis, structure and electrochemical performance of $La_{0.6}Sr_{0.4}Co_{0.2}Fe_{0.8}O_{3-\delta}$ cathodes for IT-SOFCs. *Ceramics International*, 39(7):8385–8392, 2013.

[61] J. Dailly, F. Mauvy, M. Marrony, M. Pouchard, and J. C. Grenier. Electrochemical properties of perovskite and A_2MO_4-type oxides used as cathodes in protonic ceramic half cells. *Journal of Solid State Electrochemistry*, 15(2):245–251, 2011.

[62] Jimmi Nielsen, Per Hjalmarsson, Martin Hangaard Hansen, and Peter Blennow. Effect of low temperature in-situ sintering on the impedance and the performance of intermediate temperature solid oxide fuel cell cathodes. *Journal of Power Sources*, 245:418–428, 2014.

[63] R. Vaßen, D. Hathiramani, J. Mertens, V. A. C. Haanappel, and I. C. Vinke. Manufacturing of high performance solid oxide fuel cells (SOFCs) with atmospheric plasma spraying (APS). *Surface and Coatings Technology*, 202(3):499–508, 2007.

[64] R. Fernández-González, T. Molina, S. Savvin, R. Moreno, A. Makradi, and P. Núñez. Characterization and fabrication of LSCF tapes. *Journal of the European Ceramic Society*, 34:953–959, 2014.

[65] G. Aylward and T. Findlay. *SI Chemical Data*. Wiley, 6th edition, 2008.

Appendix A

BET surface area plots

The recorded BET surface area plots are presented in this appendix. Figure A.1 and A.2 shows the surface area plot for sample 1 and sample 2 calcined at 725 °C, respectively. Figure A.3 and A.4 shows the surface area plot for sample 1 and sample 2 calcined at 900 °C, respectively. The y-axis intercepts were obtained by least-square fitting and extrapolation of the experimental data.

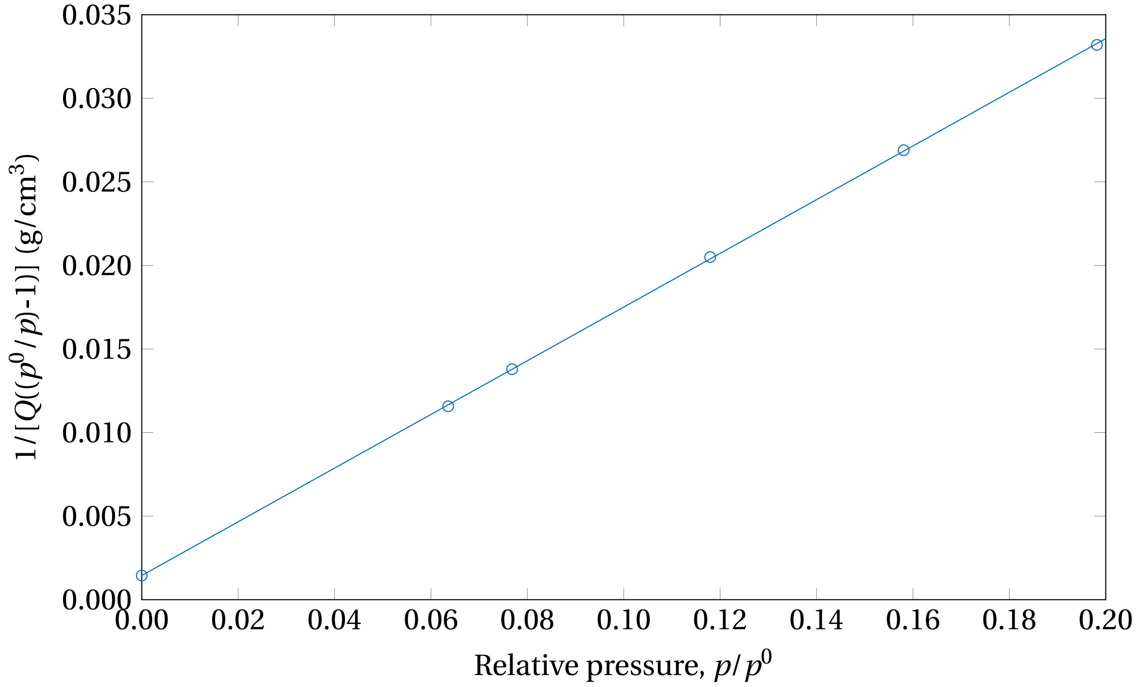

Figure A.1: BET surface area plot for sample 1 calcined at 725 °C.

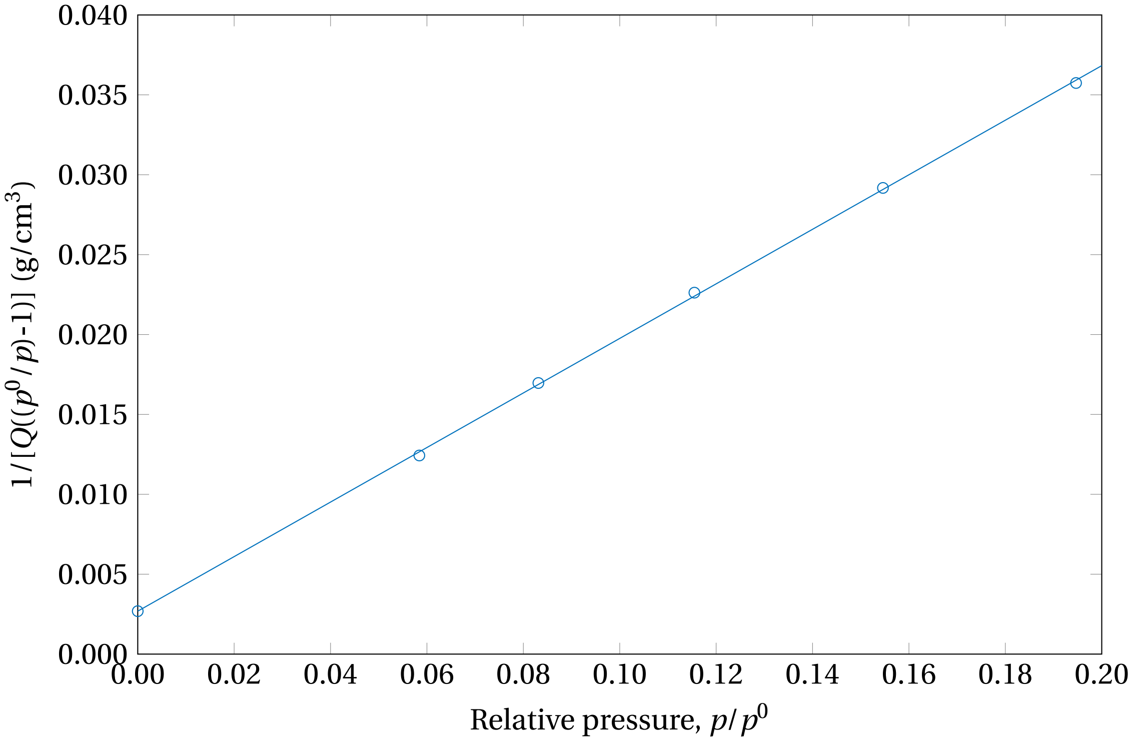

Figure A.2: BET surface area plot for sample 2 calcined at 725 °C.

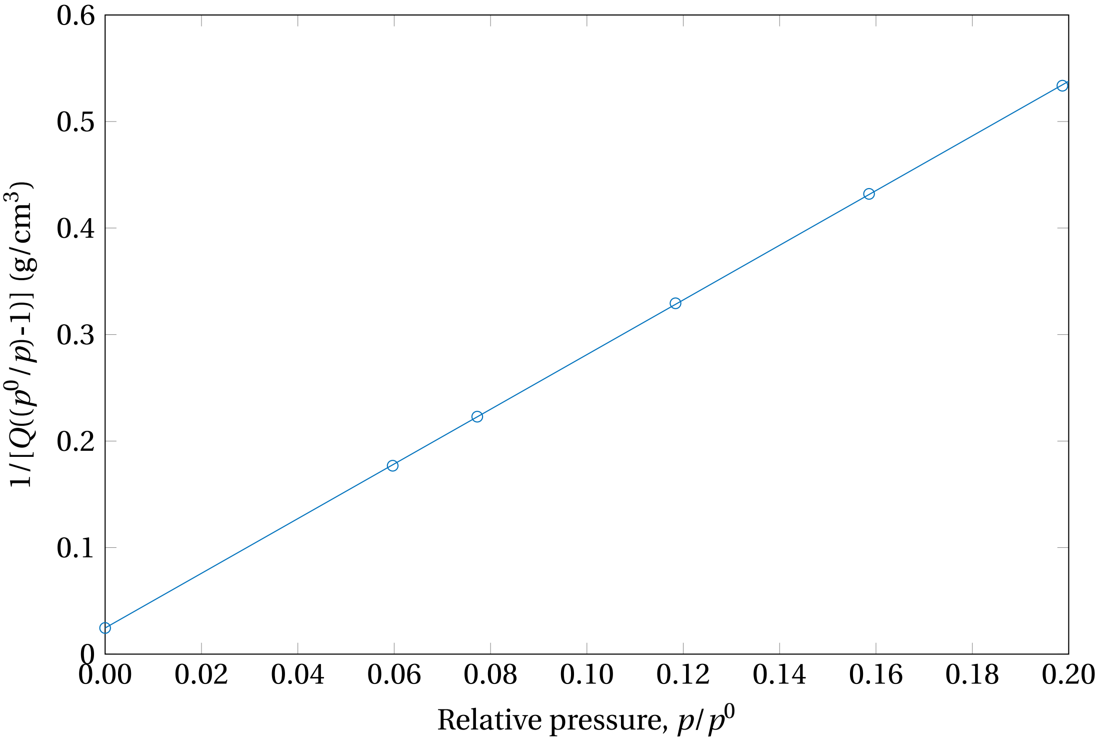

Figure A.3: BET surface area plot for sample 1 calcined at 900 °C.

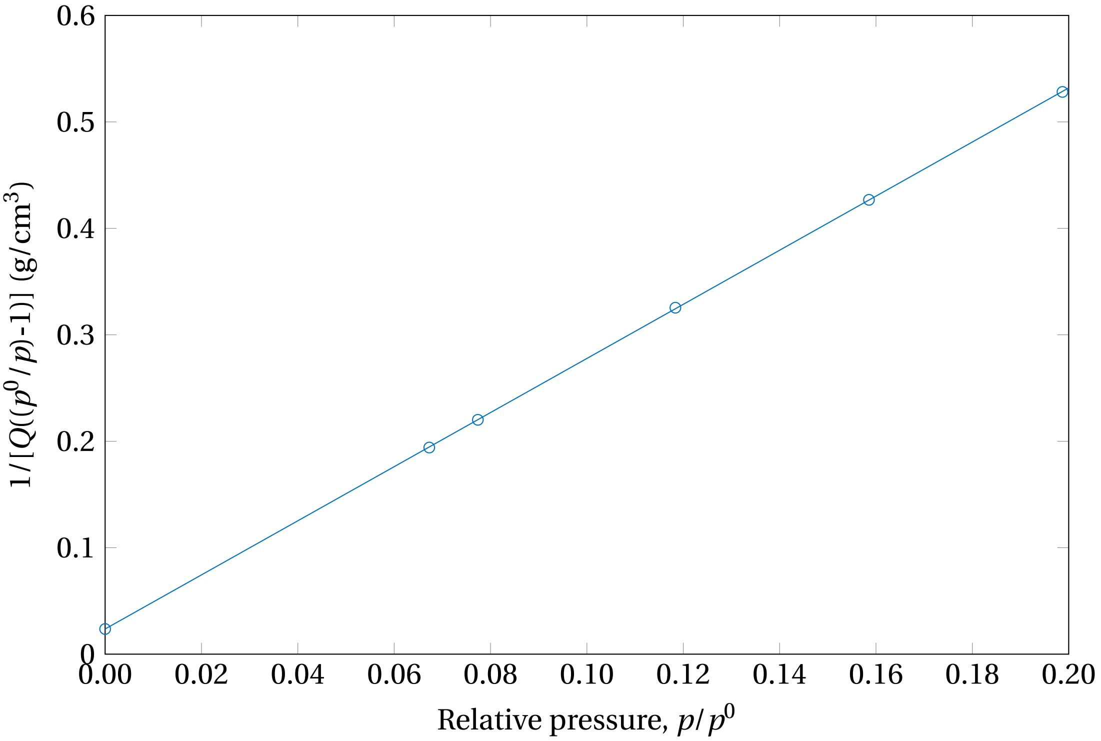

Figure A.4: BET surface area plot for sample 2 calcined at 900 °C.

Appendix B

Calculation of LSCF particle sizes

In this appendix, the procedure for calculation of LSCF particle sizes from specific surface areas is shown. The surface area and volume of one particle can be expressed as $A = 4\pi r^2$ and $V = \frac{4}{3}\pi r^3$, respectively, if spherical particles with radius r is assumed. Then, the mass of the particle can be found by multiplying the crystallographic density of LSCF, given in PDF 04-017-2448, with V. Furthermore, the measured specific surface area can be expressed as:

$$A_{\text{spec}} = \frac{A}{\rho V} = \frac{4\pi r^2}{\rho \frac{4}{3}\pi r^3} = \frac{3}{\rho r} \tag{B.1}$$

where ρ is the crystallographic density. Finally, the particle size as given by the radius can be calculated:

$$r = \frac{3}{\rho A_{\text{spec}}} \tag{B.2}$$

Appendix C

Non-normalized Nyquist plots

This appendix shows the non-normalized Nyquist plots of the electrochemical impedance data recorded to investigate the effect of firing time and firing temperature. Figure C.1 shows the data recorded at 700 °C for the symmetric cells fired at 2 hours and 6 hours, respectively. The data recorded at 600 °C, 700 °C and 800 °C for symmetric cells fired at 950 °C, 1000 °C, 1050 °C and 1100 °C are presented in Figure C.2, C.3 and C.4, respectively.

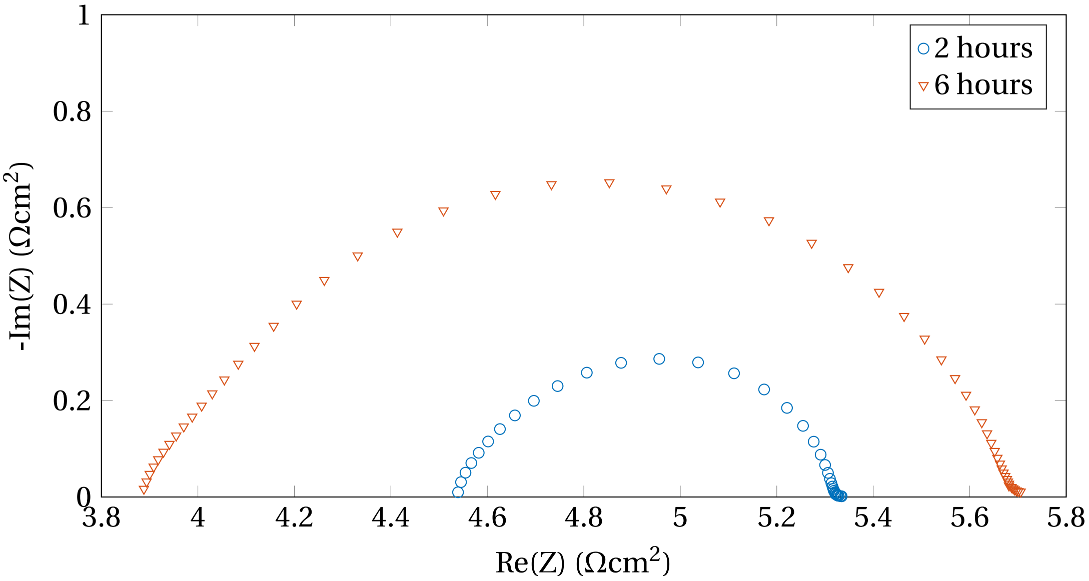

Figure C.1: Electrochemical impedance data recorded at 700 °C in pure oxygen for symmetric cells fired at 1100 °C for 2 hours and 6 hours, respectively.

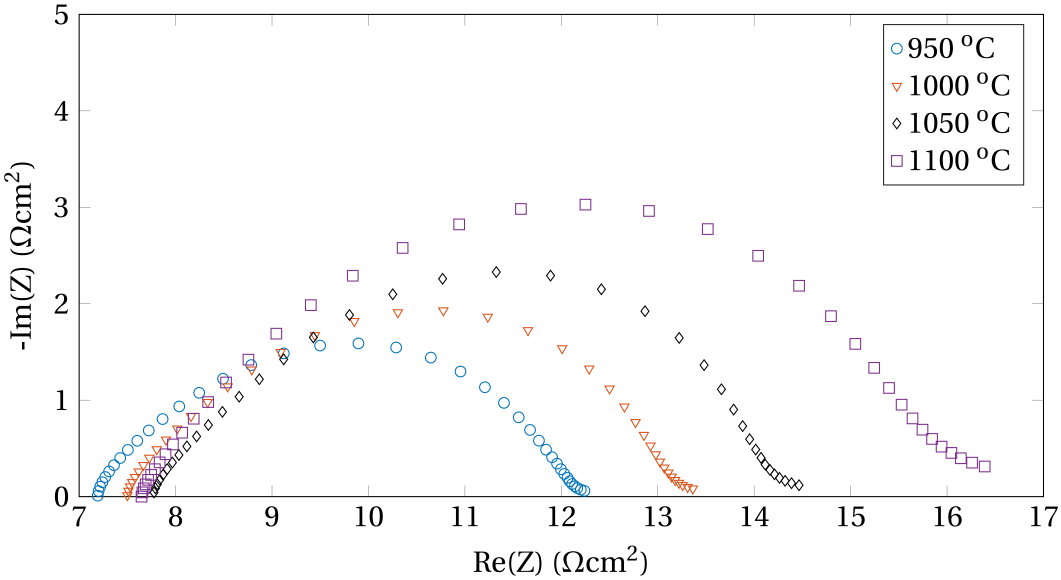

Figure C.2: Electrochemical impedance data recorded at 600 °C in pure oxygen for symmetric cells fired at 950 °C, 1000 °C, 1050 °C and 1100 °C.

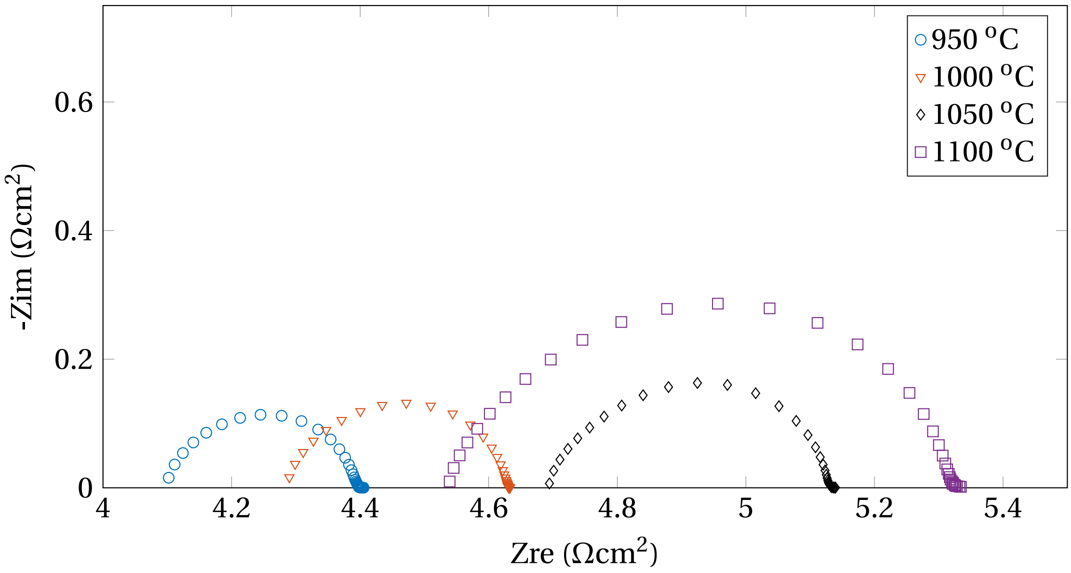

Figure C.3: Electrochemical impedance data recorded at 700 °C in pure oxygen for symmetric cells fired at 950 °C, 1000 °C, 1050 °C and 1100 °C.

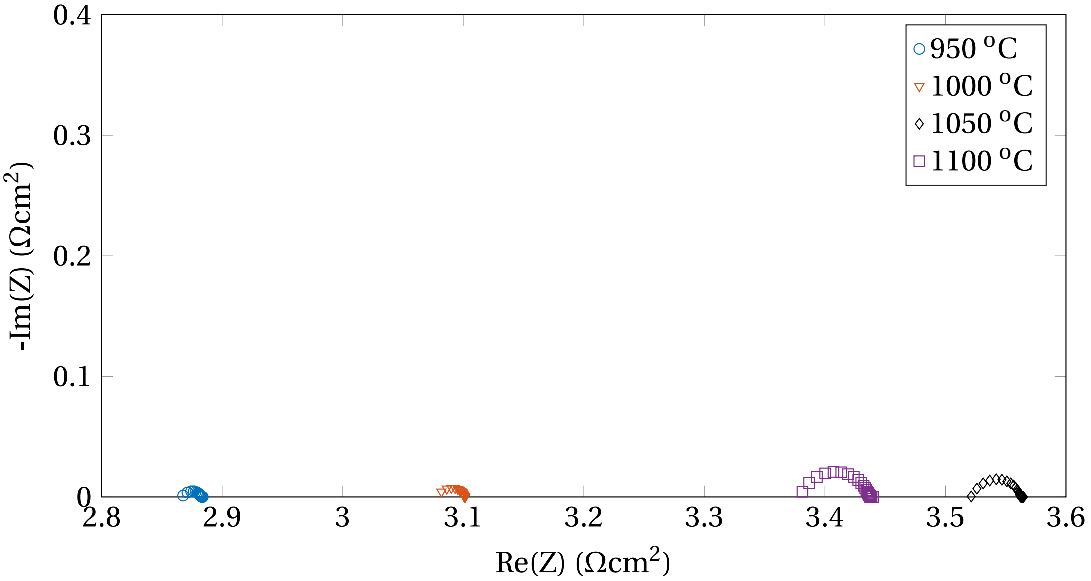

Figure C.4: Electrochemical impedance data recorded at 800 °C in pure oxygen for symmetric cells fired at 950 °C, 1000 °C, 1050 °C and 1100 °C.